Development of Accelerated Test Cycles for Analysing Real-World PEMFC Degradations

by

Xin Fu

A Doctoral Thesis

Submitted in partial fulfilment of the requirements for the award of Degree of Doctor of Philosophy of Loughborough University

Abstract

Polymer Electrolyte Membrane Fuel Cells (PEMFCs) are a promising alternative to replace Internal Combustion (IC) engines due to their zero-tailpipe emission and fast refuelling time. However, prolonged durability requirements are still remaining challenges for PEMFCs technologies. In addition, not only the prolonged durability requirement itself, measuring the lifetime of a PEMFCs are highly time and resource consuming. The aim of this research is to develop Accelerated Test Cycles (ATC) based on real-world PEMFCs operations to predict the degradations of real-world operations in a much-reduced testing time.

The ATC development strategy utilises Worldwide Harmonised Light Vehicle Test Procedure (WLTP) as a representative of a real-world operation. The strategy uses a PEMFCs performance model combined with Petri Nets degradation model to calculate second-by-second degradation voltage attributed to different degradation mechanisms. According to the calculated degradation voltage, selection criteria are applied, time steps are selected to build the ATC, and acceleration factor, which represents the ratio between the degradation voltage of the real-world application and that of the developed ATC is defined. By testing the developed ATC, the degradation voltage of the original operation can be predicted by multiplying the tested degradation voltage of the ATC by its acceleration factor.

The sensitivity of the ATC strategy is analysed. Results showed that the accuracy of the ATC to predict degradation voltage of the real-world operations decreases as the operation transit nature is more rapid. On the other hand, the accuracy decreases as the model accuracy decreases. When the acceleration factor of the ATC increases, the accuracy of the ATC also decreases.

The ATC development strategy was applied to Real Driving Emission (RDE) test cycles to demonstrate how the strategy is used in real-world scenario. The predicted degradation voltages showed a good agreement with the simulated ones.

The developed strategy has been combined with AST strategy to further facilitate degradation and reduce testing time. By simulating the developed WLTP-based test cycles at 80°C and 100°C, the degradation voltage of the original WLTP operation at 60°C is predicted using the acceleration factor of the ATC and Arrhenius relationship.

Experimental tests were conducted to validate the strategy. An ATC has been developed based on 400 cycles of the WLTP operation and was tested.

Degradation voltage prediction of the 400 cycles of the WLTP operation is made using the tested degradation voltage of the ATC. Results showed that the 200 hours operation has been condensed into a 27 hours ATC, reducing testing time by 86.5%, with a degradation voltage prediction accuracy of 89.96%.

Contents

Abstract ii
List of Figures vii
List of Tables x
List of Abbreviations xi
1 Introduction & Literature Review 12
1.1 Polymer Electrolyte Membrane Fuel Cells Basics 13
1.1.1 Types of Fuel Cells 13
1.1.2 Polymer Electrolyte Membrane Fuel Cells 14
1.1.3 Cell Voltage and Performance Losses 16
1.1.4 Degradation Mechanisms 20
1.1.5 Fuel Cell Diagnostic Tools 29
1.2 Model-Based PEMFCs Durability Prediction Methods 31
1.3 Experimental-Based PEMFCs Durability Testing Strategies 33
1.4 Accelerated Stress Test in PEMFCs 36
1.4.1 Temperature 37
1.4.2 Relative humidity 38
1.4.3 Load Cycling 39
1.5 Limitations of Testing Strategies in Literature 41
1.6 Literature Review Summary 42
1.7 Motivation 44
1.8 Aim & Objectives 45
1.9 Layout of Remaining Thesis 45
2 PEMFC Modelling Introduction 47
2.1 Introduction 47
2.2 0 – Dimensional FC Model 47
2.3 Degradation Model 51
2.3.1 Petri-Nets Degradation Model 51
2.3.2 Degradation Rates 54
2.3.3 Model Modifications 56
2.4 Combined Model and Model Variations 59

2.4.1 Model Variations 59
2.5 Conclusions 64
3 Accelerated Test Cycle Development Procedure 65
3.1 Introduction 65
3.2 Accelerated Test Cycle Development Strategy 67
3.2.1 Fuel Cell Cycles Conversion 68
3.2.2 Degradation Simulation 70
3.2.3 Steps Selection 73
3.2.4 ATC Construction and Acceleration Factor Calculation 74
3.2.5 Degradation Voltage Prediction and Error Analysis 76
3.3 ATC Validation 77
3.3.1 Experimental Set Up and Testing Equipment 78
3.3.2 Testing Procedure 82
3.3.3 Validation of The Models 83
3.3.4 Results and Error Analysis 87
3.4 Conclusions 88
4 ATC Sensitivity Analysis 89
4.1 Introduction 89
4.2 ATC Evaluation against Different Real-World Operations 89
4.3 ATC Evaluation against Different Selection Criteria 98
4.3.1 Model Assessment 98
4.3.2 Experimental Validation 104
4.4 ATC Evaluation against Different Models 106
4.4.1 Models Comparison 107
4.4.2 Results Analyses 110
4.5 Conclusions 114
5 Applying Developed Strategy to Real Driving Emissions 115
5.1 Introduction and Background Study of RDE 115
5.2 Methodology of Applying ATC Development Strategy to RDE 116
5.2.1 RDE Cycles Conversion 116
5.2.2 RDE Cycles Degradation Voltage Model Calculation 121
5.2.3 RDE-Based ATC Development 126

5.2.4 Degradation Voltage Prediction and Error Analysis 130
5.3 Conclusions 132
6 Combining Accelerated Stress Test with ATC Development Strategy .. 134
6.1 Introduction 134
6.1.1 A Product's Lifetime Distribution 135
6.1.2 Life-Stress Relationship 136
6.2 Combination of AST and ATC 138
6.2.1 Predicted WLTP Durability at 60°C from 80°C and 100°C Using Life-Stress Relationship 138
6.2.2 Predicted WLTP Durability at 60°C Using WLTP-Based ATCs at 80°C and 100°C. 140
6.3 Conclusion 147
7 Conclusions and Future Work 148
7.1 Major Contributions 148
7.2 Conclusions 148
7.3 Future Work 150
References 152
Appendix 167

List of Figures

Figure 1.1 – PEM fuel cells components and structure 14
Figure 1.2 – An illustration of a PEMFC stack 15
Figure 1.3 – Polarisation curve and losses of a 25×25cm^2 cell 20
Figure 1.4 – Typical impedance spectra of a PEM fuel cell [68] 30

Figure 2.1 – An overview of the PEMFC performance model 50
Figure 2.2– An example of a Petri Nets 51
Figure 2.3 - Pinholes Petri Net Module [92] 53
Figure 2.4 – Membrane creep Petri Nets graph [92] 56
Figure 2.5 – Modified carbon corrosion Weibull calculation block 58
Figure 2.6 – Original Pt agglomeration Petri Nets block 60
Figure 2.7 – Modified Pt agglomeration Petri Nets block 61
Figure 2.8 – Original peroxide attack Petri Nets block 62
Figure 2.9 – Modified peroxide attack Petri Nets block 63

Figure 3.1 - Flow diagram of accelerated stress test formulation and comparison logic 66
Figure 3.2 – WLTP Class 3 vehicle drive cycle 67
Figure 3.3 – Lab obtained polarisation curve and power curve 69
Figure 3.4 – WLTP PEMFC load profile 70
Figure 3.5 – Simulated cumulative WLTP degradation voltage 71
Figure 3.6- Simulated degradation voltage of one WLTP cycle 72
Figure 3.7 – Degradation rates of the WLTP operation simulation 73
Figure 3.8 - Degradation rates of the initial 1800s of the WLTP simulation and selection criteria 74
Figure 3.9 - WLTP-based ATC compare with WLTP operation load cycle . 75
Figure 3.10 – Simulated degradation rates of 400 WLTP cycles and selection criteria 77
Figure 3.11 – 400 WLTP based accelerated test cycle 78
Figure 3.12- Experimental Setup 79
Figure 3.13 – Mass flow controller 80
Figure 3.14 – Humidifier used 80
Figure 3.15 – Fuel cell heater and temperature controller 81
Figure 3.16 – TDI power system load bank 81
Figure 3.17 – The assembled 25 cm^2 Nafion 211 test cell with 0.3mg/cm^2 catalyst loading 82
Figure 3.18 – Tested Performance Decay of WLTP Cycles 84
Figure 3.19 – Electrochemical impedance spectroscopy before tests at different current densities 84

Figure 3.20 – Electrochemical impedance spectroscopy after tests at different current densities 85
Figure 3.21 – Error curves of Model 1 and 2 of predicting the degradation voltage loss of 0-400 WLTP cycles 86
Figure 3.22 – One Set of the Polarisation Curves Obtained before and after 400 WLTP Cycles Test 87

Figure 4.1 – NEDC and JC08 load profiles 90
Figure 4.2 – Voltage profile of PEMFC NEFC cycle 90
Figure 4.3 – Voltage profile of PEMFC JC08 cycle 91
Figure 4.4 – Simulated NEDC cumulative degradation voltage 91
Figure 4.5 – Simulated JC08 cumulative degradation voltage 92
Figure 4.6 – Degradation rates of the NEDC operation simulation 93
Figure 4.7 – Degradation rates of the JC08 operation simulation 93
Figure 4.8 – Degradation rates of the initial 1800s of the NEDC simulation and selection criteria 94
Figure 4.9 – Degradation rates of the initial 1800s of the JC08 simulation and selection criteria 94
Figure 4.10 – Initial 5000s NEDC-based ATC Compare with NEDC 95
Figure 4.11 – JC08-based ATC Compare with JC08 96
Figure 4.12 - Degradation rates of the initial 1800s of the WLTP simulation and different selection criteria 99
Figure 4.13 – Error curves of WLTP, NEDC, and JC08 predictions 104
Figure 4.14 – Errors variations against acceleration factors 106
Figure 4.15 – Model 1 calculation of degradation voltage loss of one WLTP cycle 107
Figure 4.16 – Model 2 calculation of degradation voltage loss of one WLTP cycle 107
Figure 4.17 – Degradation rates of the initial 1800s of the WLTP Model 1 simulation 108
Figure 4.18 – Degradation rates of the initial 1800s of the WLTP Model 2 simulation 108
Figure 4.19 – Model 2 simulated cumulative WLTP degradation voltage. 109
Figure 4.20 – Degradation rates of the Model 2 WLTP operation simulation 110
Figure 4.21 – Comparison of the errors of the prediction made based on Model 1 and Model 2 112

Figure 5.1 – RDE drive cycle 1 117
Figure 5.2 – RDE drive cycle 2 117
Figure 5.3 – RDE drive cycle 3 118
Figure 5.4 – RDE PEMFC load cycle 1 119
Figure 5.5 – RDE PEMFC load cycle 2 119
Figure 5.6 – RDE PEMFC load cycle 3 120

Figure 5.7 – Cumulative degradation voltage loss of RDE load cycle 1 ... 122
Figure 5.8 – Degradation rates of RDE load cycle 1 simulation 123
Figure 5.9 – Cumulative degradation voltage loss of RDE load cycle 2 ... 124
Figure 5.10 – Degradation rates of RDE load cycle 2 simulation 124
Figure 5.11 – Cumulative degradation voltage loss of RDE load cycle 3 . 125
Figure 5.12 – Degradation rates of RDE load cycle 3 simulation 125
Figure 5.13 – RDE load cycle 1 based accelerated test cycle 1 and comparison 126
Figure 5.14 – RDE load cycle 1 based accelerated test cycle 2 and comparison 127
Figure 5.15 – RDE load cycle 2 based accelerated test cycle 1 and comparison 128
Figure 5.16 – RDE load cycle 2 based accelerated test cycle 1 and comparison 128
Figure 5.17 – RDE load cycle 3 based accelerated test cycle 1 and comparison 129
Figure 5.18 – RDE load cycle 3 based accelerated test cycle 2 and comparison 129
Figure 5.19 – Error curves of RDE load cycles degradation voltage predictions 132

Figure 6.1 – A typical probability density function of a Weibull distribution 136
Figure 6.2 – Using life-stress relationship to predict lifetime distribution at different stress levels 137
Figure 6.3 – Flow diagram of testing ATCs at accelerated stress level..... 142
Figure 6.4 – Flow diagram of predicting the degradation voltage loss of WLTP using the acceleration factor of the accelerated test cycle 143
Figure 6.5 – Relationship between acceleration factor, temperature, and error 146

List of Tables

Table 2-1- List of Parameters Used in the Model 49
Table 2-2 - Weibull Distribution Data Used..... 55

Table 3-1 – List of variables of vehicle power calculation 68
Table 3-2 – WLTP-Based ATC Degradation Voltage Prediction 76
Table 3-3 – 0-400 WLTP Cycles Modelling and Tested Results Comparison 86
Table 3-4 – Prediction of Degradation Voltage of the 400 WLTP Operation Using tested ATC Results..... 88

Table 4-1 – NEDC Degradation Voltage Prediction 97
Table 4-2 – JC08 Degradation Voltage Prediction 97
Table 4-3 – The analysis of the transit nature of WLTP, NEDC, and JC08 cycles..... 98
Table 4-4 – WLTP based acceleration test cycles with various acceleration factors..... 100
Table 4-5 – WLTP based accelerated test cycles predictions and error 101
Table 4-6 –NEDC based acceleration test cycles with various acceleration factors..... 102
Table 4-7 – JC08 based acceleration test cycles with various acceleration factors..... 102
Table 4-8 –NEDC based accelerated test cycles predictions and error..... 103
Table 4-9 – JC08 based accelerated test cycles predictions and error 103
Table 4-10 – 400 WLTP cycles based ATCs with various acceleration factors 105
Table 4-11 – 400 WLTP cycles based ATCs experimental results and predictions with error 105
Table 4-12 – WLTP based acceleration test cycles with various acceleration factors developed using Model 2 111
Table 4-13–Model2-Based ATCs Predictions and Error..... 112

Table 5-1 – The analysis of the transit nature of the RDE PEMFC load cycle 1 to 3..... 121
Table 5-2 Degradation comparison between RDE, WLTP, NEDC, and JC08 122
Table 5-3 – RDE based acceleration test cycles with various acceleration factors..... 130
Table 5-4 – RDE based accelerated test cycles predictions and error..... 131

Table 6-1 – ATC simulation results at 60°C, 80°C, and 100°C 144

List of Abbreviations

ATC	Accelerated Test Cycle
PEMFC	Polymer Electrolyte Membrane Fuel Cell
NEDC	New European Drive Cycle
WLTP	Worldwide Harmonised Light Duty Vehicle Test Procedures
JC08	Japanese Drive Cycle
RDE	Real Drive Emission Test
AST	Accelerated Stress Test

Chapter 1

1 Introduction & Literature Review

Climate change and the production of greenhouse gases have drawn great attention in recent years. According to the International Energy Agency, global energy-related CO_2 emission has reached its historic high of 33.1 Gt in 2018, with an increasing rate of 1.7%, which was the highest since 2013 [1]. The change in global CO_2 emissions from 2014 to 2018 indicated that the global CO_2 emission reduction of 57 Mt and 28 Mt seen in 2015 and 2016 separately were reversed, with an increase of 527 Mt and 565 Mt in 2017 and 2018, respectively [1]. The annual CO_2 emissions in 2018 in the UK was 364.1 Mt, and 121.4 Gt was produced from transport industry, contributing 33% of the overall CO_2 production [2].

As a result, the emission legislation targets have become increasingly challenging for automotive manufactures to reduce CO_2 emissions. The transport industry has seen a shift towards low-carbon technologies with the likes of battery electric and fuel cell technologies being studied intensely. This is because these technologies have the potential to dramatically impact upon carbon emissions from the transport industry.

Although battery electric vehicles have been produced and sold by many manufactures all around the world, there are several barriers that need to be solved before Battery Electric Vehicle (BEV) can challenge the internal combustion engine vehicles. The most significant challenges for BEVs are range, cost, and charging time. Depending on the battery type and local electrical power limitations, fully charging a battery can take several hours, while refuelling a pressurised hydrogen tank may only take several minutes [3]. It was predicted by researchers that if hydrogen fuel cell vehicles contribute 80% of all the road vehicles in the EU by 2050, in a “business-as-usual” scenario, CO_2 emissions would be reduced by more than 50% [4]. Therefore, hydrogen fuel cells are believed to be one of the most promising candidates to replace internal combustion engines in vehicles.

1.1 Polymer Electrolyte Membrane Fuel Cells Basics

In this section, fuel cells, especially PEMFCs, will be introduced, covering types of fuel cells, operational voltage and degradation mechanisms of PEMFCs, and fuel cell diagnostic tools.

1.1.1 Types of Fuel Cells

Fuel cells are electrochemical devices that convert chemical energy in the reactant gases into electrical energy. Fuel cells are used as power source and have always been compared with internal combustion engines and batteries. As stated in Fuel Cell Fundamentals [5], fuel cells combine many of the advantages of its two competitors [5]. Compared with IC engines, fuel cells have higher efficiency, and can achieve zero-emissions if pure hydrogen is used [6]. Fuel cells also have some advantages over batteries such as the separation between power and capacity, and much quicker refuelling process. Although the electrochemical principles based on which all types of fuel cells operate are the same, six different types of fuel cells, which are Phosphoric Acid Fuel Cell (PAFC), Polymer Electrolyte Membrane Fuel Cell (PEMFC), Alkaline Fuel Cell (AFC), Molten Carbonate Fuel Cell (MCFC), Direct Methanol Fuel Cell (DMFC), and Solid Oxide Fuel Cell (SOFC), have been identified according to their different electrolyte, and the operating temperature of different types varies significantly, from 20 °C to 1000 °C [6]. Each type of fuel cell has its advantages and disadvantages. For example, although PEMFCs can be operated at relatively low temperature, between 60°C to 100°C, which makes it more feasible for portable and automotive applications, it can only use 99.999% pure H_2, and need to use sophisticated catalyst and electrodes [5]. In terms of high temperature fuel cells, such as SOFCs, the operating temperature of which is between 500°C to 1000°C, although the high temperature limits the feasibility of it possibility of being used in some area, not only H_2, but also hydrocarbons can be used as fuel, and reactions can take place without expensive catalysts[3]. According to the advantages of different types of fuel cells, different types of fuel cells are believed to be valuable in different areas. PEMFCs have attracted many research interests, especially in terms of automotive applications, due to its relatively low operating temperature and high-power density [5]. In contrast, SOFCs are believed to be more promising in stationary applications due to its high operating temperature and fuel flexibility [5]. Among all the above types of fuel cells, polymer electrolyte fuel cells (PEMFCs) are believed to be the most suitable candidate for automotive applications due to its low operating temperature and being able to cope with transient operations and vibration [5].

1.1.2 Polymer Electrolyte Membrane Fuel Cells

Polymer electrolyte membrane fuel cells utilise hydrogen as fuel and air as oxidant to generate electricity. Figure 1.1 below presents a diagram of the components and structure of a PEMFC

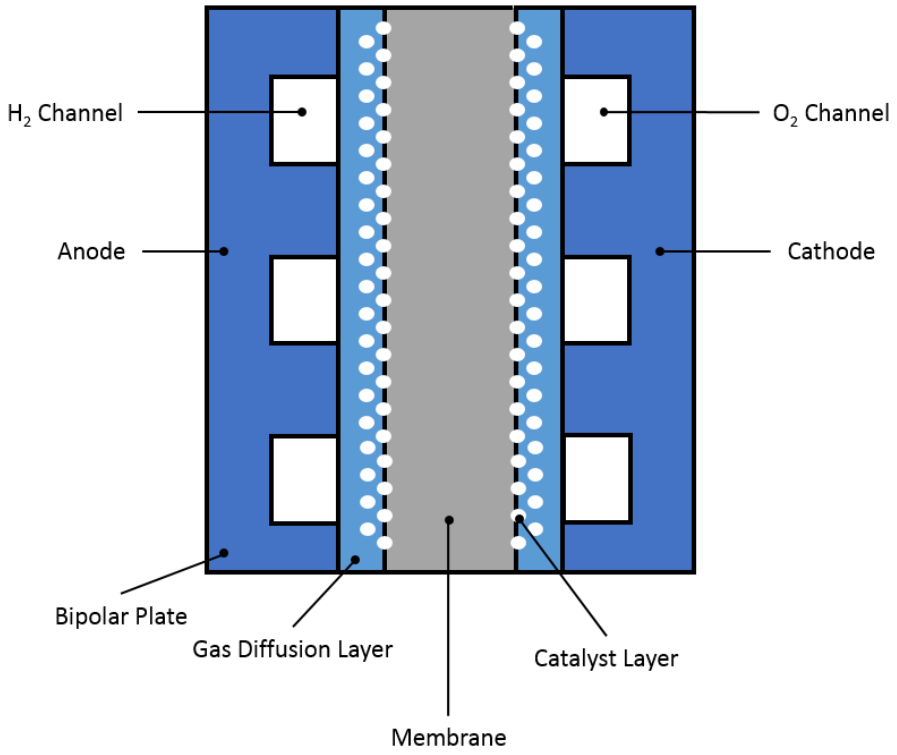

Figure 1.1 – PEM fuel cells components and structure

In a PEMFC, there are two electrodes, anode and cathode, separated by a polymer electrolyte membrane in the centre. Electricity is generated from hydrogen oxidation reaction and oxygen reduction reaction. Hydrogen is supplied to the anode side and is oxidised with the presence of catalyst to generate protons and electrons. Protons travel through the humid membrane to the cathode side and electrons travel around the external circuit from anode to cathode. Air is supplied to the cathode electrode and oxygen is reduced by the protons and the electrons to produce water and heat. Anode and cathode reactions were presented in Equation (1.1) and Equation (1.2) respectively, and the overall reaction is presented in Equation (1.3).

$$H_2 \rightarrow 2H^+ + 2e^- \tag{1.1}$$

$$\frac{1}{2}O_2 + 2H^+ + 2e^- \rightarrow H_2O \tag{1.2}$$

$$H_2 + \frac{1}{2}O_2 \rightarrow H_2O \quad (1.3)$$

A PEMFC consists of several components, which are polymer electrolyte membrane, catalyst layer, gas diffusion layer, bipolar plates and sealing gaskets. The structure of a single cell PEMFC is illustrated in Figure 1.1. The polymer electrolyte membrane allows protons to travel through from anode to cathode. Gas diffusion layer, normally made of Polytetrafluoroethylene (PTFE)-coated carbon fibre paper or cloth, helps the reactant gases to be spread in the flow channels and diffuses into the catalyst layer. The catalyst layer contains catalyst, normally carbon supported platinum, and is between the interface of the membrane and the gas diffusion layer. The hydrogen oxidation reaction and oxygen reduction reaction occur at the catalyst layer of the anode and cathode respectively, with the presence of catalyst. Bipolar plates are used to connect cells in series and are placed between individual cells. Sealing gaskets are used to seal the reactant gases and coolant.

Normally, the theoretical Open Circuit Voltage (OCV) of a single PEMFC is below 1V, and to meet the power demand of most applications, it requires multiple cells being connected in series to form a stack. An illustration of using multiple cells to form a PEMFC stack is presented in Figure 1.2. Cells were connected by bipolar plates and sandwiched in between two end plates, where current can be collected.

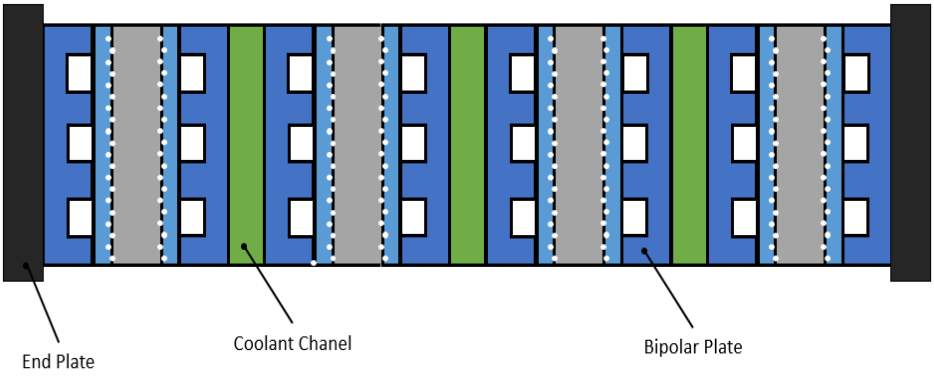

Figure 1.2 – An illustration of a PEMFC stack

The fuel cell stack is often only a small part of a fuel cell power system although it is the core energy generate device. Other equipment is also required and plays an important role in a fuel cell power system and is normally called balance of plant (BOP). Depending on the fuel cell type, fuel, and the purpose of the fuel cell power system, the BOP varies significantly. A

simple PEMFC power system can consist of hydrogen storages, compressors, humidifiers, a DC/DC converter, and an electric motor.

1.1.3 Cell Voltage and Performance Losses

PEMFC is an electrochemical device that converts chemical energy in the reactants into electricity, water, and heat, and therefore, it is important to evaluate the voltage it produces. Similar to other electric power generators, the operational voltage of a PEM fuel cell includes two parts: the reversible open circuit voltage and the voltage drop caused by irreversibilities.

Theoretical Open Circuit Voltage

To discuss the theoretical open circuit voltage of a PEM fuel cell, the 'Gibbs free energy' needs to be introduced first. According to Larminie and Dicks [6], the 'Gibbs free energy' is defined as the 'energy available to do external work, neglecting any work done by changes in pressure and/or volume'. In a fuel cell, the electric energy released is given by the change in Gibbs free energy, and the change is the difference between the Gibbs free energy of the products and that of the reactants.

In terms of a PEM fuel cell, the change in the molar Gibbs energy of formation is used to calculate the reversible open circuit voltage, and the equation is shown in equation (1.4) below.

$$E = \frac{-\Delta \bar{g}_f}{2F} \tag{1.4}$$

Where $\Delta \bar{g}_f$ is the change in the molar Gibbs free energy, and F is the Faraday constant.

As presented in equation (1.5). the fundamental reaction of a PEM fuel cell is:

$$H_2 + \frac{1}{2} O_2 \rightarrow H_2O \tag{1.5}$$

To calculate the $\Delta \bar{g}_f$, the change in the molar Gibbs energy of formation is defined is defined in terms of the molar entropy and the molar enthalpy by equation (1.6):

$$\Delta \bar{g}_f = \Delta \bar{h}_f - T * \Delta \bar{s} \tag{1.6}$$

Where $\Delta \bar{h}_f$ and $\Delta \bar{s}$ are the change in molar enthalpy and the change in molar entropy respectively. The value of $\Delta \bar{h}_f$ and the $\Delta \bar{s}$ are the differences between $\bar{h}_f$ and $\bar{s}$ of the product and those of the reactants.

$$\Delta \bar{h}_f = (\bar{h}_f)_{H_2O} - \left(\bar{h}_f\right)_{H_2} - \frac{1}{2}(\bar{h}_f)_{O_2} \tag{1.7}$$

$$\Delta\bar{s} = (\bar{s})_{H_2O} - (\bar{s})_{H_2} - \frac{1}{2}(\bar{s})_{O_2} \quad (1.8)$$

Because the enthalpy and the entropy are temperature dependent, the equations for calculating the molar enthalpy and molar entropy at temperature T are given in equation (1.9) and (1.10).

$$\bar{h}_T = \bar{h}_{298.15} + \int_{298.15}^{T} \bar{c}_p dT \quad (1.9)$$

$$\bar{s}_T = \bar{s}_{298.15} + \int_{298.15}^{T} \frac{1}{T}\bar{c}_p dT \quad (1.10)$$

The value of the molar enthalpy and the molar entropy of formation at 298.15K can be obtained from thermodynamics tables. The above calculations of reversible OCV assume no 'irreversibilities' and pure hydrogen and pure oxygen are used.

In real-world scenario, instead of pure hydrogen and oxygen, the reactants used in a PEMFC are normally a mixture of gases, and therefore, apart from temperature, the Gibbs free energy can also be affected by the reactant pressure and concentration, and therefore, affect the reversible open circuit voltage.

The effects can be explained by the Nernst equation, which describes the relationship of the partial pressures of the reactant gases and product, and the reversible open circuit voltage at temperature T as below. equation (1.11) presented the Nernst equation of a hydrogen fuel cell, where pressure in bar.

$$E = E^0 + \frac{RT}{2F}\ln\left(\frac{p_{H_2} * p_{O_2}^{\frac{1}{2}}}{p_{H_2O}}\right) \quad (1.11)$$

Where E is the reversible cell voltage, E^0 is the reversible OCV at standard pressure, R is the universal gas constant, F is the Faraday constant, and $p_{H_2}, p_{O_2}, and\ p_{H_2O}$ are the partial pressure of H_2, O_2, and the H_2O.

Performance Losses

As described previously, the reversible open circuit voltage of a fuel cell is not the actual output voltage of the cell. During fuel cells operation, there exist different types of losses that need to be taken into consideration when calculating the operational voltage. In this chapter, the four major irreversibilities of an operating hydrogen fuel cell will be explained.

Activation Losses

The activation loss is caused by the slowness of the reactions taking place on the surface of the electrodes. In low and medium temperature hydrogen fuel cells, the activation loss is the most important irreversibility and occurs

mainly at the cathode. Based on the Tafel equation, the activation loss in a hydrogen fuel cell is calculated using equations (1.12) below.

$$V = \frac{RT}{2\alpha F} \ln\left(\frac{i}{i_0}\right) \tag{1.12}$$

Where; R is the universal gas constant, T is the cell temperature, α is the charge transfer coefficient, i is the current density, and i_0 is the exchange current density.

The proportion of the applied electrical energy that is utilised to change the rate of the electrochemical reaction is defined as the charge transfer coefficient, and for hydrogen electrode and oxygen electrode, the value is about 0.5 and between 0.1 and 0.5 respectively.

The exchange current density is generated by the reversible electrochemical reactions at zero current density. High exchange current density indicates a more 'active' surface, and therefore, lower activation voltage loss.

Fuel Crossover and Internal Currents

Although ideally the electrolyte should only allow the ions to be transferred through, in reality, a small amount of hydrogen is diffused through the electrolyte and react with oxygen at the cathode. In this case, the wasted hydrogen does not produce electricity because no electrons travel through the outer circuit. The diffused hydrogen is known as fuel crossover. It is noticed that some electrons can pass through the electrolyte as well, given rise to internal currents. The calculation of fuel crossover and internal currents can be added to the calculation of the activation losses equation and is presented in equation (1.13).

$$V = \frac{RT}{2\alpha F} \ln\left(\frac{i+i_n}{i_0}\right) \tag{1.13}$$

Where R is the universal gas constant, T is the cell temperature, α is the charge transfer coefficient, i is the current density, i_0 is the exchange current density, and i_n is the internal current density.

Although the amount of crossover hydrogen is limited and the internal current is usually very small, it can significantly affect the actual open circuit voltage of a hydrogen fuel cell. The open circuit voltage of a hydrogen fuel cell can be reduced by 0.2V from theoretical value with an internal current of 1mA/cm^2 [6].

Ohmic Losses

During the operation of a fuel cell, electrons are travelling through the outer circuit, while protons are transferred through the membrane. Both movements will experience some resistance. The ohmic losses are caused by the electrical

resistance of the electrode and the resistance to the flow of the ions in the electrolyte. The calculation obeys the Ohm Law, as presented in equation (1.14).

$$V = i * r \tag{1.14}$$

Where i is the internal current density, and r is the area specific resistance, the resistance corresponding to 1 cm^2 of the cell and usually given in $k\Omega cm^2$.

Mass Transport or Concentration Losses

Reduced reactant concentration at the catalyst layer results in mass transport losses. In a hydrogen fuel cell where air is used as oxygen source, the mass transport at the cathode side domain because when current increases, the oxygen consumption rate at the cathode catalyst layer is higher than the oxygen diffusion rate from the flow field. Therefore, voltage is reduced at high current densities.

In addition, when the reactants pass through the channels, with the consumption of the reactants, the concentration of hydrogen and oxygen will be reduced, and result in reduced partial pressure, which cause voltage losses. The mass transport losses are calculated using the equation (1.15).

$$V = Bln(1 - \frac{i}{i_l}) \tag{1.15}$$

Where B is a constant that depends on the fuel cell and its operating state, and i_l is the limiting current density at the electrode which has the lowest limiting current density.

Operational Voltage

After identifying the reversible open circuit voltage and all the losses, the operational voltage of a hydrogen fuel cell can be calculated by subtracting the losses from reversible open circuit voltage. The operational of a hydrogen fuel cell is expressed in equation (1.16).

$$V = E - (i + i_n) * r - \frac{RT}{2\alpha F}\ln\left(\frac{i+i_n}{i_0}\right) - Bln(1 - \frac{i}{i_l}) \tag{1.16}$$

Where; E is the reversible open circuit voltage, i_n is the internal current density, R is the universal gas constant, T is the cell temperature, α is the charge transfer coefficient, i_0 is the exchange current density, B is a constant that depends on the fuel cell and its operating state, i_l is the limiting current density at the electrode that has the lowest limiting current density.

Figure 1.3 presented the reversible OCV, the operational cell voltage and the losses of a typical hydrogen fuel cell as a function of current densities. The polarisation curve was recorded by testing a 25×25cm^2 Nafion 211 single cell

at 60°C in the lab. The anode and cathode feed were pure hydrogen and air respectively. The losses were calculated based on the testing conditions. The polarisation curve can be divided into three regions, defined as activation losses region, ohmic losses region, and mass transport losses region [12]. Activation losses region is the low current density region, where the voltage drops sharply with increasing current densities, and the voltage drop is dominant by activation. Ohmic losses region is the intermediate current density region, where the voltage drop almost follows a linear relationship with the current densities, and it is usually the preferred operational region when PEM fuel cells are being utilised. In this region, with the increasing current densities, the voltage drop is mainly caused by ohmic loss. Mass transport losses region is the high current density region, where the voltage drops significantly due to the concentration losses caused by the limited reactant gas transportation through the GDLs and electrocatalyst layers.

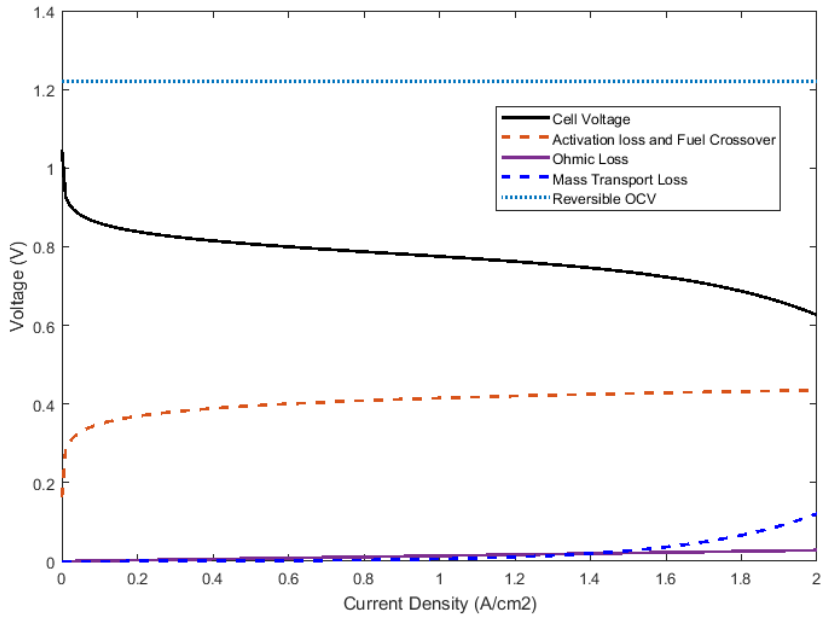

Figure 1.3 – Polarisation curve and losses of a 25×25cm² cell at 60°C

1.1.4 Degradation Mechanisms

Apart from the losses mentioned previously, as a result of subjected to a combination of acid conditions, water, reducing and oxidising environments, high temperatures, and high electrochemical voltages, components will experience another type of performance loss during fuel cell operations – degradation losses. In this section, degradation mechanisms are discussed in

terms of different components: membrane, electrocatalyst and catalyst layer, gas diffusion layer, bipolar plate, and sealing gasket.

Membrane Degradation Mechanisms

In a PEM fuel cell, the proton electrolyte membrane used is sulphonated fluoro-polymers, usually fluoroethylene, and the construction processes of the membrane material are as follows [6]: the hydrogen of the polyethylene is substituted by fluorine, a process called perfluorination, and the product is polytetrafluoroethylene (PTFE). To sulphonate the PTFE, a side chain ending with sulphonic acid HSO_3 is added, and the product is named perfluorosulfonic acid (PFSA). The suplhonic acid group added is ionically bonded, and therefore, the resulting produced is named ionomer. The PTFE is strongly hydrophobic. However, after it is sulphonated, the sulphonated side chain is highly hydrophilic, which means hydrophilic regions are created around the sulphonated side chains to absorption large quantities of water while the structure remains strongly hydrophobic. Within the hydrated regions, H^+ ions are more likely to move because they are relatively weakly attracted to the SO_3 group. The movement of H^+ ions contributes to the conductivity of the membrane and allow protons to travel through the membrane from anode to cathode. The most well-known and widely used membrane is the 'Nafion', which was manufactured by DuPont in 1960s, and has been developed and established since then [5].

The membrane is placed between two electrodes and is utilised to separate the reactant gases and the oxidising and reducing environments, support anode and cathode catalyst layers, and more importantly, transport protons [13]. Based on the functionalities of the membrane, the requirements of a membrane are: chemically highly resistant, mechanically strong and can be made into very thin films, good proton conductivity when hydrated, and minimised gas permeability [6][14]. At present, the durability of the membrane remains a critical issue that reduces the lifetime of PEM fuel cells and delays the commercialisation of PEM fuel cells. Some researchers claimed that the decay of the Membrane-Electrode-Assembly (MEA) was primarily responsible for the degradation of the fuel cell performance [15-18]. Membrane degradation is usually classified into two different categories based on the causes of the degradation: mechanical degradation and chemical degradation [13][19][20].

Mechanical Degradation

Although the mechanical properties such as tensile strength, tear strength, and puncture resistance of commonly used membranes are usually satisfied, there still exist some problems when utilising the membrane in a fuel cell environment [6]. Early life failure can be caused by the congenital defects or improper MEA manufacturing process, which may result in pinholes, cracks

or perforations [13][14][21]. At the areas, such as gas inlets and edges, where the membrane experiences non-uniform or high pressure, the formation of small perforations or tears may also be accelerated, and therefore, facilitate the degradation of the membrane [22]. In a PEMFC, membrane is placed between tow bipolar plates, and the compressive pressure can lead to creep of the membrane, which is believed to be one of the main reasons for membrane thinning [10]. The higher the pressure, the severer the membrane thinning.

Chemical Degradation

Gas crossover to the respective reverse electrodes causes only a 1-3% fuel cell efficiency loss because the crossover rate is relatively low [23][24]. However, peroxyl and hydroxyl radicals, which are believed to result in the chemical attack on the membrane and catalyst layer, can be produced by the reactions on the electrocatalyst [25][26], and it is the chemical degradation that is the major cause for performance decay of PFSA membrane [27-29].

Formation of peroxyl and hydroxyl radicals

According to Rodgers et al. [13], two mechanisms have been proposed for the formation of peroxyl and hydroxyl radicals.

The first mechanism indicates that hydroxyl radicals are generated by the decomposition of hydrogen peroxide, as shown in equation (1.20), which can be formed either chemically at the anode side, as shown in equation (1.17), or both chemically and electrochemically at the cathode side, described in equation (1.18) and (1.19) [13].

At the anode side:

$$H_2 + O_2 \rightarrow H_2O_2 \tag{1.17}$$

At the cathode side:

$$H_2 + O_2 \rightarrow H_2O_2 \tag{1.18}$$

$$2H^+ + O_2 + 2e^- \rightarrow H_2O_2 \quad E^0 = 0.672V \tag{1.19}$$

$$\frac{1}{2}H_2O_2 \rightarrow HO^{\bullet} \tag{1.20}$$

The second mechanism is proposed by LaConti et al. and described in equation 1.21) to equation (1.25) [30]. Hydrogen is reduced to hydrogen ions on Pt catalyst at the anode side, and then oxidised by the crossover oxygen to form peroxyl radicals as shown in equation (1.22). Hydrogen peroxide is then formed and diffuses into PEM as described in equation (1.23). With the presence of metal ions, hydroxyl radicals will be generated from hydrogen peroxide following equation (1.24).

$$H_2 \rightarrow 2H^{\bullet} \quad (1.21)$$

$$H^{\bullet} + O_2 \rightarrow HO_2^{\bullet} \quad (1.22)$$

$$HO_2^{\bullet} + H^{\bullet} \rightarrow H_2O_2 \quad (1.23)$$

$$H_2O_2 + M^{2+} \rightarrow M^{3+} + OH^{\bullet} + OH^{-} \quad (1.24)$$

$$OH^{\bullet} + H_2O_2 \rightarrow H_2O + HO_2^{\bullet} \quad (1.25)$$

The chemical degradation of a PFSA membrane is believed to follow the following three steps: end groups unzipping, chemical attack of the C-F bond in side chain, and scission of the main chains.

Three steps of chemical attack

Depending on the type of membrane, chemical attack can take place at different points of the material structure. As for PFSA membrane, the H-containing partially fluorinated end groups, such as R-CF_2COOH, -CF_2H and carboxylic end group, that are formed inevitably during the manufacturing process are very sensitive to peroxide radicals, and it is generally accepted that the chemical attack initially takes place at the per-fluorocarbon backbone and side chain groups and may propagate along the main chain [31]. The proposed chemical attack reactions on carboxylic acid end groups are as follow [31]:

$$R_f\text{-}CF_2COOH + {}^{\bullet}OH \rightarrow R_f\text{-}CF_2^{\bullet} + CO_2 + H_2O \quad (1.26)$$

$$R_f\text{-}CF_2^{\bullet} + {}^{\bullet}OH \rightarrow R_f\text{-}CF_2OH \rightarrow R_f\text{-}COF + HF \quad (1.27)$$

$$R_f\text{-}COF + H_2O \rightarrow R_f\text{-}COOH + HF \quad (1.28)$$

The fluoride release rate is therefore an ideal indicator of PFSA degradation rate, and the Fluoride Emission Rate (FER) can be measured from the product water directly. It has been proved that the FER technique is being increasingly widely utilised to measure ionomer degradation [23][29][32][33].

In addition to the chemical attack of the end group, hydroxyl radicals also attack the side chain of the polymer under certain conditions [34][35]. According to Coms [34], when operating PEM fuel cell under dry conditions, the hydroxide radical can abstract the proton, which is attached on the side group as -SO_3H, to form $SO_3^{\bullet}$ and therefore weakens the C-S bond, which can result in the formation of perfluoro-radical. Then the perfluoro-radical will eventually form an oxy-radical that is bonded to the main chain of the PFSA backbone. Moreover, the C-F bond bonds on the main chain in PFSA can also be attacked by hydrogen and result in main chain scission [30].

Being attacked by radicals can result in loss of mechanical strength and proton and electrical conductivity. As a result, the ohmic resistance and overall cell resistance will be increased.

Electrocatalyst and Catalyst Layer Degradation Mechanisms

Another key factor that limits PEM fuel cell performance and durability is the degradation of the electrocatalyst layer, which is sandwiched in between the membrane and the gas diffusion layer. The catalyst for both anode and cathode is nanometre sized platinum (Pt) or a Pt-alloy, which is supported on high surface area carbon materials and fixed to either the gas diffusion layer or the membrane, depending on different manufacturing processes, to ensure the three-way contact between electrolyte, catalyst, and reactant gas. The catalysts are usually embedded in an ionomer to mediate proton migration and water transport [37].

As one of the fundamental mechanisms that significantly affect the lifetime and performance of PEM fuel cells, the degradation of the catalyst layer has been addressed and studied by many researchers, and degradation mechanism is relatively well understood. According to different causes of degradation, the degradation of the catalyst layer can be classified into two aspects, which are losing of electrochemically active surface area (ECSA) and effects of contaminations.

Loss of activity

The Electrochemical Active Surface Area (ECSA) is the main factor that reflects the activity of the catalyst layer, and will therefore, to some extent, determine the performance of the fuel cell. Many researchers reported in various papers that the ECSA of the Pt-catalyst measured after their tests decreased with time [37]. The decrease of ECSA can be caused by Pt degradation, carbon support degradation, and the degradation of the ionomer.

Pt degradation

As stated previously, the Pt-catalyst used in PEM fuel cells is nanometre sized. The agglomeration of the nanosized catalyst is inevitable during preparation of the MEAs because Pt particles agglomeration was observed in fresh MEAs [38][39], and it is the inherent tendency of nano-particles to agglomerate into larger particles to reduce the high surface energy [36]. Several mechanisms have been proposed by researchers to explain Pt agglomeration and particle size growth during PEM fuel cell operations, while no agreement on which process contributes the most has been achieved: (1) Ostwald ripening is the phenomenon that leads to particle size growth due to the dissolution of small Pt particles into the ionomer phase and redeposit on bigger particles [40][41]. (2) Cluster-to-cluster collision can lead to the nanometre scale agglomeration of Pt particles on carbon support [42]. (3) Particle size growth will also be

caused by coarsening of the catalyst because of particles movement and/or Pt particle coalescence [43][44].

In addition to Pt agglomeration and particle size growth, the degradation of the catalyst layer can be also caused by Pt loss due to Pt detachment, dissolution and migration. It is widely accepted that Pt dissolution is a critical process in catalyst degradation, although the reaction taking place may vary depending on different electrode aging process, and higher Pt ion concentration results in higher Pt/C catalyst degradation rate [36]. Darling and Meyers proposed a three-step dissolution model that explained the Pt dissolution process [45]:

$$\text{Pt dissolution: } Pt \rightarrow Pt^{2+} + 2e^- \tag{1.29}$$

$$\text{Pt oxide formation: } Pt + H_2O \rightarrow PtO + 2H^+ + 2e^- \tag{1.30}$$

$$\text{Pt oxide dissolution: } PtO + 2H^+ \rightarrow Pt^{2+} + H_2O \tag{1.31}$$

The presence of Pt particles both in the interface between the catalyst layer and the membrane and inside the membrane have been reported by many researchers [46], and it is caused by Pt migration, which is the phenomenon that dissolved Pt diffuses into the ionomer phase, and reduced by crossover hydrogen at the cathode, which result in Pt precipitate in the membrane [47][48]. Pt migration can significantly affect the membrane by reducing its stability and conductivity.

Carbon corrosion

Corrosion of the carbon support is another factor that reduces the ECSA and therefore, dramatically affects the durability and performance of the catalyst layer. The oxidisation of carbon to carbon dioxide can take place at quite low voltage following the reaction shown below [49]:

$$C + H_2O \rightarrow CO_2 + 4H^+ + 4e^- \quad E_0 = 0.207V \; versus \; RHE \tag{1.32}$$

Theoretically, the kinetics of the reaction is slow and carbon corrosion is negligible at voltages lower than 1.1V during normal PEM fuel cell operations [49]. However, with the presence of Pt catalyst, the oxidisation reaction is catalysed following the mechanisms below [50]:

$$C + H_2O \rightarrow CO_{surf} + 2H^+ + 2e^- \quad E > 0.207V \; versus \; RHE \tag{1.33}$$

$$CO_{surf} + H_2O \xrightarrow{Pt} CO_2 + 2H^+ + 2e^- \quad E = 0.8V \; versus \; RHE \tag{1.34}$$

CO_{surf} will be formed irreversibly on the surface of carbon particle at voltages higher than 0.3V versus RHE, and then oxidised to CO_2 at a voltage of 0.8 V versus RHE. The effects of Pt catalyst on carbon corrosion have been

proved by Roen et al., who detected CO_2 emission at voltages over 1.1V versus RHE without the presence of Pt, while CO_2 emission was detected in a voltage range from 0.55-0.6V with the presence of Pt [51].

During prolonged fuel cell operation, carbon corrosion can be affected and accelerated by different conditions such as fuel starvation, start-up/shutdown cycling, and open circuit voltage operation et al., which will be explained in detail later.

Ionomer and interfacial degradation

To mediate proton migration and water transport of the MEA, the carbon supported catalyst is often embedded in a polymeric ionomer, usually recast Nafion ionomer. The ionomer is also a significant factor that influences the structure and performance of the catalyst layer as it is utilised to create a three-phase interface between reactant gases, membrane and catalyst. The chemical/physical degradation and dissolution of the ionomer can result in decreased conductivity and mass transport ability of the MEA [36].

As demonstrated previously, chemical attack of peroxide radicals can degrade the Nafion ionomer. The same degradation process can occur in the catalyst layer during fuel cell operation. However, the degradation rate of the ionomer in the CL is lower than that in the membrane as some of the radicals can be eliminated by the Pt catalyst [52]. In contrast, as the recast Nafion ionomer is located at the fuel cell reaction active sites, where higher water content is available, from both humidified inlet water and water generation. This may facilitate the dissolution and chemical degradation of the ionomer in the CL compared with that in the membrane [53]. It remains unclear which influence is more significant to ionomer degradation. Despite the difficulties of distinguishing the effect of ionomer degradation in the CL from that caused by Pt degradation and carbon support corrosion, some researchers have demonstrated the degradation of Nafion ionomer in CL using cell impedance trends and X-ray photoelectron spectroscopy (XPS) et al. [45][54].

The dimensional changes of the membrane caused by changes in water content can temporally alter the contact and connection of the interface between membrane, catalyst layer and the GDL, and these changes are reversible. In contrast, with the accumulation of the microstructural changes inside the CL, the connection between different solid phases of the MEA can be affected irreversibly. Guilminot et al. observed a separation and cracks at aged membrane/cathode interfaces [38]. It is believed that ice formation in the CL is one of the main reasons that damage the interfacial structure [55][56].

Contaminated by impurities

Contaminations also have a negative effect on the electrocatalyst and catalyst layer. There are two main resources that contaminations can be induced from, which are from the reactant gases supply and from the fuel cell system.

On the anode side, PEM fuel cells utilise hydrogen produced by reforming hydrocarbons. The products of the reformate process are hydrogen, carbon dioxide and carbon monoxide. After treatments such as water-gas shift reaction and selective oxidation can reduce the concentration of carbon monoxide to 10-100 ppm [57]. However, even parts per million levels of carbon monoxide can result in serious poisoning of the catalyst [58]. Carbon monoxide has a strong affinity to Pt, and thus can absorb on the active sites of the catalyst. Even very low concentration of carbon monoxide can occupy more sites than hydrogen, and therefore block access of hydrogen to the sites, which causes reduction of Pt catalyst activity and result in cell performance decay due to kinetic loss of the anode. Furthermore, researchers have observed that carbon monoxide can be transferred from the anode to the cathode side at certain conditions and affects the cathode performance by poisoning the cathode catalyst [58].

Sometimes sulphur-containing species also exist in the reformatted gases and are feed to the anode together with hydrogen. The effects of sulphur-containing species are also studied by researchers and it is demonstrated that it can cause irreversible degradation on the catalyst to significantly affect the cell performance. Garzon et al. observed chemisorbed sulphur species onto the catalyst surface when 1 ppm H_2S was added to the hydrogen feed, and their cell was almost completely deteriorated after running at a constant voltage of 0.5V for 21h [59].

In contrast, on the cathode side, the degradation phenomenon caused by some contaminations from the feeding gas, such as NO_2, is reversible and the poisoning mechanism is believed not catalyst related [56]. Another impurity that is believed to have negative effect on Pt catalyst on the cathode side is Cl^-. The poisoning mechanism of Cl^- is described by Matsuoka et al. as follows: 1). Cl^- facilitates the dissolution of Pt to generate Pt ions. 2). Pt ions are reduced into Pt by the crossover hydrogen and deposited in the membrane.

Gas diffusion layer degradation Mechanisms

Gas diffusion layer is placed above the catalyst layer to provide mechanical support, diffuse reactant gases to the catalyst layer, maintain electronic contact, transfer heat, and remove water. The GDL consists of a macro porous carbon cloth or carbon paper substrate covered by a thinner Microporous Layer (MPL), which consists of carbon black powder and a hydrophobic agent [14]. More attention has been paid to the impact of materials and design

of GDL on PEM fuel cell performance rather than degradation and durability issues in past studies of GDLs [13]. Therefore, the degradation mechanisms of GDLs are still unclear. Furthermore, although some researchers have done some tests on GDL degradation, most of the tests employed ex situ experiments to separate the effects of other components, which result in the uncertainty of the real performance decay of GDL used in PEM fuel cells.

Changes in GDL physical properties have been observed by researchers. The most widely noticed property changes are loss of hydrophobicity, weight loss, and decreased conductivity. Borup et al. [60] witnessed loss of hydrophobicity of the GDL in their tests and demonstrated that it increased with temperature, and they also concluded that the changes were mostly attributed to the MPL. Mukundan et al. proposed that loss of hydrophobicity of the GDL could result in increased mass transport loss, and therefore, affected the cell performance [61]. Kangasniemi et al. experienced weight loss and increased MPL contact angle during their experiments, and they also indicated that those changes were attributed to the MPL [14]. Wu et al. claimed that weight loss was one of the most critical degradation mechanisms of GDL degradation and weakened structure and changed properties can be caused by excessive mechanical stress resulted from the compression force in the cell, which would accelerate the weight loss during ageing [62]. The macro porous carbon cloth or carbon paper usually needs to be coated with PTFE to ensure its hydrophobicity. During fuel cell operation, the PTFE and carbon composite of the GDL may be exposed to chemical attack by radicals such as hydroxyl, and the attack may result in decreased conductivity and hydrophobicity [13].

Bipolar plates degradation Mechanisms

Bipolar plates are placed between cells to connect cells in serious. The plate serves as a gas separator and current collector of the cell. To fulfil the required functions, the requirements for materials for bipolar plates are high electrical conductivity, low gas permeability, high corrosion resistance, sufficient strength, low thermal resistance, and low cost, etc [6]. Graphite and stainless steel are two widely used materials for bipolar plates.

Graphite has the outstanding characteristics such as high corrosion and chemical resistance, low density, and high electrical and thermal conductivity. Therefore, the possibilities of failure are higher in durability under shock and vibration, hydrogen permeability, and manufacturability. Although corrosion resistance of graphite is high, under extreme conditions, especially under startup/shutdown cycles and fuel starvation conditions, carbon corrosion may still occur in graphite bipolar plates. De Bruijn et al. reported complete erosion of a graphite plate under cell reversal condition [14].

Metallic bipolar plates are studied by researchers in order to reduce cost and improve power density. When metal material is used in bipolar plates, one of the most critical issues is corrosion. As one of the most widely used metal material, stainless steel has been utilised by researchers as material of bipolar plates. However, corrosion was observed at the anode side, where most stainless steels were operated in their active region and dissolved in the medium they exposed to directly [14]. Makkus el al. claimed that no metal material had been identified that could avoid corrosion to occur in direct contact with the membrane [63]. Release of contamination ions form metal bipolar plates is another effect that will cause performance decay of the cell. Pozio observed iron contaminations in the MEA when using stainless steel end plates, but when aluminium end plates were used, no such contaminations observed [64]. To seek the possibilities to improve the corrosion resistance and contact resistance of stainless steel bipolar plates, different materials have been used by researchers to coat the plates. One of the most commonly used coating materials is gold [65].

Sealing gasket degradation Mechanisms

The sealing gaskets used in PEM fuel cells are usually made of elastomeric material and are used to seal the reactant gases and the coolant. Most widely used material is silicone. During fuel cell operation, the gaskets will be exposed to an acid liquid environment, humid air and hydrogen, and mechanical stress, all of which may result in degradation and failure of the gaskets. According to researches on degradation phenomena of seals, four major degradation mechanisms domain the degradation of the sealing gasket, which are weight loss, silicon and calcium leach, change of surface chemistry, and change of mechanical properties.

Silicon and calcium leaching from the gasket into the soaking solution was observed by Tan et al, together with the observation of altered surface chemistry [67]. Li, Tan and Gong also reported that the change of surface chemistry initially proceeded via de-crosslinking and chain scission in the backbone, and they observed the surface conditions of the gaskets changed from smooth to rough, and finally crack [68]. Significant mechanical properties change was reported by Tan et al. [69].

1.1.5 Fuel Cell Diagnostic Tools

When performing fuel cell testing, the performance of the test cell needs to be analysed, both quantitively and qualitatively. In this section, the commonly used diagnostic tools for fuel cell performance measurement will be introduced, including polarisation curves and power curves, Electrochemical Impedance Spectroscopy (EIS), and other widely used electrochemical and physical diagnostic tools.

Polarisation Curves

A plot of operational voltages against current densities, names as a polarisation curve, is always useful to characterise the performance of a fuel cell. The reason why voltage is plotted against current densities rather than current output is because if all the other factors are fixed, the current output of a cell is in direct proportional to the active area of the cell, and therefore, using current densities is more convenient to compare cells with different active area. Because the cell performance is affected by many factors such as cell temperature, inlets and outlets pressure, humidity etc., a polarisation curve can only represent the performance of a cell at the operating condition when the curve is recorded, and changes in operating conditions will result in a different current density and voltage relationship.

Electrochemical Impedance Spectroscopy

Another powerful tool to analyse fuel cell performance and degradation is electrochemical impedance spectroscopy. When performing EIS, a small ac voltage or current perturbation is applied to the cell, and the amplitude and phase of the resulting signal are measured as a function of frequency [69]. EIS is widely used to study the oxygen reduction reactions [70] [71], to characterise transport losses [72] [73], and to evaluate electrode properties and ohmic resistance [74]. A typical example of impedance spectra of a PEM fuel cell in Nyquist form with two arcs is shown in Figure 1.4 [69].

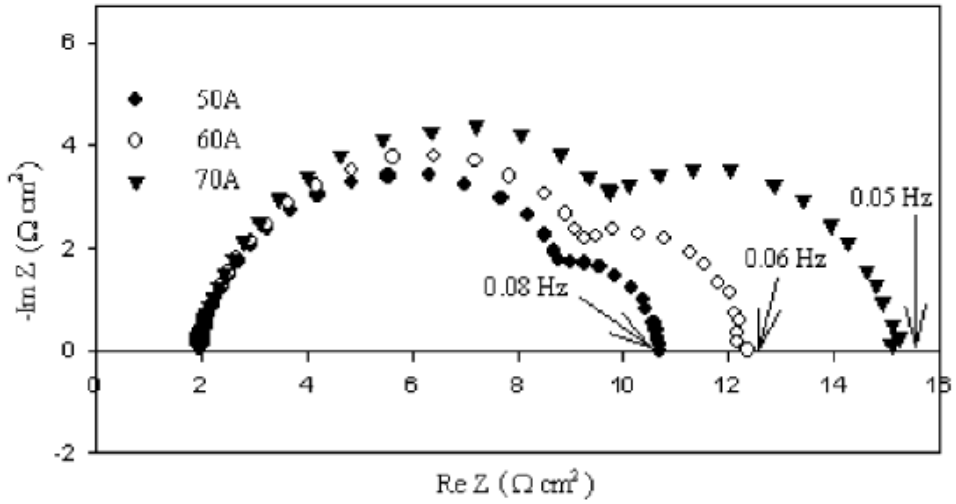

Figure 1.4 – Typical impedance spectra of a PEM fuel cell [68]

The frequency increases from the right to the left. Impedance due to mass transport loss can be analysed from the low frequency arc [75], while the impedance due to the combination of the double-layer capacitance in the catalyst layer and the effective charge transfer resistance and the ohmic resistance [70] [76] can be analysed from the high frequency arc.

Due to the high kinetics of Hydrogen oxidation reaction at anode side, the cathode impedance almost equals the impedance of the fuel cell, and therefore, EIS is mainly used to analyst the cathode behaviours [69]. However, Schiller et al. [77] and Leng et al. [78] used EIS to study the effects of CO poisoning on the anode catalyst.

Other Diagnostic Tools

Pressure drops within fuel cells can be used as a diagnostic tool to detect flooding, especially at cathode side, as water production and accumulation will increase gas flow resistance and therefore increase pressure drop [79]. Gas chromatography can be used to measure species distribution within a PEM fuel cell [80]. Moreover, gas chromatography has been widely used by researchers to measure the crossover rate [81] [82].

Cyclic voltammetry is another electrochemical approach that is commonly used in PEM fuel cell degradation research. It is valuable for ascertaining the ECSA of the catalyst layer. The cyclic voltammetry is performed by sweeping the potential of a system between two voltage limits while recording the current. The ECSA can be calculated as follow [69]:

$$ECSA = \frac{Charge\ of\ H_2\ absorbtion}{210\ (charge/cm^2) \times catalyst\ loading} \tag{1.35}$$

1.2 Model-Based PEMFCs Durability Prediction Methods

Various modelling techniques have been employed by researchers to describe the aging and degradation process and estimate the durability of PEMFCs. Sauer and Wenzl summarised different lifetime prediction approaches of electrochemical systems and three approaches have been identified, which are physico-chemical aging model, weighted Ah ageing model, and event-oriented ageing model [83]. According to Sauer and Wenzl, when utilising physico-chemical ageing model to predict lifetime of a system, the model, which was based on the fundamental equations of the electrochemical reactions is built in the first step, followed by the utilisation of information from testing on the ageing effects to quantify ageing processes and their impact on performance, which enabled lifetime prediction of the system under any operating conditions [83]. The weighted Ah ageing model is based on the assumption that the effects of a given Ah throughput on the lifetime depends on the details of the conditions during the throughput. This approach utilises a factor to weight the Ah throughput to quantify the different impact of different operating conditions on lifetime. The ‘tougher’ the condition the higher value of the factor. For example, cycling a lead-acid battery at low states of charge is believed to stress the battery more than at high state of charge. If 10Ah is charged at low states of charge condition, then 10Ah should be multiplied by a factor to obtain the corresponding ‘effective’ throughput.

When utilising the event-oriented ageing model, the loss of lifetime of a system consists of two aspects, which are the incremental loss of lifetime and the loss of lifetime caused by well-defined events [83]. The effect of each event is quantified into loss of lifetime and when a certain number of events occurred, the lifetime of a system runs out. Each approach has advantages and disadvantages when being applied to PEM fuel cell lifetime prediction. The physico-chemical model requires a good understanding of the degradation mechanisms of PEM fuel cell to build the model based on the electrochemical reactions occurred during the accelerated degradation tests. The most critical work when using the Weighted Ah ageing model is to identify the factor that corresponds the failure time of the accelerated tests and the end of lifetime. The event-oriented ageing model requires an accurate quantified loss of lifetime of each well-defined event.

Marrony et al. [84] predicted the lifetime of a PEM fuel cell by comparing the degradation rate under stationary operating condition with that under cycling dynamic conditions to identify how many hours of lifetime under normal operating conditions that one accelerated tests cycle corresponds to, and therefore deduced the lifetime of the cell. However, this method did not apply to those cases that the cell did not 'fail' at the end of the accelerated tests.

Although lifetime prediction is relatively less developed in fuel cell area, it has been applied to other fields for a relatively long time. Lankford and Hudak Jr [85] predicted the lifetime of gas turbines against small crack problem. In their study, they built a model based on fracture mechanics to predict the crack growth and therefore to predict lifetime of gas turbines. Meier, Nissley and Sheffler [86] developed a model to predict the lifetime of thermal barrier coating. The model was generated by combining models of different failure mechanisms.

From the above it can be concluded that modelling is essential for lifetime prediction. Some researchers have already made their contributions to modelling of PEM fuel cell degradation based on degradation mechanisms or performance loss. Fowler et al. [87] modified a Generalised Steady State Electrochemical Model (GSSEM) of PEM fuel cell that was proposed by Mann et al. [88] to incorporate voltage degradation. The GSSEM is expressed by subtracting the losses, which are activation loss, ohmic loss and mass transfer loss, from the thermodynamic potential, which is calculated using Nernst equation. When incorporating voltage degradation into the GSSEM, Fowler et al. [87] built their model in order to model the observed performance decay, rather than modelling the actual degradation modes mechanistically. They classified the failure causes into three modes, which were loss of apparent catalytic activity, conductivity loss, and loss of mass

transfer of reactants. Each failure mode could be represented by modifying the coefficient values of the GSSEM and the results indicated that the model successfully described the observed voltage degradation of their test cell.

Liu and Case [89] analysed the performance decay of their test cells under dynamic testing conditions and utilised a semi-empirical model to incorporate the observed aging phenomena during their tests. The equations were similar to the GSSEM, which was calculated by subtracting the losses from the thermodynamic potential. The model was a phenomenological model and it was a steady-state model that can only describe the performance decay at specified time nodes. It still requires a transient model to capture the dynamic behaviour under dynamic conditions.

Degradation model of individual component of PEM fuel cells has also been done by researchers. Bi and Fuller [90] developed a model describing Pt/C catalyst degradation in PEM fuel cells based on degradation mechanisms such as electrochemical dissolution and re-deposition, Pt migration, Pt ion reduction in membrane, Pt loss, and Pt particle size growth. However, their model failed to predict Pt degradation rate because they believed that other mechanism besides those introduced in the model contributed to Pt degradation as well.

A model was built by Solasi et al. [91] to study the mechanical behaviour of the polymer electrolyte membrane when subjected to hydration and temperature cycles. Shah, Ralph and Walsh [92] built a model that incorporated chemical degradation in PFSA membrane to describe the degradation of the membrane of PEM fuel cells. Their model can be used to describe the chemical degradation of the PFSA membrane comprehensively.

A comprehensively PEMFCs degradation model was built by Whiteley [93], based on a 1-dimensional PEMFC performance model developed by Fly [94], using petri nets modelling techniques to model the degradation phenomenon during different PEMFC operations. This model can calculate the degradation voltage loss caused by each second-based load input of a PEMFC load profile, and therefore, was used in this work to evaluate the degradation contribution of each load input data of a selected real-world operation.

1.3 Experimental-Based PEMFCs Durability Testing Strategies

In terms of experimental strategies to assess durability of PEMFCs, there are two widely used methods, which are lifetime test and Accelerated Stress Test (AST). Lifetime test is a way of assessing the durability of a fuel cell by operating a fuel cell under designed working conditions until the cell reaches

failure level. However, due to the increasing prolonged lifetime of fuel cells, this method is not practical for measuring durability of long-term applications because of its long duration and required resources [95]. To reduce testing time and cost, AST, which facilitate the failure of a fuel cell by increasing stress levels during fuel cell operations, have been widely adopted and utilised by researches to measure fuel cell durability [95]. Two different types of ASTs have been used, which are Accelerated Life Tests (ALT), and Accelerated Degradation Tests (ADTs). ALTs run tests until the overstressed testing segments reach failure level, while ADTs utilise performance degradation data to predict the time when overstressed testing segments fail. All factors that can affect fuel cell performance and durability have the potential to be used as acceleration stressors. The level of which will be increased in ASTs to facilitate the degradation phenomenon during fuel cell operations, and therefore, reduce testing time. At component level, different components have different factors that affect performance and durability, and as a result, accelerated stressors of different component are not identical.

Accelerated life tests are believed to be an effective way to identify different causes of degradation phenomenon. Ramaswamy et al. found that membrane degradation was facilitated when the temperature increased from room temperature to 80 °C, due to accelerated peroxide radical attack, which is resulted from higher ORR rate and increased peroxide generation rate [96]. Some researchers studied the effects of relative humidity on membrane mechanical degradation by cycling relative humidity between 150% and 0% at 80°C, and only air was supplied to both electrodes to isolate any chemical degradation [97]. Membrane failure was observed, and repeated swelling and shrinkage of the membrane was believed to be the major cause of the degradation [97]. Liu and Case evaluated the effects of load cycling on long-term durability of PEM fuel cells by testing two MEAs under a cyclic load profile and a constant load profile separately [98]. Results showed that after 1000h of operation, the cyclic load aged MEA reached its lifetime, and hydrogen crossover was believed to be the most dominant degradation mechanism, while the degradation of the constant load aged MEA was partially recovered, and the lifetime of the MEA was not reached [98]. Although ALTs are effective in identifying possible causes of degradation and failure, it is more suitable for qualitative analyses of understanding the relationship between failure and the applied stress levels.

Accelerated degradation tests are often employed by researchers to predict the durability of a fuel cell as well, and it further reduce testing time compared to ALTs because degradation results can be used for analyses, and the testing cells do not have to reach failure level. Statistical models are used to describe the degradation process and lifetime of fuel cells, and the statistical models consist of two parts: a lifetime distribution that shows the variance in lifetime

of a product, and a life-and-stress relationship that describe how the lifetime distribution varies at different stress levels [99]. Bae, Kim, and Park et al. [100] applied ADTs to compare the performance and predict durability of direct methanol fuel cells by operating test samples at a constant voltage of 0.45V at 60 °C, 70 °C, and 80 °C. They fitted a bi-exponential model to describe the degradation phenomenon of the test cells and produced the lifetime distributions at individual stress level. A Weibull-Arrhenius model was used to represent the relationship between stress levels and lifetime of the cells, and the lifetime distribution of the test cells at designed operating temperature (60°C) was predicted using the relationship. The results shown a good compromise between the predicted and tested lifetime distribution at 60°C. The similar method was applied to PEM fuel cells by Bae, Kim, and Park et al. [101] to predict the durability under startup-shutdown cycles. Different from the direct methanol fuel cells tests, parametric models were applied to fit the degradation data, but could not fit the degradation pathways accurately. Thus, a nonparametric model was used to describe the degradation phenomenon and produce the lifetime distribution at various stress levels. Failure time at designed operating condition was predicted using the time-scale factor of the nonparametric model, and it was concluded that the lifetime predicted by the nonparametric model was more accurate than that predicted by the exponential model.

Researchers have used many different load cycles to simulate PEMFCs being used in various applications. The new European drive cycle (NEDC) has been modified by researchers to adapt PEMFC operations, and the degradation effects have been investigated. Li et al found out that by running the fuel cell NEDC for 200 cycles, the voltage at 0.5A/cm^2 decreased by almost 0.1V [102]. The degradation voltage is too high compared to the DOE target. However, the voltage loss is believed to be reversible, and is mainly caused by excessive water produced, and can be recovered by recovery protocols such as purging. Lin etc. also investigated into the effects of fuel cell NEDC on PEMFC degradation by operating the testing cell continuously for 350h, and the results showed that the degradation rate of from 280h to 350h was higher than that of from 0 to 280h, and higher degradation voltage loss was observed at high current densities [103]. Another research conducted by Lin etc. also proved that the degradation phenomenon was more server at high current densities region [104]. The result showed that after 200 fuel cell NEDC cycles, no apparent voltage loss was observed at OCV or low current density region (lower than 0.2A/cm^2), but at 1A/cm^2, voltage decreased by 0.051V after 200 cycles, and they believed it is due to mass transfer limitations at high current densities [104]. Similar tests were done by Shan etc., and the results showed a similar trend of increasing degradation with increasing current density and was believed to be caused by the excessive water produced at high current densities [105].

Bose et al. utilised the U.S. Department of Energy (DOE) established dynamic load cycling protocol for PEMFCs to evaluate the degradation effects of load cycling of a ten-cell PEMFC stack for 480 hours, and improved performance was observed after 240 hours of operation, and decreased performance obtained after 480 hours [106]. After 480 hours of operation, the voltage decreased by 2.8% compared with the maximum performance, and by extrapolating the degradation rate, the durability of the cell, defined as 10% performance loss by DOE end-of-life criterion, was predicted to be 1700 hours [106]. Liu and Case applied a 16-step cyclic dynamic load cycle to evaluate PEMFC durability for automotive applications and compared the results with that of constant load operations at the highest load output of the dynamic load cycle (1.06 A/cm^2) [98]. The results after 1000 hours showed that even under the constant load condition, the degradation rate obtained were 160 μV/h at the beginning of life and 255 μV/h at the end, which were significantly higher than those of accelerated stress test results obtained from literatures (21 μV/h to 127 μV/h), and under dynamic load condition, the cell reached the end-of-life after 1000 hours of operation [98]. Significantly increased hydrogen crossover was observed after 500 hours operation under dynamic load condition, while the hydrogen crossover rate remained unchanged under constant load condition, which indicated that it was the dynamic operation that facilitated the formation of pinholes and increased hydrogen crossover [98]. It was concluded that mass transport limitation was responsible for the degradation under constant load condition, and was partially reversible, while hydrogen crossover and pinhole formation was the major degradation cause under dynamic load condition [98].

Pei et al. utilised an arithmetic equation that took the effects of load cycling, start-stop cycling, idling operation, high load condition, and air pollution into consideration to simulate PEMFCs being operated under automotive application conditions, and by comparing the 43000 km real-world data obtained from a PEMFC bus running a fixed route every day for about two years with the calculated lifetime, the results showed a good compromise [107]. Based on the model they proposed, the durability of a PEMFC can be predicted with about 300 hours testing time [107].

1.4 Accelerated Stress Test in PEMFCs

This section presented the factors that potentially can be chosen as stressors of PEMFC accelerated stress tests. Theoretically, all factors that can affect the degradation phenomenon in PEMFCs can be used as stressors, and some of the commonly used stressors are introduced in this section.

1.4.1 Temperature

As one of the most critical factors that determining the performance, temperature may facilitate the degradation phenomenon in MEAs of PEM fuel cells. In order to obtain advantages such as improved reaction kinetics, increased CO tolerance and simplified cooling and water management, some researchers are developing PEM fuel cells that can be operated at temperatures above 100°C. However, high temperature may cause some degradation problems to the MEA. In addition, it is also an essential requirement to operate PEM fuel cells at subfreezing temperatures and freeze/thaw cycling with a stable performance before the commercialisation of PEM fuel cells.

High Temperature

Although the PFSA membrane used in PEM fuel cells can remain well-hydrated within an extensive range of operating temperatures from 60 to 80 °C, and Nafion membranes are able to remain thermally stable up to about 150 °C, with further increased temperature the side sulfonic acid groups begin to decompose. Pinholes and tears formed when operating PEM fuel cells at high temperature and will result in mechanical failure of the membrane. Furthermore, temperatures below 150 °C can lead to reduced water content in the membrane, which will result in reduced proton conductivity and facilitated chemical attack on the side chain. Ramaswamy et al. [96] demonstrated that with the operating temperature increasing from room temperature to 80 °C, peroxide radicals were generated with an increasing rate at the interface. Further increase the temperature to elevated (>100°C), Balasubramanian et al [108] reported that the lifetime of a fuel cell was significantly reduced to less than a few hundred hours.

High temperature also has negative effects on the catalyst layer. It has been reported by Borup et al [37] that increasing temperature will accelerate Pt particle size growth. Dam and de Bruijn [109] claimed that higher temperature resulted in higher Pt dissolution rate.

Low Temperature

Operating PEM fuel cells at subfreezing temperatures is another issue that causes degradation of the MEA. Operating at subfreezing temperatures may result in ice formation, which could result in reactant starvation. Especially during cold start-up at subzero temperatures, the ECSA will be covered by ice, which results in local reactant starvation and facilitates carbon support corrosion [110]. Volumetric expansion will occur when ice is formed from water which can cause damage to the components and interfaces.

Freeze/Thaw cycling

It is observed that repeated volume change caused by phase transformation of water under freeze/thaw cycling could negatively affect lifetime of the membrane [108]. There also exists a disagreement on how freeze/thaw cycling affects the performance of the membrane. Researchers observed increased contact resistance between the membrane and the electrode with ionic conductivity remaining unchanged [111]. McDonald et al. reported affected ionic conductivity, mechanical strength, and gas permeability together with unaffected catastrophic failures [112] after freeze/thaw cycling tests.

1.4.2 Relative humidity

Because water content and transport is one of the key factors that determine the conductivity of the membrane, optimising relative humidity is a critical issue for PEM fuel cell operation. Insufficient humidification, excessive humidification and humidification cycling can affect the degradation in the MEA.

Low Humidity

Low humidification makes the membrane brittle and fragile as a result of low water content. In addition, insufficient water content will result in reduced proton conductivity of the membrane. Apart from reducing conductivity and causing mechanical degradation of the membrane, researchers [113-115] observed that low humidity conditions will also accelerate the chemical degradation of the PFSA membrane. As mentioned previously, Coms [30] believed that low humidity is required for hydrogen abstraction from the -SO_3H side group, and therefore very critical for side chain perfluoro-radical propagation to induce main chain scission. Furthermore, degradation of the membrane will be severely facilitated when fuel cell is operated under high temperature and low humidity simultaneously [95]. Beuscher et al. [116] claimed that as the temperature and the relative humidity are always closely related in fuel cell conditions, these two factors should not be discussed separately.

High Humidity

Increasing relative humidity results in increased permeability of the PFSA membrane [117] [118]. Higher permeability leads to more gas crossover to the relative reverse electrodes and will facilitates the formation of peroxide radicals, and therefore, higher chemical degradation. Aoki et al [119] observed higher fluoride emission from their tests, and it is the increased permeability that is believed to be responsible. High humidification may also result in cathode reactant diffusion impeded and increased leaching contaminations from other components.

Excessive humidity also has a negative effect on the catalyst layer. Increased humidity will result in higher catalyst coarsening rates [37]. Xie et al. [46] reported that high humidity resulted in higher rate of Pt migration, and it is explained as water can lower the bonding energy between the metal and support and facilitates the metal migration. Borup et al. [37] found that when keeping other operating conditions constant, Pt particle size increased with increasing humidity level, which is likely due to the reduced particle growth activation energy. Xu et al. [120] claimed that Pt oxidation was facilitated when RH increased from 20% to 72% and did not continuously increase when the RH was above 72%.

Humidity cycling

Some researchers reported that insufficient humidification can result in higher degradation rate than excessive humidification [121] [122], while a different result was obtained by Gore Fuel Cell Technologies [123]. The membrane experiences compression and tension during membrane drying out and dehydrated processes respectively. Therefore, humidity cycling can result in repeated membrane shrinkage and swelling and degrade the membrane faster. To separate membrane mechanical degradation caused by RH cycling from chemical degradation, researchers applied RH cycling from 150% to 0% at 80 °C with air at both electrodes and observed membrane failure resulted from membrane repeated swelling and shrinking [97].

1.4.3 Load Cycling

Utilising PEM fuel cells in automotive application requires the cells to be operated under dynamic load cycling conditions, and it has been proved that cyclic current ageing conditions have a negative effect on membrane degradation, both mechanically and chemically. On one hand, load cycling is believed to be somewhat related to the humidity effect as the amount of water produced increases with increasing current output. Kusoglu et al. [124] believed that in-plane stress should be responsible for the membrane cracks and pinholes formation due to the humidity changes during load cycling operations. On the other hand, load cycling will accelerate the mechanical and chemical degradation of the membrane. Liu and Case [89] compared the hydrogen crossover rate under current cycling operation and constant current operation and found out that the hydrogen crossover rate dramatically increased under current cycling conditions because of pinhole formation in the membrane, while it remained approximately the same under constant current condition. Furthermore, they also found that the fluoride-ion concentrations under current cycling conditions were about 30-fold higher than those under constant current conditions [89].

Load cycling operations will affect the performance of the catalyst layer as well. It was reported by researchers that as the catalysts on the cathode side were more likely to agglomerate than the anode side under the same load cycling conditions, it can be deduced that particle size increases with increasing potential [95]. Besides, the ECSA was observed to decrease more rapidly with increased hydrogen crossover during a load cycling test [125]. Furthermore, researchers proposed that the ageing result was also affected by the average value of the current over the cycle [126] [127].

Potential Control and OCV operations

Although current and potential are related in PEM fuel cell operation, it is necessary to analyse the degradation phenomenon during accelerated testing in terms of potential as potential changes can affect different degradation mechanisms, especially when operating PEM fuel cells under OCV condition.

It was reported by Zhang et al. [95] that potentials lower than 0.9V would most likely affect the Pt catalyst degradation, while higher potentials would increase carbon corrosion. It was proposed by Dam and de Bruijn [128] that higher potentials could accelerate Pt dissolution as they observed an approximately 54-fold increase in Pt dissolution when potential was increased from 0.85V to 1.15V at 80°C. However, further increase in potential may not lead to further increased Pt dissolution due to the formation of a protective surface oxide film [128] [129]. As Pt dissolution can be accelerated by higher potentials, more severe Pt migration, which was believed to be caused by dissolved Pt diffused through the membrane and reduced by the crossover hydrogen near the cathode side, had been observed, especially under OCV conditions [130-132].

It was claimed by Liu and Case [89] that hydrogen crossover rate was increased when operating their test cells under OCV conditions. Inaba et al. [113] believed that oxygen gas crossover, which resulted in formation of hydrogen peroxide was the primary reason for membrane degradation under OCV conditions. Due to the accelerated chemical degradation of the membrane, Liu and Crum observed a massive ionomer loss in the membrane after their OCV degradation tests [133]. The characteristics of the accelerated chemical degradation caused by OCV operations were increased fluoride ion release rate, membrane thinning, reduced OCV, and Pt migration, and were observed by many researchers [87] [134] [135].

Moreover, OCV operation can facilitate carbon support degradation. Makharia et al. [136] experienced an about 5% carbon weight loss during their idle (0.9V vs. RHE) and OCV testing for 2000h. Borup and co-workers [37] demonstrated that carbon corrosion increased with the increasing potential by applying potential cycling to their test cells. Furthermore, although carbon corrosion is less likely to happen at potentials lower than

1.1V (vs RHE) without the presence of Pt in the carbon electrode layer, with the presence of 10% Pt, carbon corrosion is severe at 0.55-0.6V (vs RHE) [51].

Startup/Shutdown cycles

Using PEM fuel cells in automotive applications requires a stable performance and durable lifetime of the cell during startup/shutdown cycles. Startup/shutdown cycling has a significant negative effect on carbon support degradation. The air/fuel boundary, which is also known as partial hydrogen coverage, can occur during both startup and prolonged shutdown processes, and will cause significant performance decay due to loss of ECSA [137] [138]. The effects can be explained as follows: partial hydrogen coverage together with the presence of O_2 at the anode will result in a potential drop at the anode, which can cause an increase of cathode potential to values higher than OCV, and dramatic carbon corrosion will occur [139]. Ballard and Borup demonstrated that insufficient humidification could accelerate carbon corrosion during startup/shutdown cycles [37] [140]. Tang et al. [138] obtained an up to 70% reduction in the cathode ECSA of their test cells when feeding air and fuel to the anode. This sharp voltage change may have some other negative effects on other PEM fuel cells components. However, further investigation is still required to understand the influences.

As introduced in Chapter 1.3, although researchers have successfully facilitated the degradation phenomenon in PEMFCs, and predict the durability in a condensed testing time under accelerated operating conditions, using the accelerated stress test itself still has limitations such as failing to consider the load effects of dynamic operations and may only facilitate degradation affected by the stressor etc. Combining the developed ATC development strategy with the accelerated stress tests can further facilitate the degradation phenomenon and reduce testing time. Furthermore, it also increases the representativity of the testing results and potentially can be more comprehensive and accurate in terms of assessing degradation of different real-world applications.

1.5 Limitations of Testing Strategies in Literature

Summarising the discussed durability testing methods, on one hand, although ASTs have been widely employed by researchers to investigate the relationship between operating conditions and fuel cells degradation phenomenon and reduce testing time and cost, the method has its own limitations. ASTs are effective when qualitatively investigating the effects of a certain operating condition on fuel cell degradation because, as stated by Wu et al. [141], by increasing a stress level, only certain degradation mechanisms that are related to the stressor should be facilitated. However,

due to the sophisticated nature of fuel cell degradation, it is difficult to isolate degradation mechanisms from each other, by accelerating degradation mechanisms related to a single stressor may cause problems when analysing the degradation and predicting the durability of a cell. Furthermore, it is possible that ASTs may induce other degradation mechanisms that are not inherent in normal operating conditions, and therefore cannot represent the degradation phenomenon in real-world operations. ADTs usually utilise statistical models not only to describe the degradation process, but also to predict the lifetime distribution from results obtained from stressed condition to normal use condition. For those products that the degradation modelling has not yet been clearly understood or accurately modelled, the accuracy of the predicted durability cannot be guaranteed. In addition, when applying ASTs, the stressors levels often need to be specified. However, it is not practical to clearly define the load level of a real-world dynamic operation, and therefore, ASTs are not applicable to evaluate the effects of a dynamic operation and predict the durability of a cell.

On the other hand, different dynamic load cycles have been employed by researchers to investigate the effects of dynamic operation on PEMFCs degradation and durability, but according to the published results, most of the tests were analysing overall degradation results that included both reversible and irreversible degradation voltage loss, and the irreversible degradation voltage loss caused by dynamic operation has not been well studied. Moreover, among all the literatures found, apart from the research done by Pei et al. [107], all tests were done by running the dynamic load cycles until the end-of-life, no method has been identified that can accelerate the tests to reduce testing time by condensing the load cycles into shorter but 'tougher' ones. Therefore, due to the nature of prolonged testing time and high costs of predicting PEMFCs durability, a strategy for developing accelerated test cycles for PEMFCs durability evaluation under dynamic load operations is required.

1.6 Literature Review Summary

A PEM fuel cell consists of several components. The basic components to assemble a PEM fuel cell are membrane, catalyst layers, gas diffusion layers, and bipolar plates. The membrane electrodes assembly (MEA) together with the two bipolar plates, which sandwich the MEA in between, is believed to be the core part of a PEM fuel cell. The basic operating principle of fuel cells consists of two main reactions, which are the hydrogen oxidisation reaction, which takes place at the anode side, and the oxygen reduction reaction that occurs at the cathode side. Hydrogen is supplied to the anode side, and with the present of the catalyst, which is usually platinum on high surface area carbon support, hydrogen is oxidised and produce protons and electrons.

Protons are transferred through the membrane to the cathode side, and electrons travel through the outer circuit from anode to cathode and generate electricity. On the cathode side, air is supplied, and the oxygen in the air react with the transferred protons and electrons to produce water and heat.

The theoretical open circuit voltage of a PEM fuel cell can be calculated using the change in the molar Gibbs energy of formation and Nernst equation. During fuel cell operations, there exists different kinds of losses, which are activation losses, fuel crossover and internal current losses, ohmic losses, and mass transport and concentration losses. Each type of loss has been properly model by previous researchers and can be calculated.

Apart from the losses mentioned above, during PEM fuel cell operations, degradation will occur and cause a further reduction in operational voltage. The degradation mechanisms were discussed in detail. It is concluded that membrane mechanical degradation is the main reason for early life failure, and can be caused by congenital manufacturing defects, undesired operating temperature and humidity, non-uniform or high stress, the heat release reaction of oxygen and hydrogen crossover et al. Membrane chemical degradation is caused by the chemical attack of the hydroxyl and peroxyl radicals. Catalyst and catalyst layer degradation is resulted from Pt agglomeration, migration, and dissolution, and carbon support corrosion. The degradation of catalyst and catalyst layer will reduce the electrochemical active surface area, and cause voltage loss. Although the effects of GDL degradation has been evaluated by researchers, the degradation mechanisms of the GDL is still not well understood. GDL degradation will result in hydrophobicity loss, weight loss, and decreased conductivity in GDL. Both graphite and metal can be used as bipolar plates material. In terms of graphite bipolar plates, corrosion is observed under star/stop cycles and fuel starvation conditions. In contrast, metallic bipolar plates experience corrosion and release contamination ions to the system that will facilitate the degradation of other components. The degradation of the sealing gasket will lead to weight loss, silicon and calcium leach, change of surface chemistry, and change of mechanical properties of the gasket.

Some diagnostic technologies, such as polarisation curves and EIS can be used to characterise the performance of a PEM fuel cell to analyse the degradation phenomenon.

The existing methods of evaluating the durability of PEMFCs have been discussed, both model-based prediction and experimental-based test strategies. The model developed by Whiteley [93] is regarded as the most suitable candidate to be used in this work because the model is capable of calculating the degradation voltage loss caused by different load cycles at each input time step. Although durability testing time can be reduced using

the existing experimental-based durability test strategies, by using accelerated stress tests, it is inevitable to introduce new degradations and only accelerate the degradation mechanisms that are related to the stressors. In addition, it is impractical to clearly define the load level of a transient real-world load cycles and therefore, load cannot be chosen as the stressors to accelerate a durability test of a transient real-world operation.

Thus, this work will seek to find a strategy that can condense a prolonged transient real-world application into a short test cycle, by testing which the durability of the original cycle can be accurately predicted.

1.7 Motivation

Although PEMFCs have been regarded as a promising replacement of vehicle internal combustion engines and manufactures, such as Toyota [7], Hyundai [8], and Honda [9], have released hydrogen fuel cell vehicles, barriers to full commercialisation remain, such as performance decay, durability and cost. For automotive applications, the durability requirement for PEMFCs is 5,000h (or 150,000 miles), while the durability requirement for PEMFCs in stationary applications is 40,000-80,000h [10].

As PEMFC components are subjected to a combination of acidic conditions, liquid water, strong reducing and oxidising environment, high temperatures, and high electrochemical potentials, together with load cycling, reactive radicals, high electrical current and large potential gradients, PEMFCs will experience a steady, moderate loss in performance during steady state operation [11]. Furthermore, when subjected to a dynamic operation, the performance loss will be significantly accelerated due to increased degradation phenomenon within the cell. A good understanding of the degradation mechanisms under various operating conditions is essential when evaluating performance durability of PEMFCs.

Due to the prolonged durability requirement of PEMFC applications, it is impractical to test cells for thousands of hours to obtain durability. Although many researchers have applied accelerated stress tests to PEMFCs to reduce testing time and to analyse the degradation phenomenon occurred using a wide range of electrochemical diagnostic tools, the accelerated degradation phenomenon cannot be used to accurately reflect the degradation results of the transient real-world duty cycles. As a result, no test strategy that can evaluate the degradation effects of transient real-world duty cycles, while reducing testing time simultaneously, has been demonstrated. Therefore, it provides the urgency and possibility for a research on developing a fast test strategy for PEMFCs durability measurement against real-world duty cycles.

1.8 Aim & Objectives

The aim of this work is to develop a fast test strategy to reduce PEMFC durability test time by condensing a prolonged real-world dynamic operation into an intense test cycle, by testing and analyse the degradation voltage of which, the degradation voltage caused by the original real-world operation can be predicted.

The main aim of the thesis will be achieved by satisfying the following objectives:

- Understand the operation principles and degradation mechanisms of PEM fuel cells.
- Understand currently employed PEMFC durability test methods in the literature and identify the advantages and limitations of the existing methods.
- Obtain a PEMFC degradation model that can accurately calculate the degradation voltage caused by a dynamic PEMFC operation by time step.
- Condense a dynamic PEMFC operation into an intense test cycle.
- Utilise the condensed test cycle to predict the degradation voltage of the original cycle with reduced testing time.
- Validate the strategy with experimental results where appropriate.
- Prove the universality of the strategy and apply it to a real-world scenario.
- Explore possibility of further reduction of testing time.

1.9 Layout of Remaining Thesis

The remaining chapters of the thesis are listed below.

Chapter 2 – PEMFC Model Introduction. In this chapter, the PEMFC performance model and the petri nets degradation model developed by previous researchers are introduced. The model is modified and used in this work to calculate the degradation voltage of different input load cycles.

Chapter 3 – ATC Development Procedure. In this chapter, the process of developing a WLTP-based ATC is introduced in detail. The degradation voltage loss of the original WLTP operation is predicted using the developed ATC. The ATC development strategy is validated using experimental results.

Chapter 4 – ATC Development Strategy Sensitivity Analysis. The sensitivities of the developed strategy in terms of different targeted real-world operations,

different selection criteria applied, and different models used are analysed to evaluate the universality of the strategy. The sensitivity of the strategy to different selection criteria applied will be validated using experimental results.

Chapter 5 – Applying the Developed Strategy to RDE. In this chapter, the ATC development strategy will be applied to RDE cycles to prove the feasibility and accuracy of the strategy in a real-world scenario.

Chapter 6 – Combining Accelerated Stress Test with ATC Development Strategy. The developed strategy is combined with standard accelerated stress test strategy to further reduce PEMFC durability testing time.

Chapter 7 – Conclusions and Future Work. The final chapter summarise the results of the previous chapters and conclude the main findings of the work. Recommendations for possible future works will be made.

Chapter 2

2 PEMFC Modelling Introduction

2.1 Introduction

In this chapter, the fuel cell model used in this research is used to represent a PEM fuel cell system, and the Petri Nets model simulating the degradation phenomenon occurred during PEM fuel cell operations is explained in detail.

2.2 0 – Dimensional FC Model

The fuel cell performance model used in this study is a 0-dimension model based on a semi-empirical equation and calculates the operational voltage by subtracting losses from the theoretical open circuit voltage [93]. The equation for theoretical open circuit voltage calculation is shown in equation (2.1):

$$OCV = -\frac{\Delta\bar{h}-T\Delta\bar{s}}{2F} + \frac{RT}{2F} ln\left(\frac{p_{H_2} p_{O_2}^{\frac{1}{2}}}{p_{H_2O}}\right) \quad (2.1)$$

Where;

$\Delta\bar{h}$ is the change in enthalpy of the electrochemical reaction with liquid water as a product at standard temperature and pressure (STP),

$\Delta\bar{s}$ is the change in entropy of the electrochemical reaction with liquid water as a product at standard temperature and pressure (STP),

T is the cell temperature,

R is the universal gas constant,

F is Faraday's constant,

p_{H2}, p_{O_2}, and p_{H_2O} are the pressures of H_2, O_2, and H_2O, respectively.

The losses are grouped into four pathways: activation, fuel crossover, mass transport, and ohmic losses. Activation losses and fuel crossover losses are combined and calculated using equation (2.2).

$$V = \frac{RT}{2\alpha F} \ln\left(\frac{i+i_n}{i_0}\right) \quad (2.2)$$

Where;

R is the universal gas constant,

T is the cell temperature, α is the charge transfer coefficient,

F is Faraday's constant,

i is the current density,

i_0 is the exchange current density,

i_n is the internal current density.

Because the mass transport losses is determined by many factors, such as operating stoichiometry, cell geometry, and presence of liquid water, predicting mass transport losses analytically is complicated, therefore, the mass transport losses are calculated using an empirical equation as shown in equation (2.3) [93].

$$V_{mass} = m_{trans} * e^{i*n_{trans}} \quad (2.3)$$

Where m_{trans} and n_{trans} are constants, the value of which are typically about 3 X 10^{-5} V and 8 X 10^{-3} cm^2mA^{-1} respectively, but can be chosen accordingly to make a better fit to the results.

The ohmic losses in the cell follow ohm's law, as shown in equation (2.4):

$$V_{Ohmic} = i * r \quad (2.4)$$

Where r is the membrane protonic resistance in ohms.

Only membrane protonic resistance is used because the electronic conductivity of the outer circuit is much higher than the ionic conductivity of the membrane and therefore the electronic resistance can be assumed to be negligible [93].

The water content in the membrane can significantly affect the movement of protons in the membrane and therefore, influence the membrane protonic resistance. An empirical relationship describing the conductivity of a Nafion 117 membrane as a function of water content at 30°C is shown in equation (2.5), and its corrections for temperature variations, equation (2.6), were utilised to calculate the membrane resistance using equation (2.7) [93].

$$\sigma_{30} = 0.005139\lambda - 0.00326 \quad \lambda > 1 \quad (2.5)$$

$$\sigma = \exp\left(1268\left(\frac{1}{303} - \frac{1}{T}\right)\right)\sigma_{30} \quad (2.6)$$

$$r = \int_0^{t_{mem}} \frac{1}{\sigma} dz \approx \frac{t_{mem}}{\sigma} \quad (2.7)$$

Where;

σ_{30} is the conductivity of a Nafion 117 membrane at 30°C,

λ is membrane water content,

T is cell temperature,

t_{mem} is membrane thickness,

and r_e is membrane protonic resistant.

By subtracting the losses from the theoretical open circuit voltage, the operational voltage is calculated using equation (2.8).

$$V_{op} = OCV - (V_{Act+FCO} + V_{mass} + V_{Ohmic}) \quad (2.8)$$

The parameters chosen for the fuel cell model are either from literatures or based on the testing conditions used in this work and are shown in Table 2-1. Working environmental parameters such as temperature, relative humidity, and pressure are determined from experimental conditions.

Table 2-1- List of Parameters Used in the Model

Parameter Name	Value	Unit	Ref
Area of the Cell	25	cm2	
Membrane Thickness	$6X10^{-6}$	m	
Mass Transport Coefficient 1	$3X10^{-4}$	V	93
Mass Transport Coefficient 2	3	cm^2/A	93
Internal Current Density	$1.5X10^{-4}$	A/cm^2	93
Charge Transfer coefficient	0.5		93
Dry Density of Membrane	$1.98X10^{-3}$	kg/m^3	92
Molar Mass of Membrane	1.1	kg/mol	92
Exchange Current Density at STP	$3.2X10^{-8}$	A/cm^2	92
Activation Energy for Oxygen Reduced Cathode	0.066	J/mol	92

The 0-dimentional PEMFC model was built using Simulink software and the overview of the model was presented in Figure 2.1. The Matlab codes that calculate each degradation mechanism was contained in the Appendix.

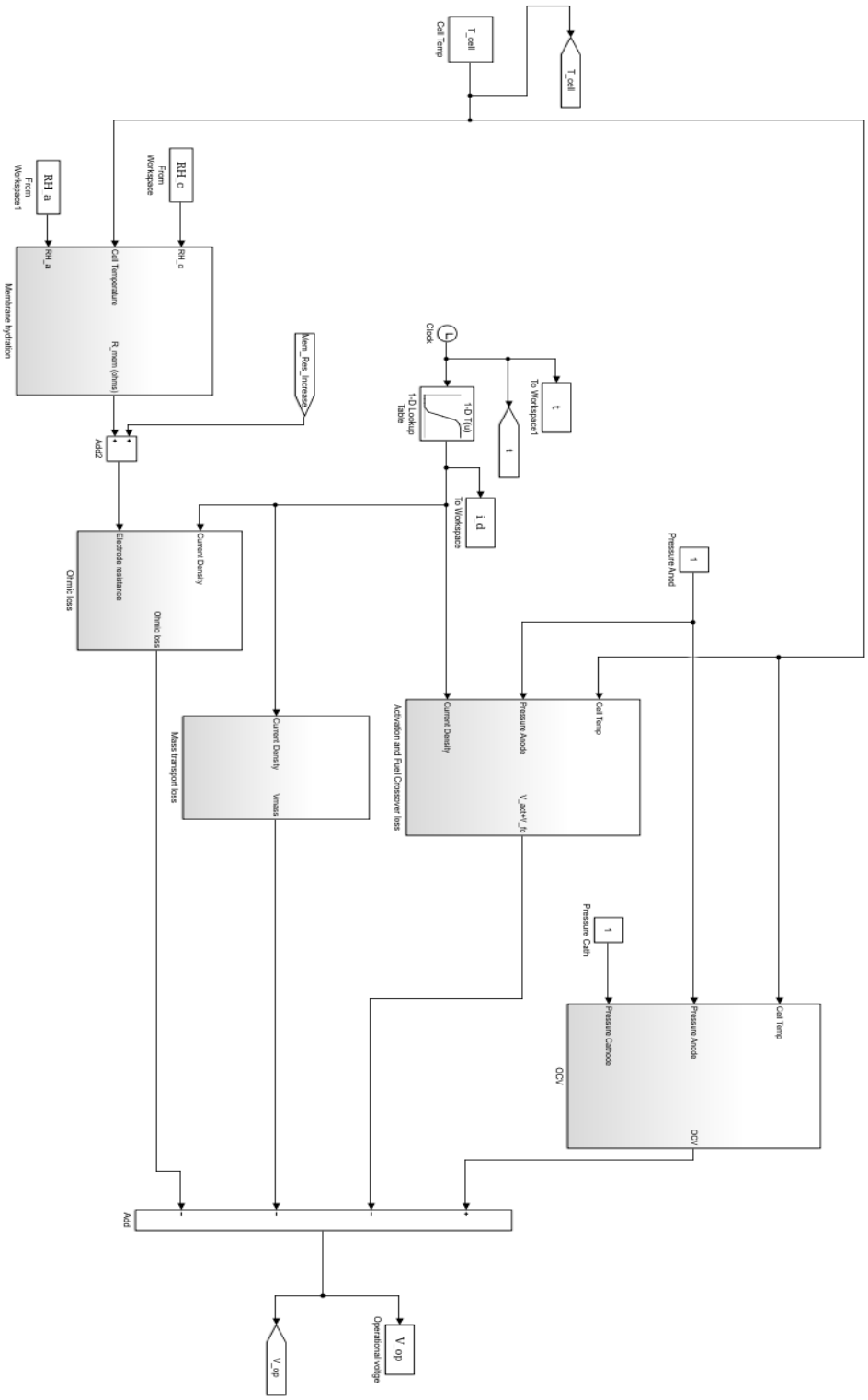

Figure 2.1 – An overview of the PEMFC performance model

2.3 Degradation Model

2.3.1 Petri-Nets Degradation Model

The degradation model used in this research is based on the Petri Nets model developed by Whiteley [92]. Petri Nets modelling is a modelling approach that contains both mathematical and graphical expression to describe the relationship between conditions and events. The advantage of Petri Nets compared with Fault Tree Analyses is that it can cope with relationships and dependencies when modelling and analyse dynamic operations of a system [93].

There are two main symbols contained in Petri Nets, which are 'places (P)' and 'transitions (T)'. 'Arcs (A)' are arrows that are used to connect places and transitions. The direction of arcs indicates the direction of 'tokens' flow. Tokens are transferred between places and transitions through arcs to enable a place and represent the state of the system. Places can represent different working states of a system, and transitions stand for the system transferring from one working state to another. If the pre-defined transition conditions are met, tokens will be transferred from places to places through arcs and transitions. A simple example of a Petri Nets is shown in Figure 2.2.

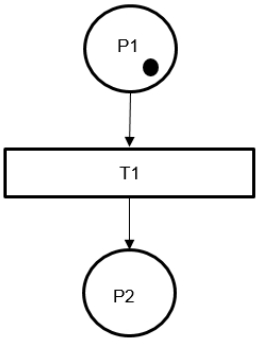

Figure 2.2– An example of a Petri Nets

In this example, at the beginning, P1 has a token in it indicating that the cell is fresh and has no degradation. According to the degradation mechanisms, if the predetermined firing conditions of T1 are met, token will be transferred from P1 to P2 through T1, representing degradation is happening, and the system working state is changed from 'no degradation' to 'degradation occurred'.

The example shown in Figure 2.2 is a graphical expression of Petri Nets and can be mathematically represented by matrixes. Marking matrix shows the current state of the system, and transition matrix represents the movement of tokens.

The starting marking matrix of the above example is shown in equation (2.9) below. It shows that at the starting point, there is a token in P1 and no token in P2.

$$P = \begin{pmatrix} 1 \\ 0 \end{pmatrix} \tag{2.9}$$

When the predetermined firing conditions of T1 is met, then T1 is fired, and token will be transferred from P1 to P2. The transition matrix used to describe this token movement is shown in equation (2.10).

$$\begin{matrix} & T1 \\ P1 & \begin{pmatrix} -1 \\ 1 \end{pmatrix} \\ P2 & \end{matrix} \tag{2.10}$$

This matrix stands for a token being removed (-1) from P1 and placed (1) into P2 when T1 is fired. By completing the firing of T1 and the movement of token, a new marking matrix will be generated and is shown in equation (2.11).

$$P = \begin{pmatrix} 0 \\ 1 \end{pmatrix} \tag{2.11}$$

The firing of the Petri Nets and the mathematical relationship between marking matrix and transition matrix are described in equation (2.12).

$$M_n = M_0 + A^T \tag{2.12}$$

Where: M_n is the final marking matrix, M_0 is the starting marking matrix, and A^T is the transition matrix.

The degradation model developed for this research modelled 12 degradation mechanisms covering membrane degradation, catalyst and catalyst layer degradation, GDL degradation, and BPP degradation. The model is used under laboratory operation conditions, and therefore, it is assumed that the operating temperature is within the normal operating range of PEM fuel cells (60 °C - 100 °C), and the inlet gases of the both electrodes are humidified. Degradation caused by extreme operating conditions, such as ice formation or dry operating of the cell, are not considered in this model but can be added in the future.

Each degradation mechanism is represented by a Petri Nets graph to describe the process of the degradation. Transfer of tokens among places and firing of

transitions are modelled using matrixes written in Matlab scripts. The Petri Nets graph of pinholes formation is shown in Figure 2.3 [92] as an example.

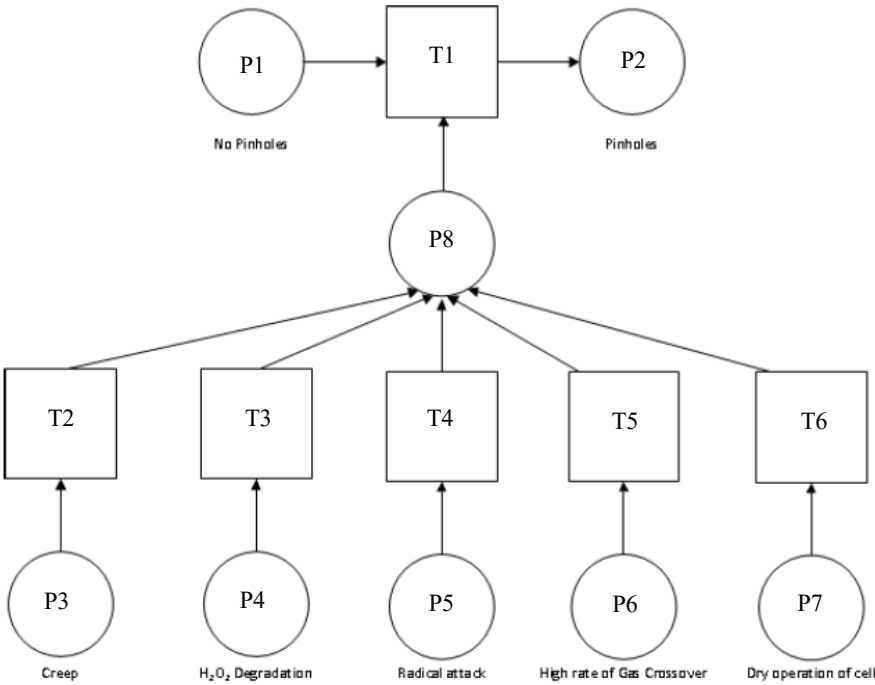

Figure 2.3 - Pinholes Petri Net Module [92]

Initially, a token is placed in P1 upon first iteration of the model, representing there is no pinhole formation in a fresh cell. When P8 obtains a token, which can be transferred from P3 through to P7, T1 will be fired, and the token in P1 will be transferred to P2. This indicates pinhole formation.

As described in the previous equation, the transition matrix of formation of pinholes is shown in equation (2.13).

$$A^T = \begin{array}{c} \\ P_1 \\ P_2 \\ P_3 \\ P_4 \\ P_5 \\ P_6 \\ P_7 \\ P_8 \end{array} \begin{array}{c} \begin{array}{cccccc} T_1 & T_2 & T_3 & T_4 & T_5 & T_6 \end{array} \\ \begin{pmatrix} -1 & 0 & 0 & 0 & 0 & 0 \\ 0 & -1 & 0 & 0 & 0 & 0 \\ 0 & 0 & -1 & 0 & 0 & 0 \\ 0 & 0 & 0 & -1 & 0 & 0 \\ 0 & 0 & 0 & 0 & -1 & 0 \\ 0 & 0 & 0 & 0 & 0 & -1 \\ -1 & 1 & 1 & 1 & 1 & 1 \\ 1 & 0 & 0 & 0 & 0 & 0 \end{pmatrix} \end{array} \tag{2.13}$$

In the above matrix, a '1' indicates placing a token into a place, while a '-1' indicates removing a token from a place.

The Petri Nets degradation mechanisms are modelled using Simulink and integrated with the 0-dimension fuel cell model to simulate fuel cell operation. Each of the 12 degradation mechanisms has an individual Petri Nets graph and corresponding matrix representations. The matrixes are written in Matlab script and the scripts are grouped according to different components where the degradation phenomenon happens.

2.3.2 Degradation Rates

For every time step, all of the Petri Nets modules will be enabled to determine whether the transition is fired or not. The output of the Petri Nets simulations is either 0, representing the degradation mechanism is not happening, or 1, indicating the degradation mechanism is occurring. To quantitatively analyse the effects of the degradation mechanisms, the output of each Petri Nets module will be multiplied by a corresponding degradation rate, which is either determined from literatures or is proposed based on experience. However, in real world operations, it is always not the case that the degradation rates stay constant during the lifetime of the cell. To estimate the real-world degradation levels using constant degradation rates, it is assumed that for each degradation mechanism, $\mu(t)$ follows a Weibull distribution;$\mu(t) = 1/\lambda(t)$, where $\lambda(t)$ is the degradation rate [41]. The probability function is shown in the equation (2.14) below.

$$F(t) = \frac{\beta}{\alpha}\left(\frac{t-\gamma}{\alpha}\right)^{\beta-1} e^{-\left(\frac{t-\gamma}{\alpha}\right)^{\beta}} \tag{2.14}$$

Where β is the shape parameter, α is the scale parameter, and γ is the location parameter.

The shape parameter equals to the slope of the line in a probability plot. The scale parameter is determined by

$$\alpha = \frac{\mu(t)}{\Gamma\left(1+\frac{1}{\beta}\right)} \tag{2.15}$$

Where:

$$\Gamma(\alpha) = \int_0^{\infty} t^{\alpha-1} e^{-t} dt \tag{2.16}$$

In this study, 0 is chosen for the location parameter γ because it is assumed that all degradation starts at the starting of lifetime of the cell.

The Weibull distribution data and degradation rates used for different degradation mechanisms were obtained from literatures and listed in Table 2-2 below. Some of the data listed were not obtained directly and were recalculated from results figures.

Table 2-2 - Weibull Distribution Data Used

Degradation Mechanism	Degradation Rate	Scale Parameter	Gamma Function	Shape Parameter	Reference
	$\lambda(t)$	α	$\Gamma(\alpha)$	β	
Immature Pt Agglomeration					
a Cell V > 0.8	4.356×10^{-7}	4.248×10^{6}	1.13	0.8	
b Cell V between 0.8 &0.65	2.837×10^{-7}	2.549×10^{6}	1.13	0.8	[161]
c Cell V between 0.65 &0.41	2.281×10^{-7}	3.278×10^{6}	1.13	0.8	
d Cell V < 0.41	4.89×10^{-8}	1.275×10^{7}	1.13	0.8	
Mature Pt Agglomeration					
a Cell V > 0.9	6.23×10^{-9}	1.420×10^{8}	1.13	0.8	
b Cell V between 0.9 &0.8	7.79×10^{-9}	1.136×10^{8}	1.13	0.8	[92]
c Cell V between 0.8 &0.65	9.34×10^{-9}	9.475×10^{7}	1.13	0.8	
d Cell V < 0.65	1.56×10^{-9}	5.673×10^{8}	1.13	0.8	
Peroxide Attack					
a Normal Rate	3.31×10^{-8}	3.112×10^{6}	0.89	2	[112]
b w/Fe+ presence	8.96×10^{-8}	1.886×10^{6}	0.89	2	
c w/High Gas Crossover	1.27×10^{-7}	1.556×10^{6}	0.89	2	
Radical Attack	3.61×10^{-7}	3.112×10^{6}	0.89	2	[92]
Carbon Corrosion	2.77×10^{-8}	4.045×10^{7}	0.89	2	[51]
Pinholes	1.6×10^{-5}	7.022×10^{4}	0.89	2	[162]
Creep	2.77×10^{-8}	4.045×10^{7}	0.89	2	[92]
High Gas Crossover	2.77×10^{-8}	3.186×10^{5}	1.13	0.8	[92]
Low Gas Crossover	0	0	0	0	[92]
GDL Degradation	3.33×10^{-7}	3.374×10^{3}	0.89	2	[92]
BPP Degradation	8.796×10^{-7}	1.277×10^{6}	0.89	2	[92]
Flooding	5.972×10^{-5}	1.674×10^{4}	1	1	[92]

The degradation rate of low gas crossover was zero because gas crossover was believed to be inevitable in a PEMFCs, and the degradation voltage caused by low gas crossover was negligible. However, it was regarded as one

of the trigger conditions of other degradation mechanisms and therefore, was modelled using Petri Nets and listed in Table 2-2.

2.3.3 Model Modifications

Before the Petri Nets degradation model developed by Whiteley [92] was utilised in this research, the model was modified to enable it to predict the degradation effects of different operating temperatures more accurately. Operating temperature was used as a input of the Petri Nets modules of some degradation mechanisms in the model, such as membrane creep and excess heat. The original model was able to respond to temperature changes and model different degradation phenomenon at different temperatures The Petri Nets graph of membrane creep was presented in Figure 2.4 below.

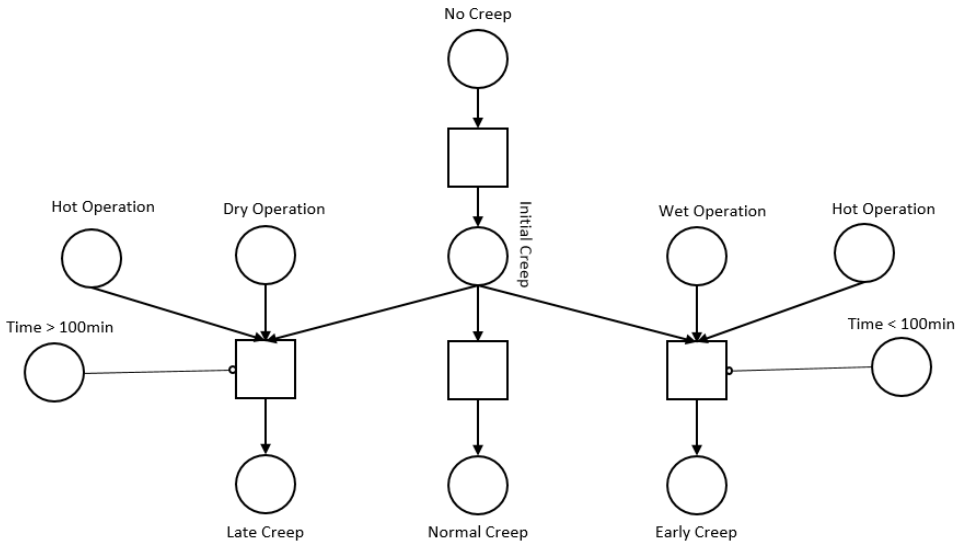

Figure 2.4 – Membrane creep Petri Nets graph [92]

The 'hot operation' in the membrane creep degradation mechanism was defined as operations at higher than 85°C. When the operating cell temperature is higher than 85°C, with varied humidity conditions and operation time, different level of creep will happen, resulting in varied degradation rates.

To quantify the effects of varied operating temperature on degradation phenomenon, other Petri Nets modules were modified. Researchers reported that by increasing operating temperatures, the degradation phenomenon of carbon corrosion, Pt dissolution, and membrane damage were facilitated [142-145]. The degradation of carbon support was observed when cell temperature was over 60°C and significantly increased when cell temperature increased from 60°C to 90°C [143]. A dramatic increase in Pt dissolution rate

at the same dissolution potential when cell temperature increased from 60°C to 80°C was reported, following the same trends of the increase in carbon corrosion [144]. As reported in literatures, when a PEMFC is exposed to cyclic load cycles with temperature increasing from 40°C to 60°C and further to 80°C, carbon corrosion, Pt agglomeration, loss of ECSA, and Pt migration were facilitated [145]. The degradation voltage loss was quantified and found out to be increased from 4.0 μV/cycle at 40°C to 14.7 μV/cycle at 60°C, and further increased to 29.5 μV/cycle at 80°C. Although the same trend of increased degradation rates with increasing operating temperatures were reported by researchers, the number of literatures that clearly quantified the degradation voltage loss caused by individual degradation mechanisms were rare. Therefore, to accurately model the effects of operating temperature on degradation, the degradation rates of the temperature – sensitive degradation mechanisms used were functions of temperature rather than constant values.

The degradation rates used in the Weibull distribution calculation modules of immature and mature Pt agglomeration and carbon corrosion were changed from constant values into a linear function of operating temperature. The ratio between degradation rates and temperature was estimated from literature, and the degradation rates listed in Table 2-2 were regarded as the degradation rates at 60°C. The degradation rates at 80°C was 2.84 times that at 60°C [145], the calculation of degradation rates at different temperatures was expressed in equation (2.17), and this equation only calculated the degradation rates of operating temperatures higher than 60°C.

$$DR_T = (0.07 \times T - 3.2) \times DR \tag{2.17}$$

Where DR is the degradation rate at 60°C, T is the operating temperature, and DR_T is the degradation rate at temperature T, and $T \geq 60$°C.

The modified Weibull calculation block of carbon corrosion was represented in Figure 2.5 below.

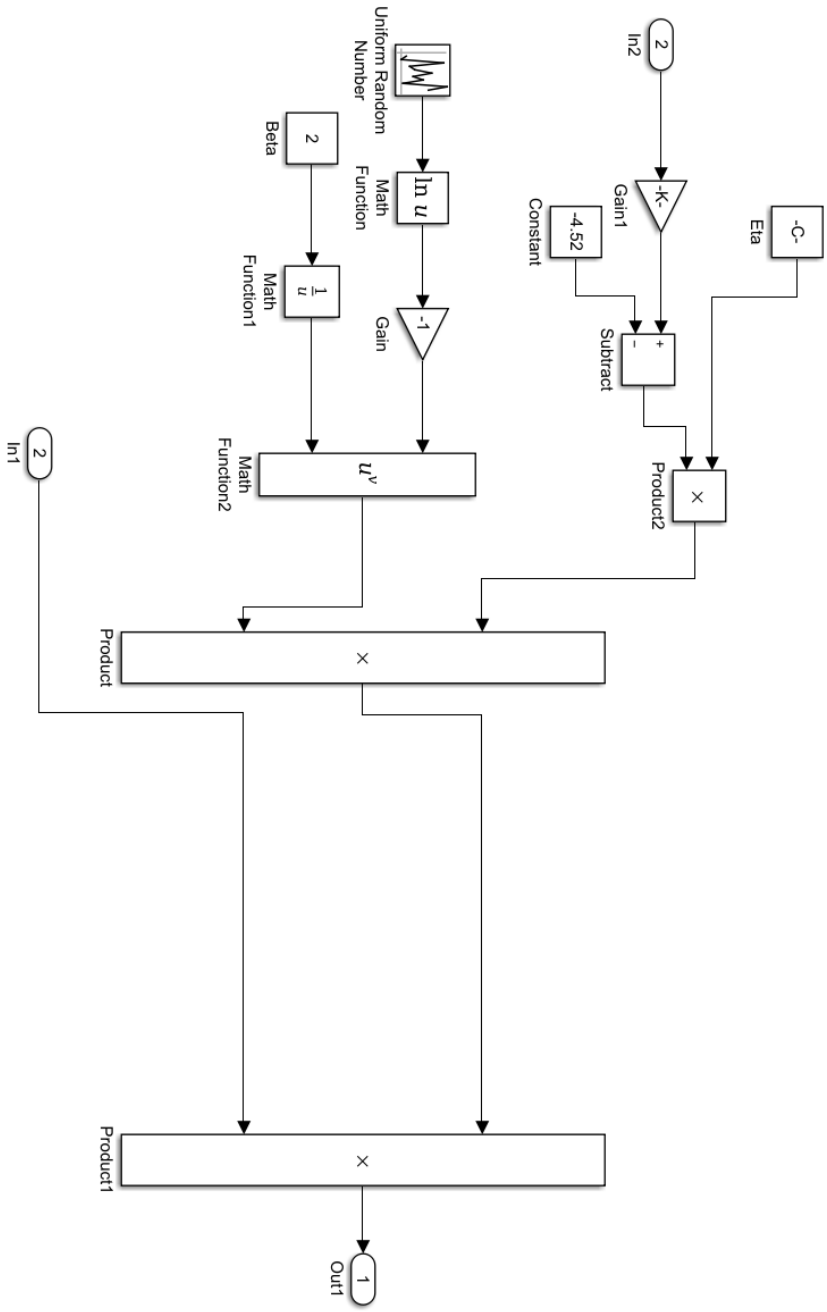

Figure 2.5 – Modified carbon corrosion Weibull calculation block

The two inputs (In1 and In2) in Figure 2.5 were the output of carbon corrosion petri nets block and the operating cell temperature respectively. Eta represented the degradation rate of carbon corrosion at 60°C, and the output of the Weibull calculation block was the degradation rates of carbon corrosion at a certain operating temperature. The same Weibull calculation blocks were

used for immature and mature Pt agglomeration degradation rates calculations with different Eta.

2.4 Combined Model and Model Variations

To simulate the operation of a PEMFC, the 0-D fuel cell performance model and the petri nets degradation model were combined to calculate the cell voltage during different PEMFC operations.

The cell voltage is calculated by subtracting degradation voltage loss, calculated from the petri nets degradation model, from the operational voltage as described in equation (2.18) below.

$$V_{cell} = V_{op} - V_d \tag{2.18}$$

Where V_{op} is the operational cell voltage and V_d is the degradation voltage.

When modelling the degradation phenomenon using the petri nets model, all degradation mechanisms are assumed to cause voltage loss at all current densities, which is not the case in real world. Some degradation mechanisms are believed to be load dependent, while some are not. For example, the degradation of the bipolar plates is believed to be load dependent and will result in increased resistance, while the degradation caused by reactant gas crossover and pin holes is not load dependent and only affect internal current density [146]. A modelling method that can separate the various effects of degradation at different load regions is ideal. However, due to the unavailability of other models, the presented Petri Nets degradation model was adopted to model the degradation phenomenon, and the assumption that all the degradation mechanisms would cause voltage loss at all current densities was made.

2.4.1 Model Variations

Due to the unavailability of other degradation models, the petri nets degradation model was modified and regarded as a different model. The original model and the modified model were used to analyse the sensitivity of the strategy to different models. The modified Simulink modules of the model were presented and compared with the original ones in from Figure 2.6 to Figure 2.9. The mature and immature Pt agglomeration blocks were merged and simplified into one Pt agglomeration block, as presented in Figure 2.6 and Figure 2.7. In the original model, the peroxide attack block took the effects of operating voltage into account by using different degradation rates for different voltage range, and in the modified model, the voltage effects were ignored and only one constant degradation rate was used. This is

illustrated in Figure 2.8 and Figure 2.9. In addition, membrane creep block was removed from the model.

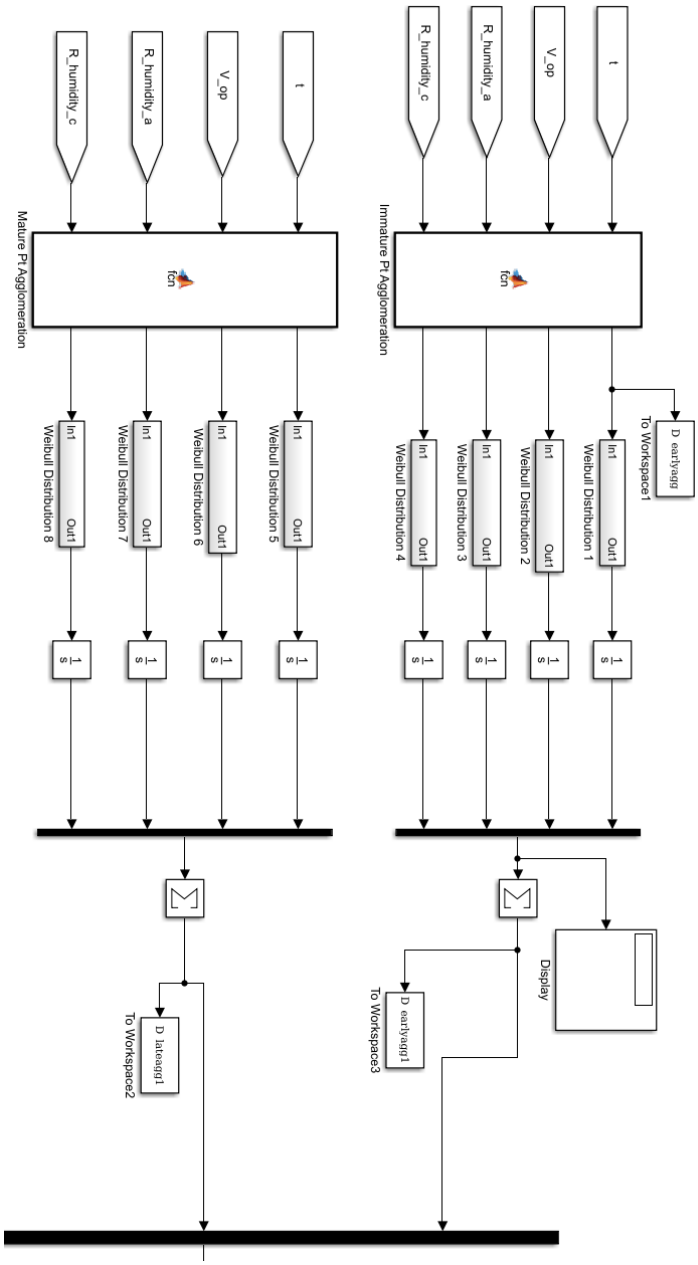

Figure 2.6 – Original Pt agglomeration Petri Nets block

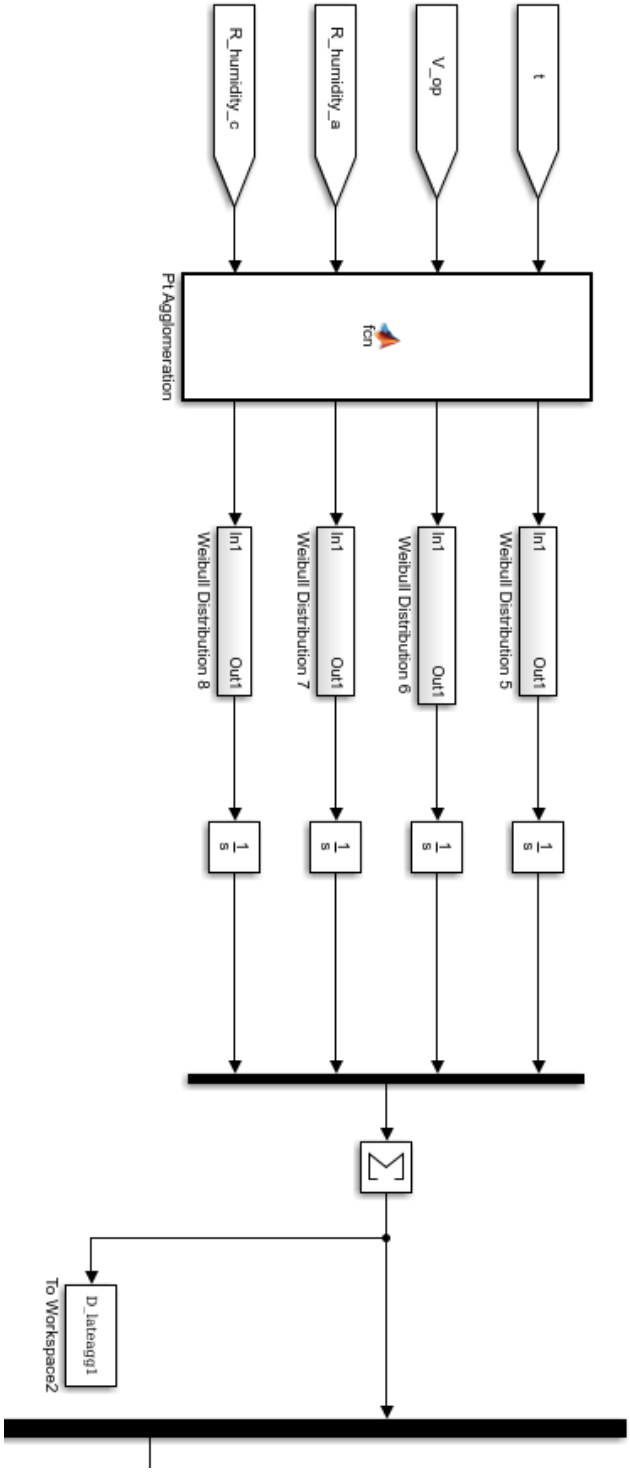

Figure 2.7 – Modified Pt agglomeration Petri Nets block

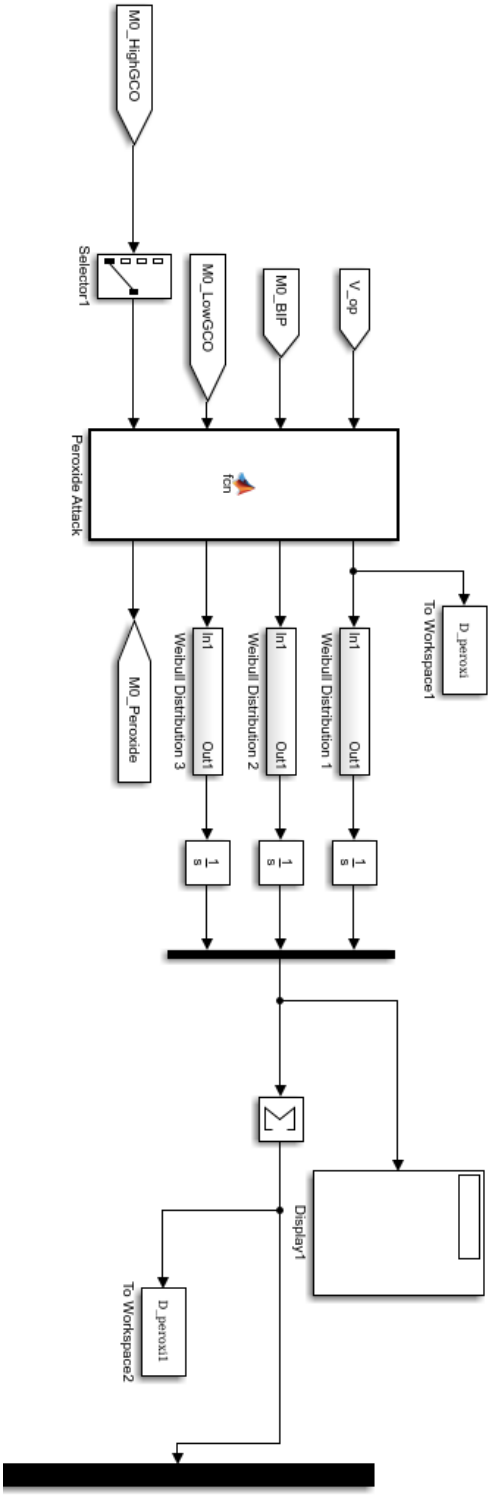

Figure 2.8 – Original peroxide attack Petri Nets block

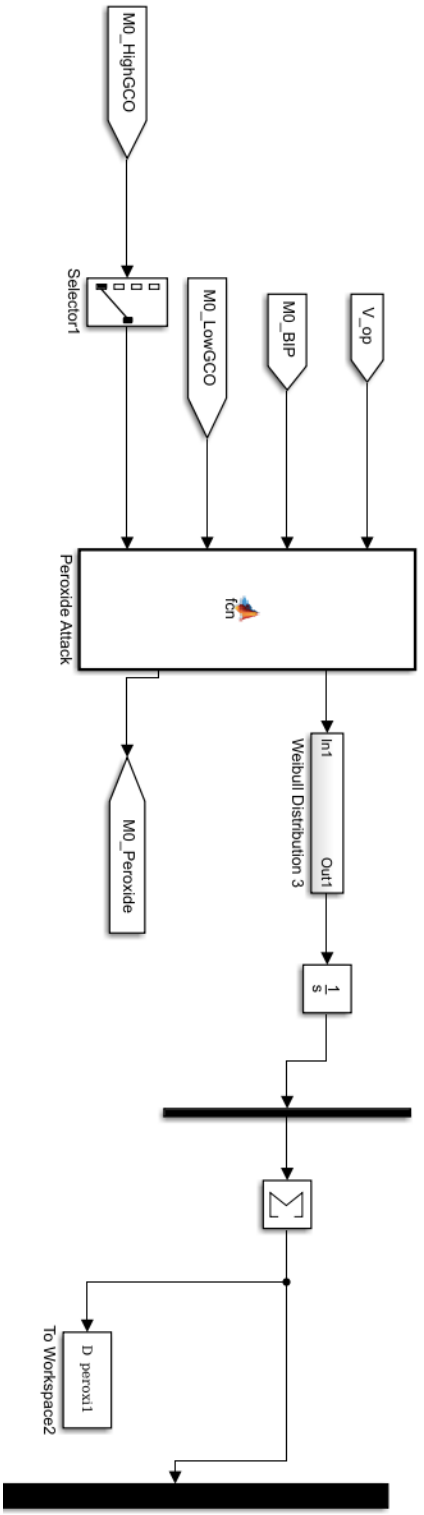

Figure 2.9 – Modified peroxide attack Petri Nets block

The original model and the modified model are referred as Model 1 and Model 2 separately in the following context. Both Model 1 and Model 2 were validated using experimental results and accuracy will be compared in Chapter 3, and the simulation results of the two models were compared and analysed in Chapter 4.4.

2.5 Conclusions

In this chapter, the model used in this work was introduced. The model was based on a PEMFC performance and degradation model built by previous researchers. The model represents a 0-dimensional PEMFC performance model governed by Nernst equation and losses calculations. Degradation phenomenon was modelled using Petri Nets modelling techniques. An existed Petri Nets degradation model was modified and enabled to predict the difference in degradation voltage loss at different operating temperatures. Degradation rates were updated based on literatures to increase accuracy. The model was simplified and regarded as a second model with different accuracy to be used for comparison. The two models will be validated through experimental tests in the next chapter.

Chapter 3

3 Accelerated Test Cycle Development Procedure

3.1 Introduction

The target of this research is to develop a strategy to develop accelerated test cycles from real-world operations. The inputs of the strategy are real-world application and selection criteria, and the outputs are the developed accelerated test cycle with its acceleration factor.

Figure 3.1 presents a flow diagram depicting the logic process of this work.

A Real-world duty cycle was firstly converted into fuel cell load cycles by matching the power output of the duty cycle with the power output of a PEMFC. By using standardised PEMFC polarisation curve and power curves, PEMFC current and voltage output can be identified.

The load cycle was then simulated using a PEMFC degradation model until the degradation voltage loss reached the predefined failure condition. In this research, the time step of simulation was set to 1 second, and according to the widely accepted durability target of PEMFCs applications, failure was defined as when a cell lost 5% of its beginning of life performance [11]. Therefore, failure condition of the simulation was defined as when the cumulative total degradation voltage reaches 0.05V because it was expected that the OCV of a PEMFC used in real world was about 1V due to losses [11].

The degradation model calculated the degradation voltage caused by each time step of the load cycle. The total cumulative degradation voltage loss, represented by DV 1 in Figure 3.1, could be calculated by summing up the degradation voltage loss of all the time steps, as described in equation (3.1).

$$DV\ 1 = \sum Degradation\ Voltage\ of\ each\ step \tag{3.1}$$

Degradation rate of each time step could also be obtained by subtracting the total degradation voltage loss at the end of the time step by that at the end of the previous time step. Equation (3.2) described how degradation rates of time step n was calculated. The degradation voltage at 0 time step was 0.

$$DR_n = DV(n) - DV(n-1) \tag{3.2}$$

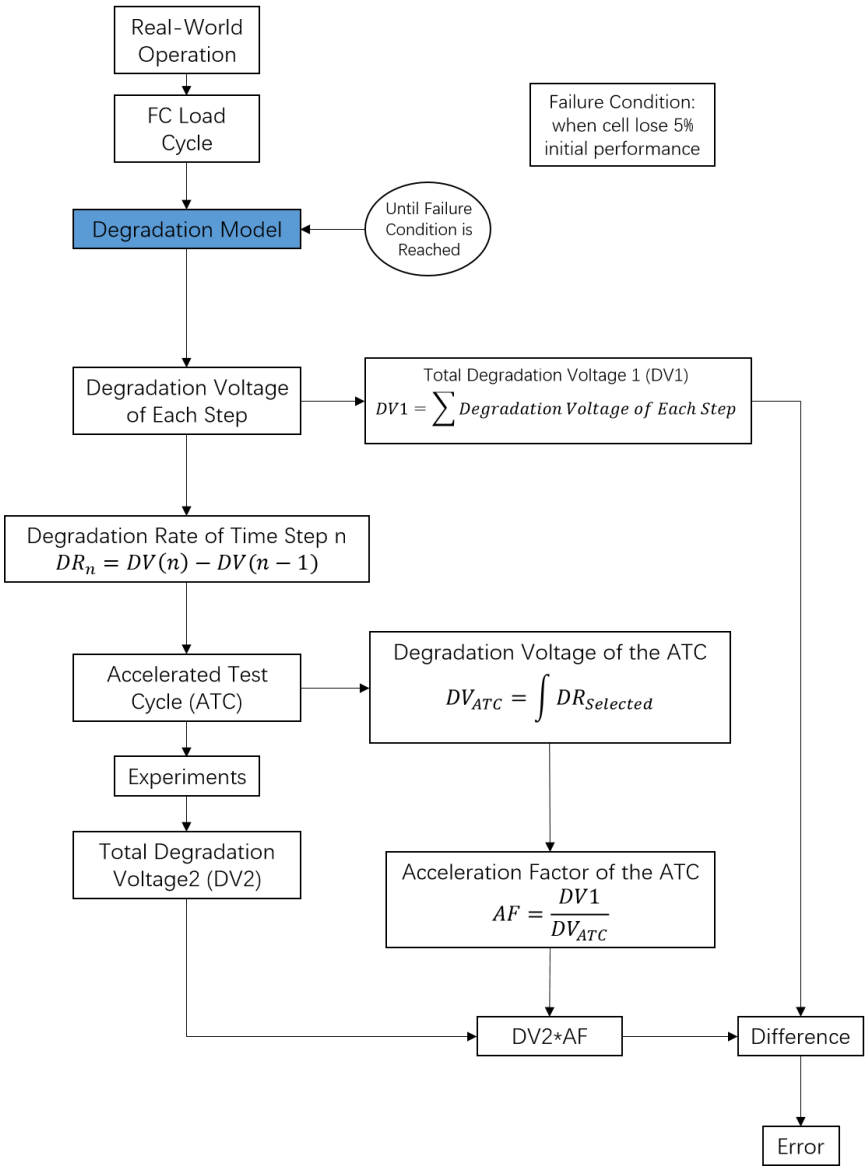

Figure 3.1 - Flow diagram of accelerated stress test formulation and comparison logic

Then time steps were selected according to the pre-defined selection criteria, if the degradation rate of a time step was higher than the selection criteria, the step was selected, and the load information of the step was used to develop the accelerated test cycle. The ATC was developed by connecting the selected steps in series. The degradation voltage loss remaining in the ATC was calculated by integrating the degradation rates of the selected time steps, as shown in equation (3.3).

$$DV_{ATC} = \int DR_{Selected} \tag{3.3}$$

Equation (3.4) presented the calculation of the acceleration factor; the ratio between the degradation voltage loss caused by the real-world operations and that caused by the ATC. With the increasing of the AF, the level of the condensation is increased, and shorter the developed ATC.

$$AF = \frac{DV\,1}{DV_{ATC}} \tag{3.4}$$

The developed ATC was then tested through experiments. The tested degradation voltage loss of the ATC was shown as DV2 in Figure 3.1. By multiplying DV 2 by the calculated acceleration factor, the degradation voltage loss of the real-world load cycle could be predicted as shown in equation (3.5) and was expected to be the same as DV 1.

$$DV_{Predicted} = DV2 \times AF \tag{3.5}$$

The difference between DV 1 and DV 2 was regarded as the error.

3.2 Accelerated Test Cycle Development Strategy

The ATC development strategy was divided into 5 sections, which are fuel cell cycles conversion, degradation simulation, step selection, ATC construction and acceleration factor calculation, and degradation voltage prediction and error analysis. In this chapter, WLTP Class 3 vehicle drive cycle was used as a representative of real-world applications. The WLTP time to speed profile was presented in Figure 3.2.

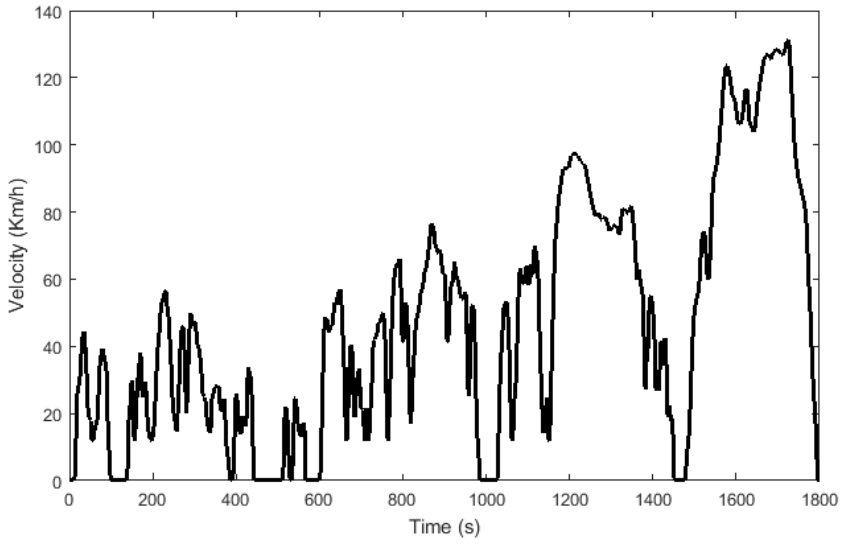

Figure 3.2 – WLTP Class 3 vehicle drive cycle

The WLTP Class 3 vehicle drive cycle covered 1800s in duration and was obtained from literatures [147]. It has been widely used in the automotive industry, as a replacement of the NEDC, acting as a standard drive cycle to measure emissions and fuel consumptions of light duty vehicles [148].

3.2.1 Fuel Cell Cycles Conversion

All real-world PEMFC operations can be and are required to be converted into time – load fuel cell cycles before applying the ATC development strategy. To convert the time – speed vehicle drive cycle into a fuel cell time – load cycle, a polarisation curve of a 25cm^2 single cell PEMFC generated from lab testing, as presented in Figure 3.3, was used to represent the relationship between load and voltage of a standardised PEMFC stack. The cell temperature was set at 65℃. The hydrogen and air were fully humidified before supplied to the cell, and the stoichiometry was 1.1 and 3.5 respectively.

The power demand of the drive cycle was calculated using equation (3.6) and equation (3.7).

$$P = F_{tr} * v \tag{3.6}$$

$$F_{tr} = \frac{1}{2}\rho * A * C_d * v^2 + m * g(A_d + B_d * v) \tag{3.7}$$

The meanings and selected values of the parameters are listed in Table 3-1 below. The values were selected not based on any specific vehicles but the average values of passenger vehicles.

Table 3-1 – List of variables of vehicle power calculation

Parameter	Selected Values	Unit
A: Frontal area	*2.5*	*m²*
C_d: Drag coefficient	*0.29*	
ρ: Air density	*1.2*	*kg/m³*
m: Vehicle mass	*1496*	*kg*
A_d: Tyre friction coefficient	*0.01*	
B_d: Velocity dependant tyre friction coefficient	*0.00005*	
g: Gravitational constant	*9.81*	*m/s²*
v: vehicle velocity	*Estimated from drive cycle*	*m/s*

The number of cells required to form the stack in order to meet the power demand of the drive cycles was calculated by dividing the maximum power demand of the drive cycle by the maximum power output of a single cell estimated from the polarisation curve. For the WLTP drive cycle, the maximum power demand was 27.5kW. Figure 3.3 also displays the power curve of the test cell, from which it can be observed that the maximum power output was 9W. Because the cells were connected in series to form the stack, the current remained unchanged while the voltage was the sum of the cell voltage, and power was the sum of the cell power. The calculated number of cells required to meet the maximum power demand of WLTP drive cycle was 3056, assuming all the energy generated was used to power the vehicle and no other losses during energy transmission. The number of cells utilised to form the stack was chosen as 3500 to ensure the stack being able to deal with unexpected high-power demand. The power demand of the WLTP was equally divided to each cell, and from Figure 3.3 it can be observed that the operating region of PEMFCs are within the ohmic region. This was before or at the points where PEMFCs reach their peak power. By selecting a power output point from the power curve, the corresponding current density can be identified, and with the help of the polarisation curve, the corresponding voltage output of the cell can be found. Therefore, by matching the power demand of the WLTP with the power output of the 3500-cells stack, required load and voltage can be found and the WLTP drive cycle was converted into fuel cell load profile. The converted load profiles of WLTP was shown in Figure 3.4.

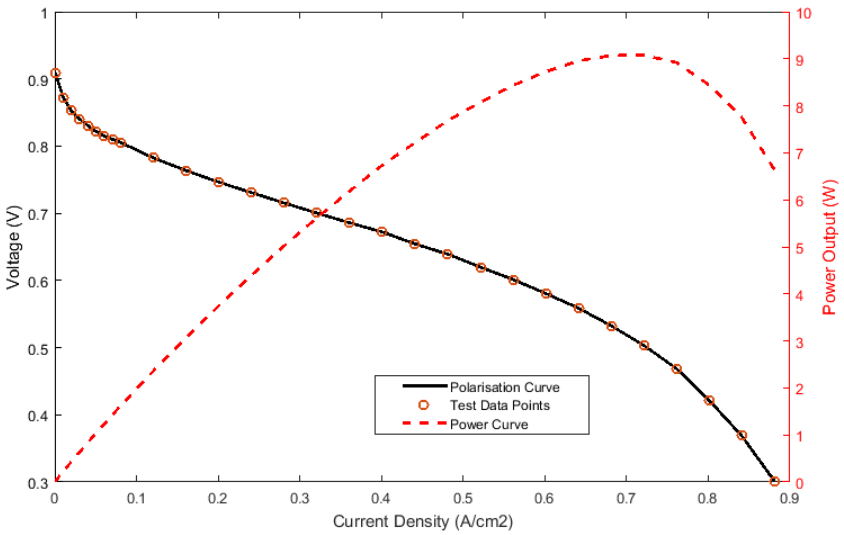

Figure 3.3 – Lab obtained polarisation curve and power curve

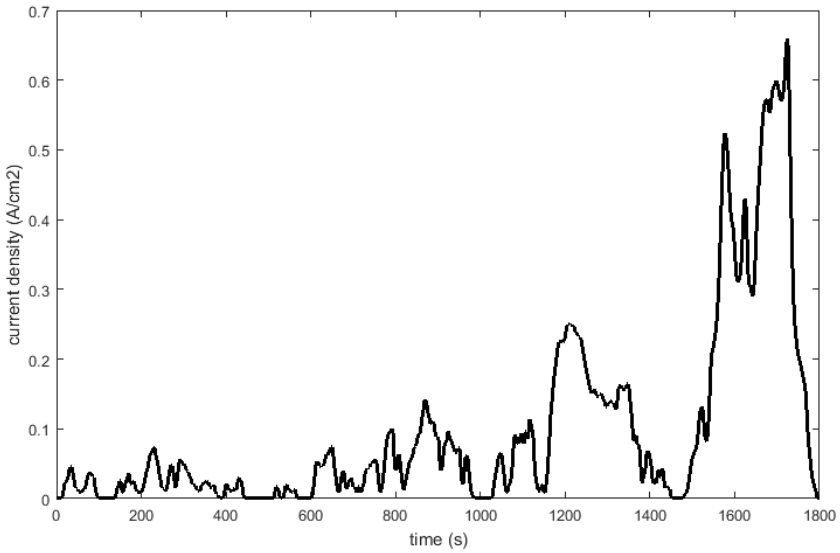

Figure 3.4 – WLTP PEMFC load profile

Although it is unusual in practice, pure fuel cells with no hybridisation are assumed in this research to power a vehicle, because this research only focuses on the degradation phenomenon of PEMFCs. Due to the limitations of resources, 25cm^2 PEMFCs are used in this research, which are much smaller than automotive PEMFCs. However, the purpose of this research is to demonstrate the possibility of condensing real-world operations into rapid test cycles to predict degradation, therefore, the size of the cell will not have significant effects. The design of connecting 3500 cells in series is also not ideal in real-world due to low reliability of the stack, but the design of the stack or the reliability are not the focus of this research and is not taken into considerations.

3.2.2 Degradation Simulation

After the real-world operations were converted into fuel cell load cycles, the WLTP load cycle was simulated using the PEMFC degradation model to calculate degradation voltage of each time step.

Repeated WLTP load cycle was simulated until the cumulative degradation voltage reaches 0.05V. Because the model calculates the degradation voltage loss caused by each time step, assuming the simulation covered T seconds before the EOL, the cumulative degradation voltage loss is the sum of the degradation voltage of all the completed time steps, as described in equation (3.8).

$$DV_{Total} = \sum_{n=1}^{T} DV(n) \tag{3.8}$$

Where DV_{Total} is the total degradation voltage at the EOL, and DV(n) is the degradation voltage loss at time step n.

Simulations of operating WLTP cycles until failure were completed 100 times. For each simulation, the time consumed before the total degradation voltage loss reached 0.05V was not all the same. If a time step was only contained in some of the simulations, the degradation voltage loss of that specific time step was set to 0, predicting a 'fail' before reaching that time step. The degradation voltages of a same time step of the 100 simulations were averaged out and the averaged value was regarded as the degradation voltage loss of the time step. The averaged degradation voltage loss of the time steps was then summed to calculate the total degradation voltage loss, when the value exceeded 0.05V, the stack was regarded as 'failed', and the durability of the stack can be determined.

The result showed that the durability of the cell was 1236 hours, and the simulated cumulative degradation voltage was shown in Figure 3.5 and the degradation voltage of one WLTP cycle was shown in Figure 3.6.

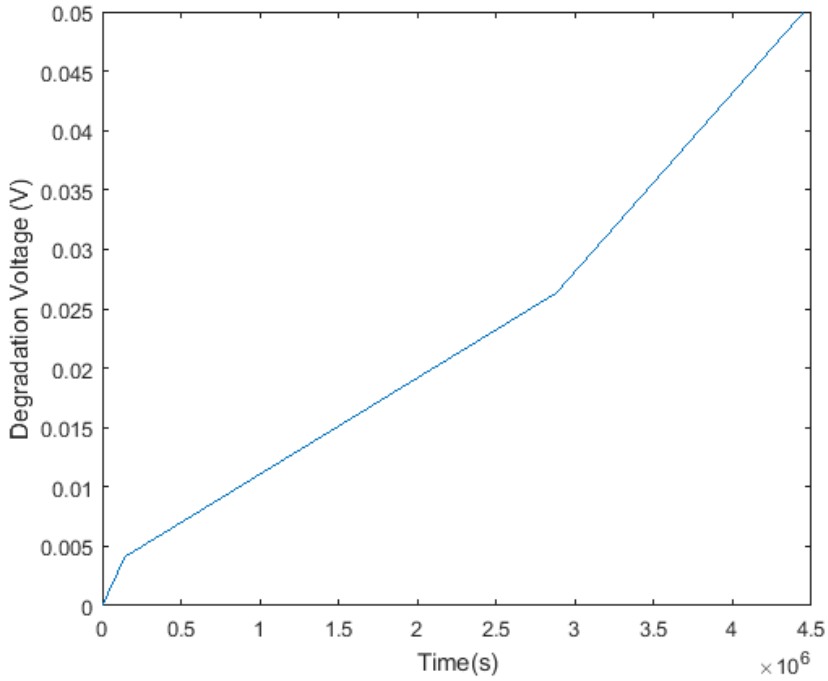

Figure 3.5 – Simulated cumulative WLTP degradation voltage

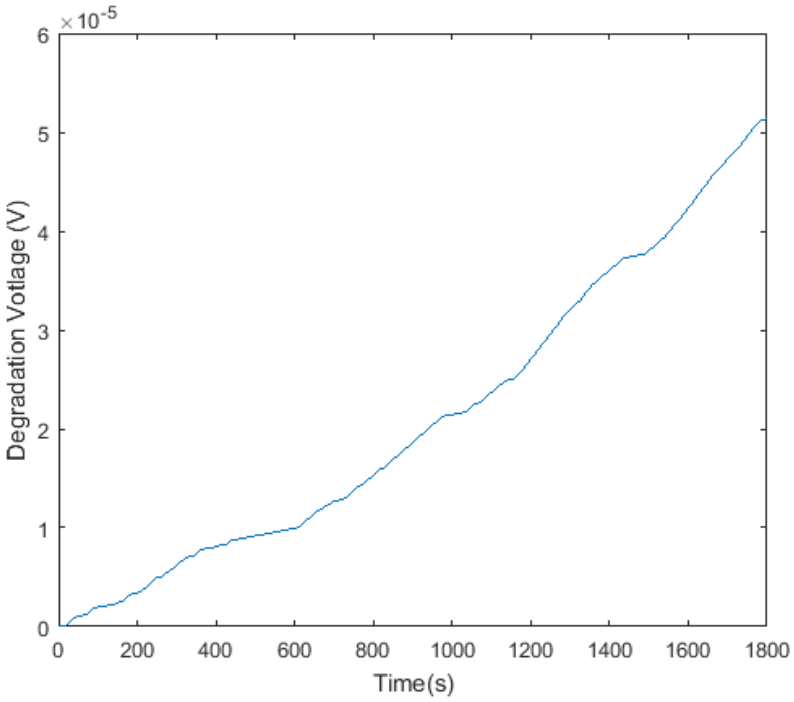

Figure 3.6- Simulated degradation voltage of one WLTP cycle

To evaluate the severity of the degradation of each time step and to decide which time steps can be eliminated, the degradation rate of a time step n was calculated as shown in equation (3.9) below.

$$DR_n = DV(n) - DV(n-1) \tag{3.9}$$

Where $\mathrm{DV(n-1)}$ and $DV(n)$ are degradation voltages of time step (n-1) and time step n separately, and DR_n is the degradation rate of time step n. The degradation voltage loss of time step 0 is regarded as 0 because it is assumed that no degradation has occurred in fresh cells.

Another method of obtaining the degradation rate of a time step n is to calculate the first order differential of the total degradation voltage loss, as shown in equation (3.10).

$$DR = \frac{d(DV)}{dt} \tag{3.10}$$

Where DR is the degradation rates and DV is the total degradation voltage loss.

Both methods can obtain the degradation rates of the simulated WLTP operation and the calculated degradation rates were presented in Figure 3.7

below. The average degradation rates throughout the simulation is calculated as 1.12 x 10^{-8} V/s

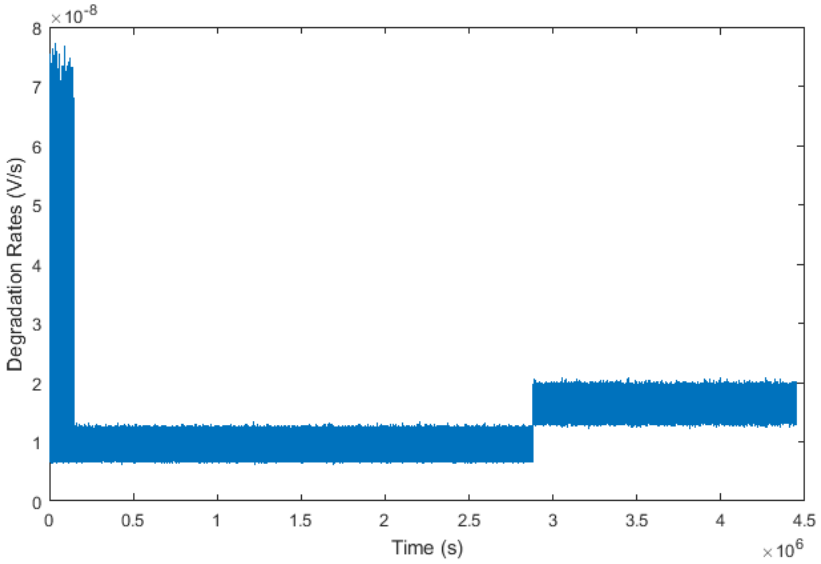

Figure 3.7 – Degradation rates of the WLTP operation simulation

From Figure 3.7 it can be observed that during different periods of the life of a PEMFC, the degradation rates varied within different ranges. The reason of the existence of the gap between 0 degradation rates and the lowest degradation rates value was because the model predicted degradation was happening throughout the entire simulation. The model predicts different degradation phenomenon during different stage of a PEMFC's life. During the initial period of life, from 0 to 40 hours, degradation rates were much higher than the rest of life due to the activation procedure of a fresh cell, and similar phenomenon has been reported by researchers. The average degradation rate of this period was 2.86 x 10^{-8} V/s, more than double the average degradation rates of the entire life. After the early stage degradation, the degradation rates were reduced and remained stable, calculated as 8.12 x 10^{-9} V/s. From approximately 800 hours to the end of life, degradation rates increased slightly, and the average degradation rates of the later stage of life was 1.53 x 10^{-8} V/s. This is because the carbon corrosion mechanism starts to be triggered.

3.2.3 Steps Selection

After the degradation rate of each time step was calculated, decisions of whether a time step would be selected to build the ATC were made according to the selection criteria. The selection criteria in this case was a degradation rate value, acting as a threshold. If the degradation rate of a time step was

higher than the selection criteria, the time step would be selected, otherwise removed.

The selection criteria can be varied according to different requirements of condensing the original load cycle. In this section, the average degradation rates of the entire simulated life of the PEMFC was utilised as the selection criterial, which was 1.12 x 10^{-8} V/s.

To have a clear illustration of how time steps were selected, Figure 3.8 presents the degradation rates (solid line) and selection criteria (dashed line) of the initial 1800s of the simulation. All the time steps that were above the average degradation rate line were selected to construct the ATC. Because the selection criteria is changeable, it can be expected that choosing higher selection criteria will result in less time steps being selected, and therefore, shorter and more condensed ATCs.

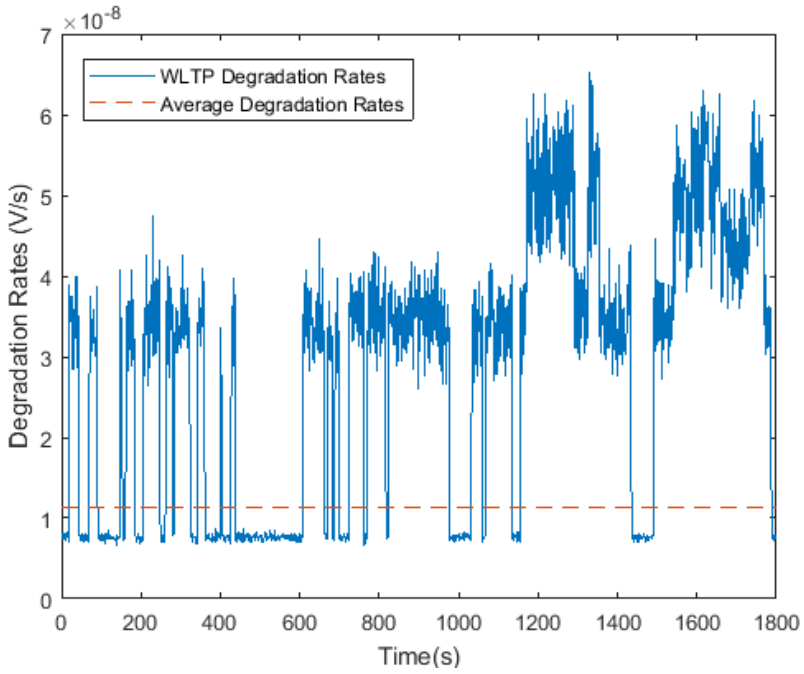

Figure 3.8 - Degradation rates of the initial 1800s of the WLTP simulation and selection criteria

3.2.4 ATC Construction and Acceleration Factor Calculation

After selecting the qualified time steps, the load information of the corresponding time step would be used to construct the ATC. The ATC was constructed by connecting the load output of the selected time steps in series. As a result, 1,775,220 (493h) out of 4,451,829 (1236h) time steps were selected to construct the ATC. It was not applicable to present all the data

clearly in a figure, and therefore, the initial 5000 seconds of the ATC and that of the WLTP were shown in Figure 3.9 for illustration. In comparison with the original WLTP load cycle it can be observed that the WLTP-based ATC reached peak load output 4 times in 5000s, while the original WLTP reached it only twice. The ATC was more intense in terms of load output compared with the original WLTP cycle, and the removed time steps were those that caused less degradation voltage loss according to the model calculation.

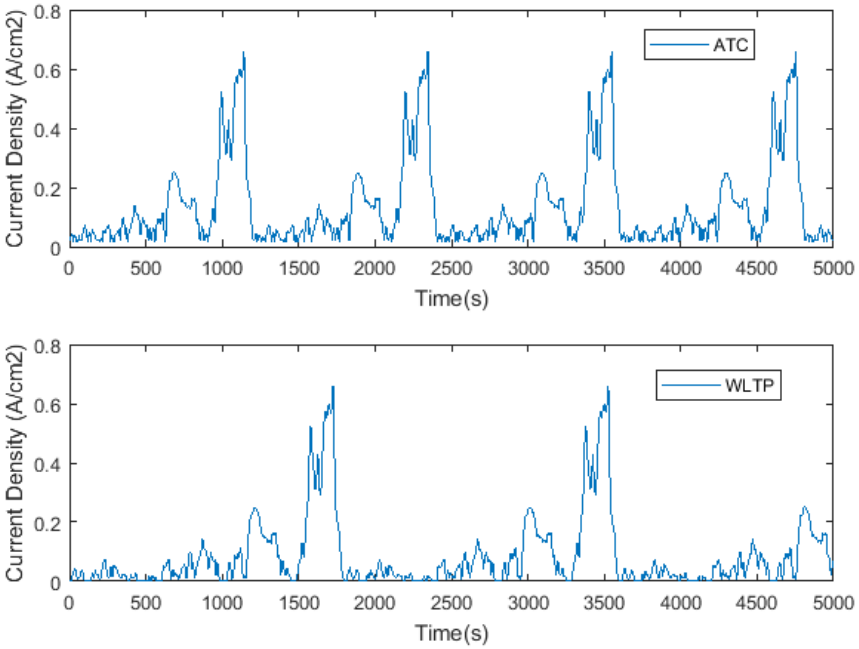

Figure 3.9 - WLTP-based ATC compare with WLTP operation load cycle

The degradation voltage remaining in the developed ATC was calculated as presented in equation (3.11).

$$DV_{ATC} = \int DR_{Selected} \tag{3.11}$$

The degradation voltage remaining in the ATC was 0.0287V over 493 hours.

The acceleration factor that represented the ratio between the degradation voltage remained in the developed ATC and that of the original WLTP operation was calculated as shown in equation (3.12).

$$AF = \frac{DV_{WLTP}}{DV_{ATC}} = \frac{0.05V}{0.0287V} = 1.74 \tag{3.12}$$

Where DV_{ATC} is the degradation voltage remained the ATC, and DV_{WLTP} is the simulated WLTP total degradation voltage.

3.2.5 Degradation Voltage Prediction and Error Analysis

The acceleration factor was defined as the ratio between the total degradation voltage of the WLTP and that remaining in the developed ATC. The degradation voltage of the WLTP operation can be predicted by multiplying the degradation voltage caused the ATC by the acceleration factor, as shown in Equation (3.13).

$$DV_{WLTP-Predicted} = DV_{ATC} \times AF \tag{3.13}$$

The ATC was used as input of the PEMFC degradation model and degradation voltage was obtained. Similar to simulations in section 4.2.2, to ensure the accuracy of the model assessment, the simulation was repeated 100 times and the degradation voltage loss used was the average value. The simulation of the ATC calculated that the voltage would be degraded by 0.0311V after 493h of ATC operation, and the average degradation rate was 1.75 x 10^{-8} V/s, over 56% higher than that of the original WLTP operation, which was 1.12 x 10^{-8} V/s. Table 3-2 presented the detailed information of the ATC degradation voltage simulation and WLTP operation degradation voltage prediction. The error was calculated as shown in equation (3.14).

$$\partial = \left(\frac{DV_{WLTP-Predicted}}{DV_{WLTP-Simulated}} - 1\right) \times 100\% \tag{3.14}$$

Where $DV_{WLTP-Predicted}$ is the predicted WLTP operation degradation based on ATC simulation and the acceleration factor, and $DV_{WLTP-Simulated}$ is the simulated WLTP operation degradation voltage, which is 0.05V in this case.

Table 3-2 – WLTP-Based ATC Degradation Voltage Prediction

Simulated ATC Degradation Voltage	Acceleration Factor	Predicted WLTP Degradation Voltage	Simulated WLTP Degradation Voltage	Error
0.0311 V	1.74	0.0541 V	0.05 V	8.2%

From Table 3-2 it can be concluded that by selecting time steps with higher than average degradation rates, the WLTP cycle was condensed into a shorter ATC. Although the total degradation voltage loss of the ATC was less than that of the WLTP due to the removal of time steps, the degradation rates of the ATC was almost doubled compared to that of the WLTP operation. The ATC was only approximately 40% of the WLTP in duration (493 hours out of 1236 hours), and about 57% degradation voltage remaining in the ATC. The

removed degradation voltage was represented by the acceleration factor and could be used to predict the degradation voltage of the WLTP operation based on the degradation voltage of the ATC and the error was 8.2%. The error is believed to be caused by the Weibull distribution used in the model to represent the uncertainties of real-world testing and the variation of degradation rates of a same degradation mechanism during different stages of life. It is also caused by the differences in degradation rates during different period of PEMFC life.

3.3 ATC Validation

Experiments were performed to validate the model-based accelerated test cycle development method. Due to the time and budget constraints, ATC was developed based on 400 WLTP cycles simulations at 60°C results prior to experiments. The simulation was run 100 times and the degradation voltage loss of each time step utilised to calculate the degradation rates was the average value of the 100 simulations. The selection criteria chosen was the average degradation rate, 1.22 x 10^{-8} V/s, and all of the time steps with higher degradation rates were selected. Figure 3.10 below presented the simulated degradation rates of the 400 WLTP cycles. The average degradation rate was 3.88 x 10^{-8} V/s, which is more than 3 times higher than that of the 400 WLTP cycles.

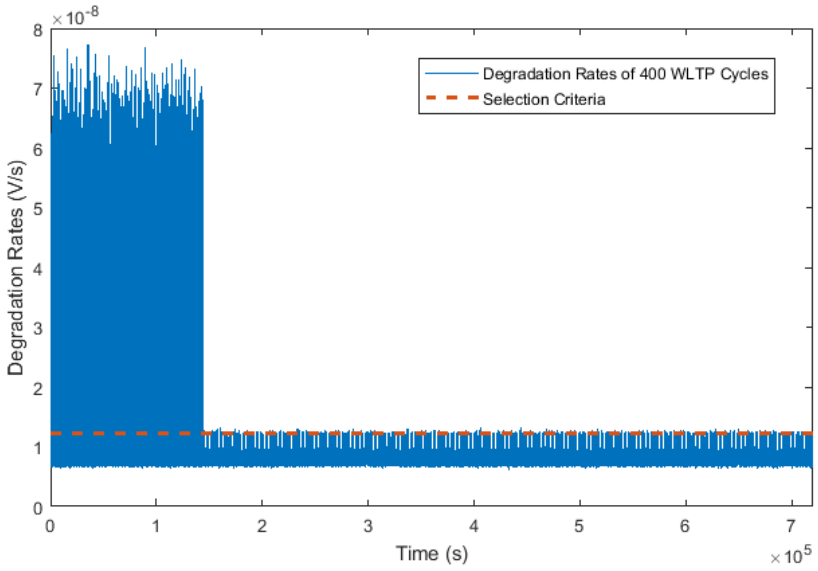

Figure 3.10 – Simulated degradation rates of 400 WLTP cycles and selection criteria

The acceleration factor between the 400 WLTP operation and the ATC was calculated as 2.33, and the original 200 hours testing time was condensed into 27 hours. The developed 400-WLTP based ATC was presented in Figure 3.11

below and was utilised for experimental validation of the ATC develop strategy.

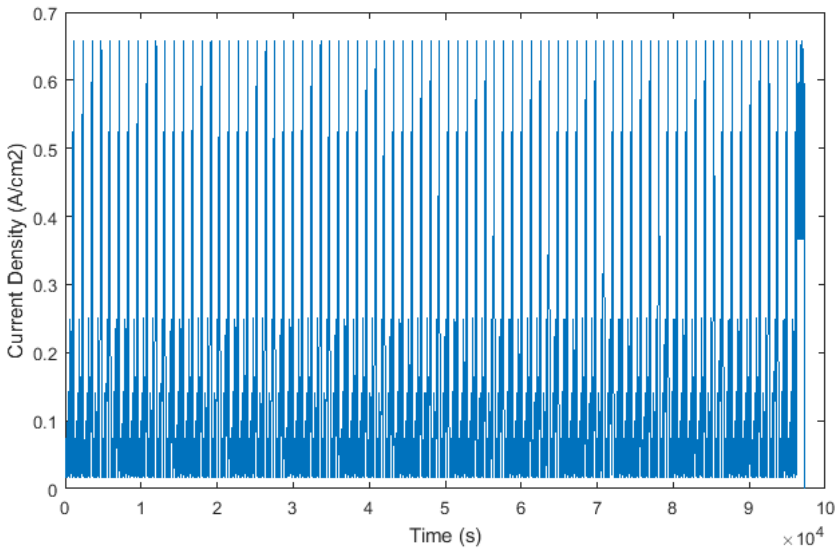

Figure 3.11 – 400 WLTP based accelerated test cycle

A 25cm^2 test cell was used to perform the experiments by running 400 WLTP operations and the developed 400-WLTP-based ATC operation. Polarisation curves were generated before and after tests to quantify the degradation voltage loss caused by the WLTP operation and the ATC operation.

3.3.1 Experimental Set Up and Testing Equipment

A sketch of the experimental setup is shown in Figure 3.12

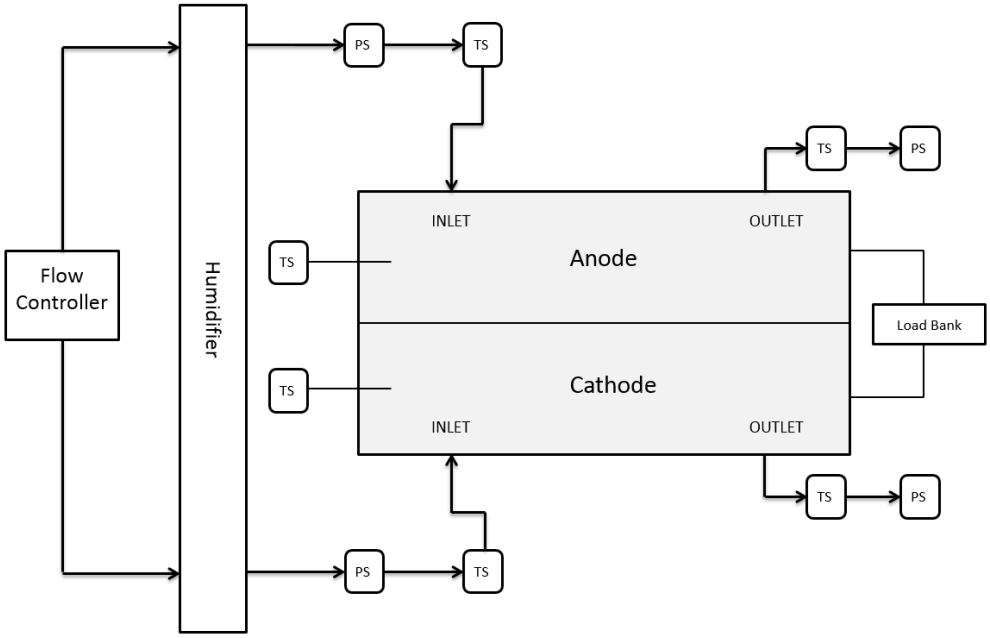

Figure 3.12- Experimental Setup

The inlet gases were heated and humidified before being supplied to the cell.

99.999% pure H_2 stored in bottles at 350 bar was used at the anode and air was used as cathode feed gas. The mass flow controller used to control the reactant gases flow is shown in Figure 3.13, and hydrogen and air flow rates were set to 0.22L/min and 0.81L/min respectively, based on the calculation of maximum load output and a hydrogen and air stoichiometry of 1.1 and 3.5 respectively.

Due to the limitation of the lab equipment, the relative humidity of the inlet and outlet gases could not be measured precisely but the both inlets were fully humidified by a humidifier at 75°C. The humidifier utilised was a manual gas humidifier system with autofill, manufactured by Fuel Cell Technologies Inc. as shown in Figure 3.14. The humidifier pumped the inlet gases through a water bottle, the temperature of which is controlled, and then supplied to the inlets of the cell through gas pipes. The temperature of the bottle and the pipes were set to 75°C and 85°C to minimise heat loss.

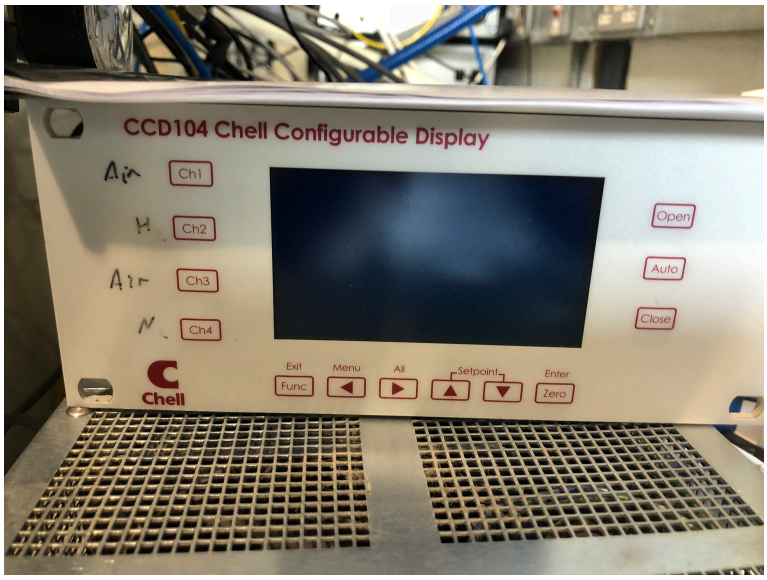

Figure 3.13 – Mass flow controller

Figure 3.14 – Humidifier used

At each inlet and outlet of the cell, the temperature and pressure of the gas was measured by sensors (represented by PS and TS in Figure 3.12), and the data was recorded. The cell temperature was measured by a K-type thermocouples and was controlled and maintained by the fuel cell heater and temperature controller that is shown in Figure 3.15. If the measured

temperature was below the pre-set value, the heater started to heat up the cell. Pressure at inlets and outlets of the two electrodes were measured using PXM-219 pressure sensors and data acquired from sensors were collected using a National Instrument compact DAQ data logger. Cell temperature was set to 60°C and the pressure remained ambient during the experiments.

Figure 3.15 – Fuel cell heater and temperature controller

The Load bank used to draw and control current output from the cell was a TDI power system load bank, as presented in Figure 3.16, with a load and power range from 0-150A and 0-800W respectively.

Figure 3.16 – TDI power system load bank

The electrolyte membrane used in the test cell was a commercially available Nafion 211 membrane with an active area of 25cm^2 (5cm×5cm). Pure Pt was used as catalyst for both electrodes, and the catalyst loading was 0.3mg/cm^2 at both sides. Carbon cloth GDLs were used and single serpentine flow fields were on the graphite plates. GDEs were hot pressed into the membrane. Graphite bipolar plates and gold-coated current collector plates were used, and the sealing gaskets were made of silicone. Torque on assembly was set to 10 Nm. The assembled cell was presented in Figure 3.17.

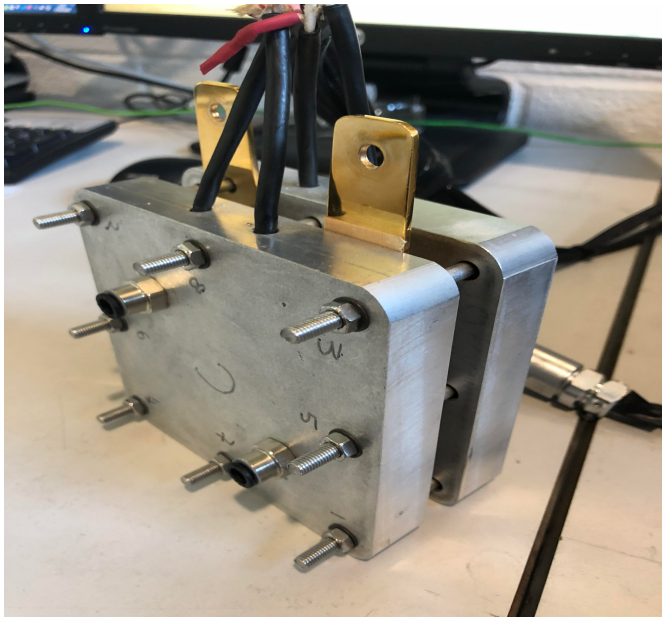

Figure 3.17 – The assembled 25 cm^2 Nafion 211 test cell with 0.3mg/cm^2 catalyst loading

3.3.2 Testing Procedure

An activation procedure was done before starting the actual tests for the first time. The cell was held at 0.6V for 1 hour, and 10 WLTP cycles were run over 5 hours to active the cell. The cell was then purged using dry N_2 and followed by 30mins steady operation at 0.6V. The purpose of purging and steady state operation is to remove any reversible degradation voltage loss caused by the previous tests and ensure the polarisation curves produced later could reflect the cell performance at a relatively stabilised operational condition.

After the activation procedure, two back-to-back polarisation curves were generated, representing the performance of the fresh test cell. After recording the polarisation curves, the cell ran WLTP cycles continuously for 24 hours, regarded as a test block. The cell was again purged with dry N_2 for 30mins and stabilised at 0.6V for 30mins after each test block, then polarisation

curves were recorded to assess the performance and degradation of the cell. The cell completed 400 WLTP cycles in total.

The testing procedure of the ATC cycle is similar to that of the WLTP cycle. Activation procedure was performed to measure the performance at the start of the ATC tests. WLTP-based ATC was run for 5 hours and polarisation curves were recorded after the purging and stabilising procedure described above. The results were used to represent the performance at the beginning of the ATC tests. The ATC testing consisted of several testing blocks, 24 hour each. After each test block, the same purging and stabilising procedure followed to ensure the consistence of the tests. Polarisation curves were recorded after the purging and stabilising procedure.

3.3.3 Validation of The Models

Prior to validating the ATC development strategy through experiments, Model 1 and Model 2 were firstly validated by comparing the simulated degradation voltage losses with the tested ones. Error was obtained as shown in equation (3.15)by dividing the model predicted degradation voltage losses by the tested ones and subtracting 1. This is to evaluate the accuracy of the model after being modified and utilised in this research.

$$\delta = \frac{DV_{model}}{DV_{Tested}} - 1 \tag{3.15}$$

The models were validated using 400 cycles of WLTP. Tests repeated 3 times. To obtain representative voltage decay, three polarisation curves were obtained at every 50 hours, equivalent to 100 WLTP cycles, and the three voltages at a same current density were averaged and utilised to represent the voltage at the current density. The polarisation curve results obtained at fresh cell, and that after running WLTP operation for 50 hours, 100 hours, 150 hours, and 200 hours are shown in Figure 3.18.

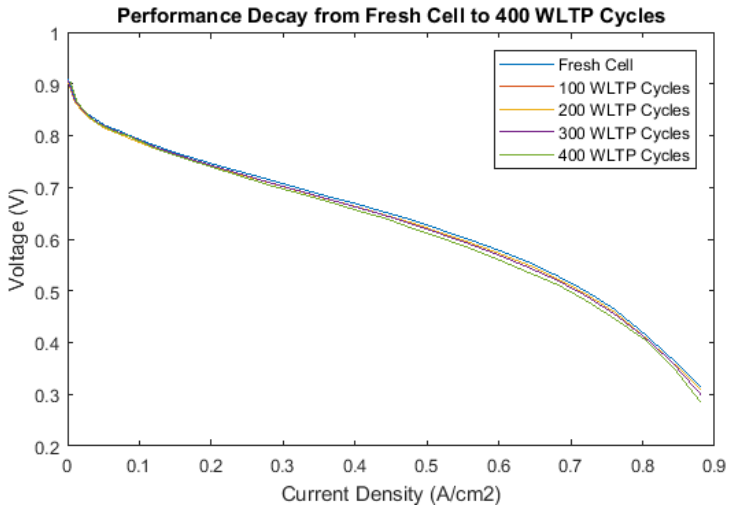

Figure 3.18 – Tested Performance Decay of WLTP Cycles

Electrochemical impedance spectroscopy was applied before and after the 400 WLTP cycles tests to observe the degradation phenomenon in the cell and measure resistance in the cell at 0.25A/cm^2, 0.5A/cm^2 and 0.75A/cm^2. Galvanostatic EIS sweeps were applied from 500Hz to 0.1Hz with an amplitude of 20mV. Results are presented in Figure 3.19 and Figure 3.20.

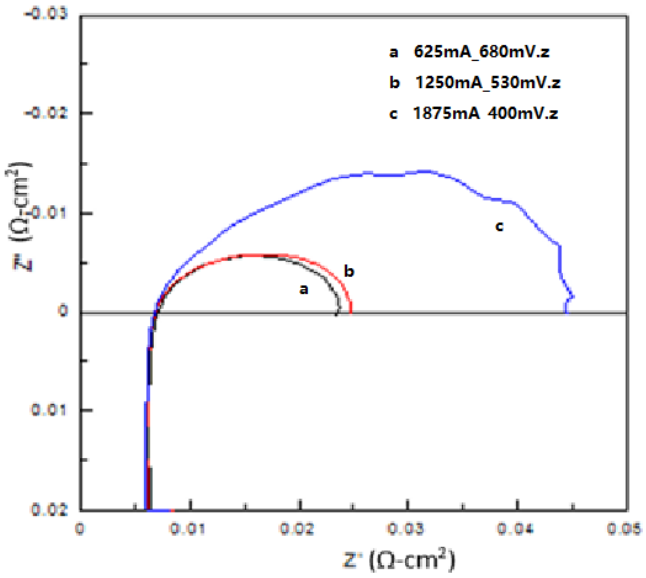

Figure 3.19 – Electrochemical impedance spectroscopy before tests at different current densities

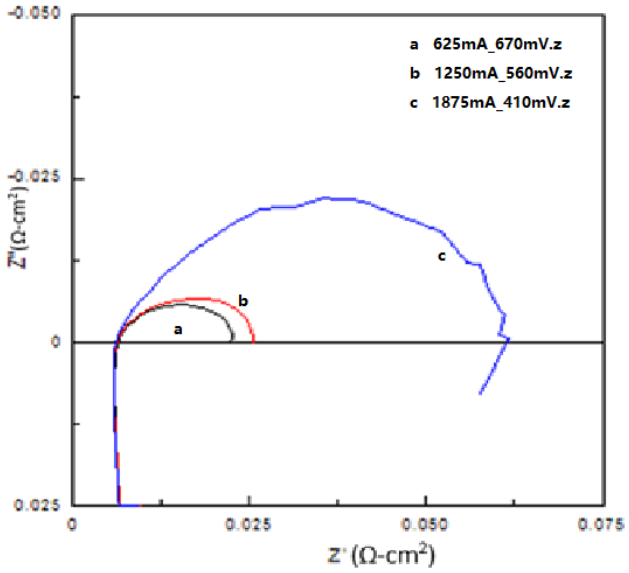

Figure 3.20 – Electrochemical impedance spectroscopy after tests at different current densities

The area between the two X-axis (y=0) intersects of a curve indicate the activation losses of the two electrodes and the mass transfer losses. Ideally, the EIS results consist of two arcs as represented in Figure 1.4. The small and the large curves represent the anode and cathode activation loss respectively. However, in reality it is very common that EIS only produces one large arc, representing the combined anode and cathode activation and mass transport losses. Therefore, by comparing the area of the curves generated under the same cell condition at different current densities it can be observed that the combined activation and mass transport losses increased with the increasing current density. Comparing the area of the curves generated at the same current density before and after tests it can be found that the after 200 hours of WLTP operation, the combined activation losses and mass transport losses were increased also.

The overall cell resistance is represented by the curve intersecting the x axis at around 0.006(Ω-cm^2) and indicate Ohmic losses. By comparing the EIS curves under the same cell condition at different current densities it can be observed that the overall resistance of the cell slightly increased with the increasing current densities.

To quantify the degradation voltage loss from polarisation curves, the voltage differences between the data points of two polarisation curves at the same current densities were averaged out. The degradation voltage loss of the three tests were averaged and regarded as the actual degradation voltage loss. The results were compared with the model calculations and were shown in Table 3-3.

Table 3-3 – 0-400 WLTP Cycles Modelling and Tested Results Comparison

Testing Duration	Tested Degradation Voltage	Model 1 Prediction	Model 1 Error	Model 2 Prediction	Model 2 Error
0-100 WLTP	0.0036 V	0.0046 V	26.92%	0.0045 V	23.66%
0-200 WLTP	0.0054 V	0.0063 V	16.67%	0.0068 V	20.63%
0-300 WLTP	0.0081 V	0.0093 V	14.81%	0.0096 V	18.69%
0-400 WLTP	0.0106 V	0.0118 V	11.32%	0.0124 V	16.87%

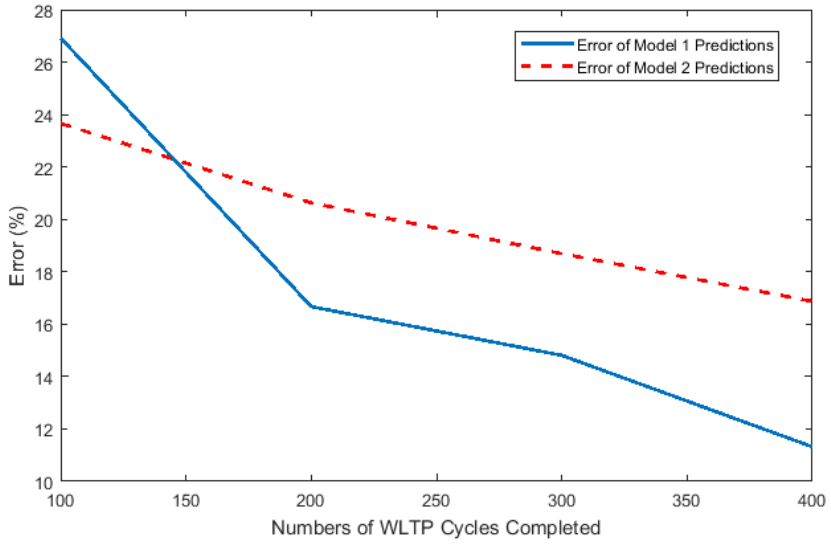

Figure 3.21 – Error curves of Model 1 and 2 of predicting the degradation voltage loss of 0-400 WLTP cycles

The error of the two models is presented in Figure 3.21, and the comparison between Model 1 and Model 2 with the experimental results proved that for short term degradation voltage prediction, Model 2 was more accurate than Model 1. This is because in Model 2, the immature catalyst agglomeration mechanism, which lead to degradation voltage loss prediction with a high degradation rate was removed and was merged with mature catalyst agglomeration to form a catalyst agglomeration mechanism. The over-prediction from Model 1 was reduced due to the combination of the catalyst agglomeration mechanisms. However, in terms of long-term degradation

voltage loss prediction, the prediction made from Model 2 was less accurate than that made from Model 1. Although both models could be used to predict the overall degradation voltage loss of PEMFC operations, this research focusing on long-term operations, and as such Model 1 is believed to be more accurate than Model 2 in terms of predicting degradation voltage loss.

3.3.4 Results and Error Analysis

To predict the degradation voltage loss of the 400 WLTP operation based on tested ATC results and calculate the error, the polarisation curves before and after each 400 WLTP operation were obtained. Figure 3.22 below presents the polarisation curves before and after 400 WLTP cycles of one test. The average voltage difference between the two curves at a same current density was regarded as the degradation voltage loss of one test. Three sets of polarisation curves were obtained for the three repeated tests. The degradation voltage loss of 400 WLTP cycles obtained from the three repeated tests were then averaged out to represent the actual degradation voltage loss caused by the operation.

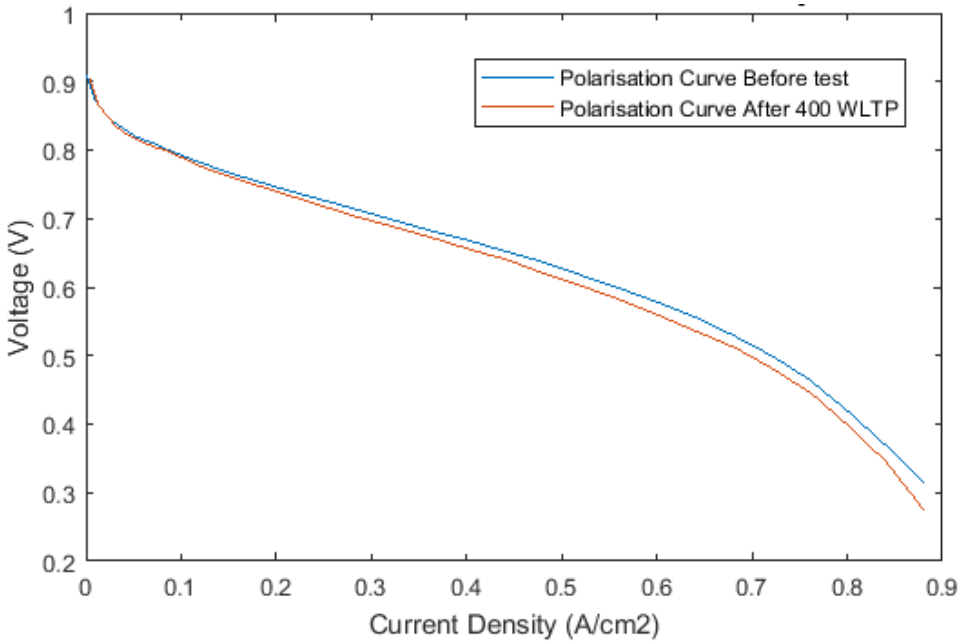

Figure 3.22 – One Set of the Polarisation Curves Obtained before and after 400 WLTP Cycles Test

The same analysis method was applied to the ATC experiment to quantify and evaluate the degradation voltage caused by the ATC. The ATC was tested three times, and the degradation voltage loss of the three testes were averaged out and regarded as the degradation voltage loss caused by the ATC. Table 3-4 contains the experimental results of the ATC and the prediction of the degradation voltage of the 400 WLTP operation is calculated by multiplying the tested degradation voltage loss of the ATC by its acceleration factor. The

predicted 400 WLTP operation degradation voltage was compared with experimental data to calculated error.

Table 3-4 – Prediction of Degradation Voltage of the 400 WLTP Operation Using tested ATC Results

ATC	experimental ATC Degradation Voltage	Acceleration Factor	Predicted WLTP Degradation Voltage	Experimental WLTP Degradation Voltage	Error
ATCW	0.0053 V	2.33	0.0123 V	0.0106	16%

From Table 3-4 it can be concluded that by using the developed 400-WLTP-based ATC, the degradation voltage loss of the 400 WLTP operation was successfully predicted. This was done by multiplying the tested degradation voltage loss of the 400-WLTP-based ATC by the acceleration factor. The error of the prediction was 16%. The prediction made using the experimental results proved that it was applicable to condense a real-world operation into a short test cycle to reduce durability testing time and ensure accuracy simultaneously. The testing time of 400 WLTP operation was reduced by 86.5%, from 200 hours to 27 hours, with a degradation voltage prediction accuracy of 84%.

3.4 Conclusions

In this chapter, the procedure of condensing WLTP PEMFC operation into an accelerated test cycle was described in detail. The degradation voltage loss of the WLTP operation was successfully predicted using the developed accelerated test cycle through model simulation with an accuracy of 92%. The accuracy of calculating the degradation voltage loss of PEMFCs using the PEMFC model combined with the petri nets degradation model was examined and proved through experimental validation. The model used in this work was validated using the degradation voltage loss of 400 WLTP cycles obtained from experiments conducted by the author. The error of using Model 1 and Model 2 to predict the degradation voltage loss of the 400 WLTP cycles was 11% and 17% respectively. Diagnostic tools such as polarisation curves and EIS were used to analyse the data and the degradation voltage loss of 400 WLTP cycles operation was successfully predicted using the tested ATC degradation voltage and the acceleration factor, and the error was 16%. The aim of reducing testing time and predict durability accurately has been achieved.

Chapter 4

4 ATC Sensitivity Analysis

4.1 Introduction

A model-based accelerated test cycle development strategy utilised a PEMFC degradation model to calculate the degradation voltage and rate of each time step of targeted real-world operations. Based on the modelling results, decisions on whether to keep or remove individual time steps to construct the ATC were made according to the chosen selection criteria. Three key factors were identified; the transit nature of the PEMFC load profile, the selection criteria that dominated the time step selection, and the PEMFC degradation model used.

In this chapter, the effects of the three factors on the accuracy of utilising the model-based ATC development strategy to predict the durability of a PEMFC will be analysed and the universality of the strategy is discussed.

4.2 ATC Evaluation against Different Real-World Operations

To analyse the sensitivity of the strategy to different real-world operations, NEDC and JC08 were selected as other representatives of real-world operations to compare with WLTP cycle. The maximum power demand of NEDC and JC08 cycles were calculated using equation (3.6) and (3.7), and the maximum power output of NEDC and JC08 were 22.3kW and 8.65kW, respectively. The maximum power demands were below the maximum power output of the 3500 of 5×5cm^2 cells PEMFC stack, and the 3500-cells stack utilised in Chapter 3.2.1 was also used here to calculate the power demand of each cell. As discussed in Chapter 3.2.1, NEDC and JC08 were converted into fuel cell load cycles by matching the power output of the two drive cycles with the power output of a standardised 3500-cells PEMFC stack. The converted NEDC and JC08 load profiles were presented in Figure 4.1 below, and the corresponding voltage profile of the NEDC and JC08 PEMFC load profiles are contained in Figure 4.2 and Figure 4.3 separately.

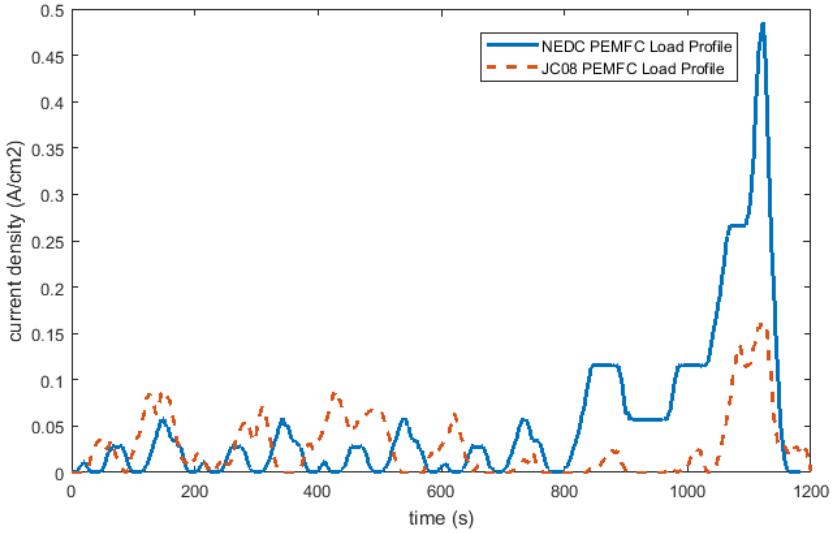

Figure 4.1 – NEDC and JC08 load profiles

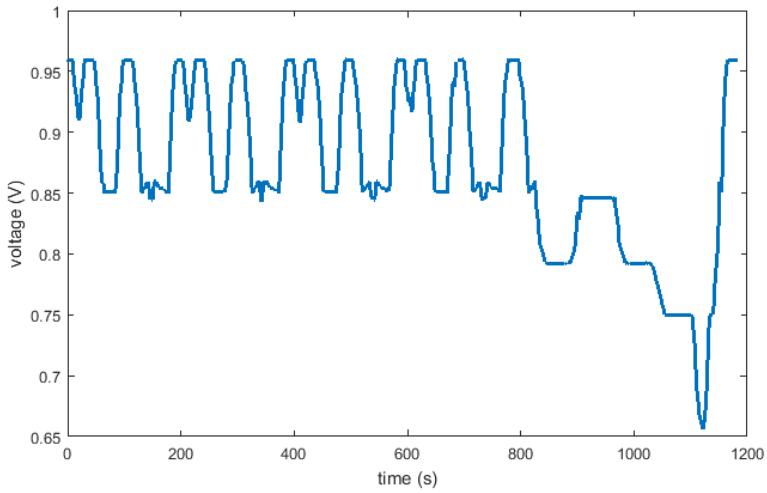

Figure 4.2 – Voltage profile of PEMFC NEFC cycle

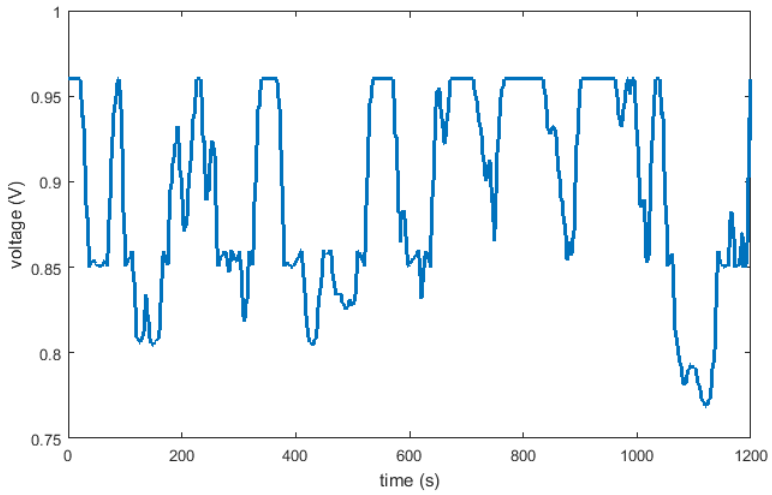

Figure 4.3 – Voltage profile of PEMFC JC08 cycle

The NEDC and JC08 load cycles were used as inputs of the fuel cell degradation model and simulations were run until the cumulative degradation voltage reached 0.05V. Simulations were run three times and the average degradation voltage of each time step was used as the degradation voltage and degradation rates were obtained using equation (3.9) and (3.10).

The simulation completed 3866 NEDC cycles, equivalent to 1270 hours of lifetime, and 3880 JC08 Cycles, equivalent to 1293 hours before failure. The degradation voltage of NEDC and JC08 are presented in Figure 4.4 and Figure 4.5 respectively.

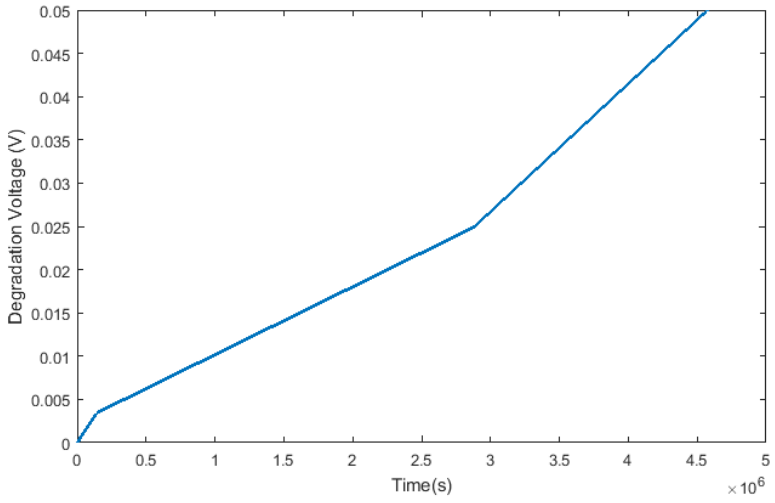

Figure 4.4 – Simulated NEDC cumulative degradation voltage

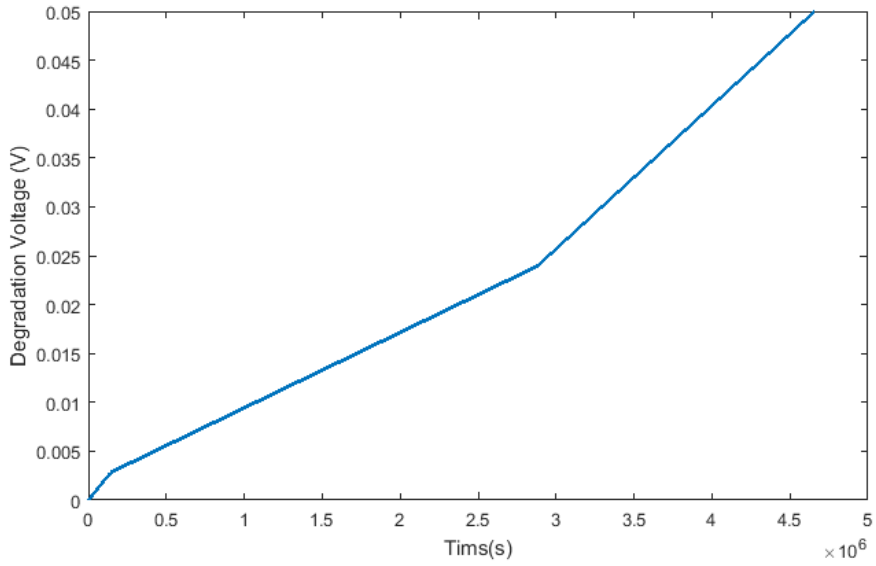

Figure 4.5 – Simulated JC08 cumulative degradation voltage

By comparing the simulated degradation voltage of the WLTP, NEDC and JC08 operations it can be observed that the overall degradation voltage of the three operations followed a similar trend. Although the shape of the simulated degradation voltage loss of the three operations looks similar, if detailed degradation voltage loss accumulation within a short time frame is looked at, it varies from the three operations. The degradation voltage loss is dependent of the load output. The degradation rate was relatively high at the start of life, reduced after 40 hours of operation and finally increased again towards the end of life. The phenomenon was because the Petri Nets model predicted that the degradation rate caused by immature catalyst agglomeration in the initial 40 hours of life was much higher than that of the matured catalyst agglomeration after 40 hours operation. At the end of life, the GDL started to degrade and material ions were released into the MEA resulting in a more severe degradation phenomenon. Those trends have been reported by researchers and adopted in the Petri Nets degradation model [92].

The degradation rates of the NEDC and JC08 simulations are presented in Figure 4.6 and Figure 4.7. The average degradation rates of the simulation of repeated NEDC and JC08 were 1.093 x 10^{-8} V/s, and 1.073 x 10^{-8} V/s, respectively. As mentioned in Chapter 3.2.2, the average degradation rate of the WLTP was 1.12 x 10^{-8} V/s. The three cycles, listed in order of decreasing average degradation rate is this: WLTP, NEDC, JC08.

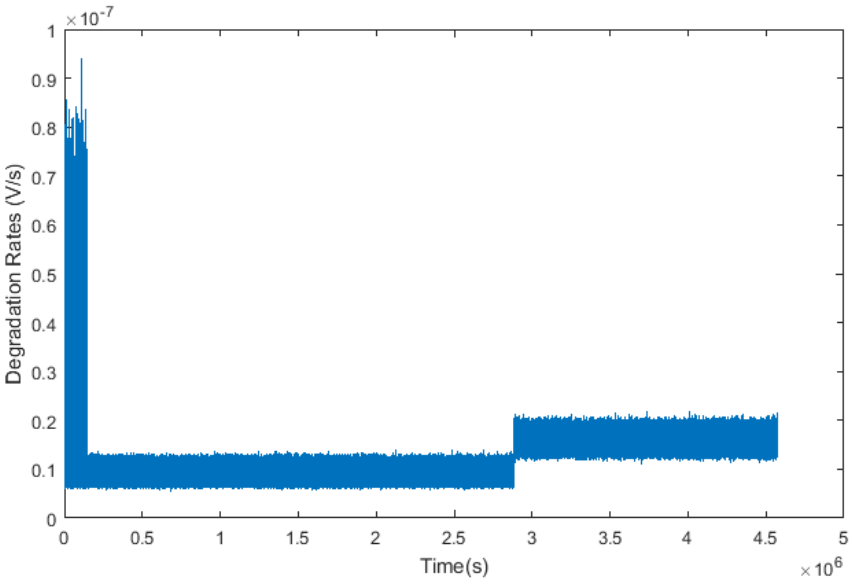

Figure 4.6 – Degradation rates of the NEDC operation simulation

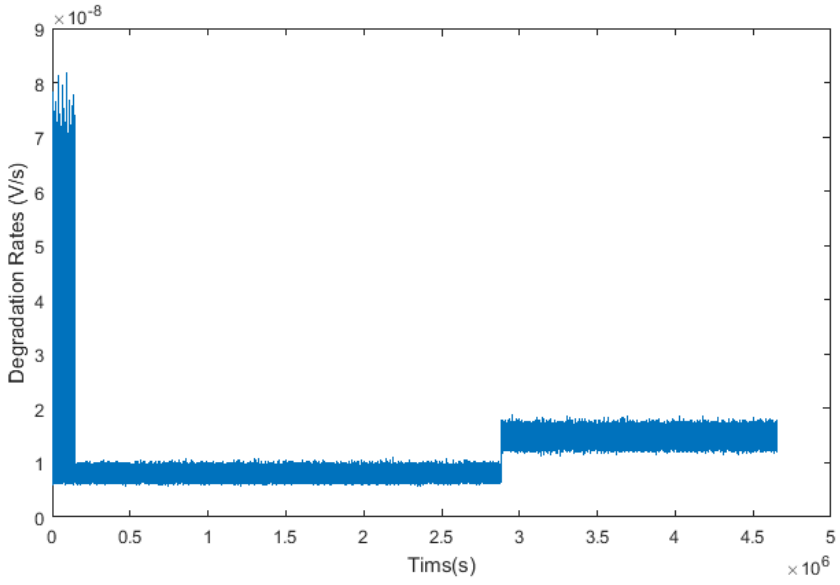

Figure 4.7 – Degradation rates of the JC08 operation simulation

To develop the ATC for NEDC and JC08 simulations, the selection criteria applied in this section were the same as that used for the WLTP simulation, which used the corresponding average degradation rates. The degradation rates of the initial 1200s of the NEDC and JC08 simulations are presented as solid lines in Figure 4.8 and Figure 4.9 respectively. The dashed line in Figure

4.8 and Figure 4.9 represent the average degradation rates of NEDC and JC08 simulations and all the time steps the degradation rates of which were above those lines were selected to construct the NEDC-based ATC and JC08-based ATC.

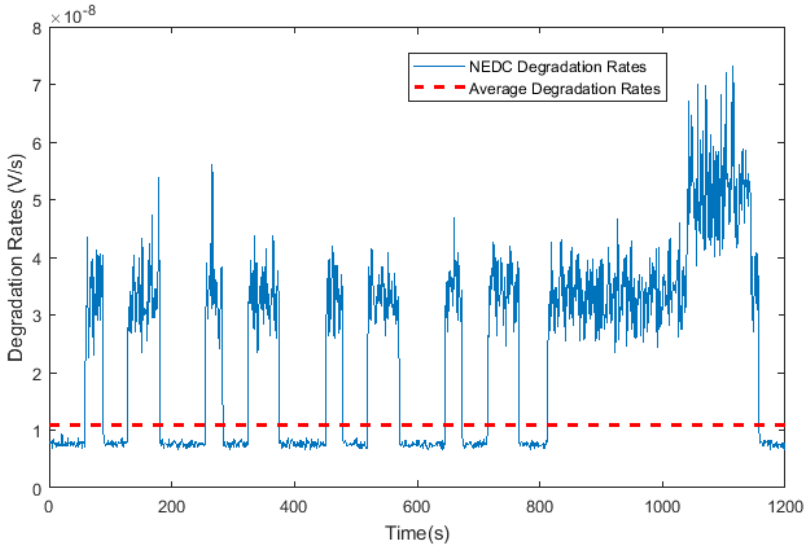

Figure 4.8 – Degradation rates of the initial 1800s of the NEDC simulation and selection criteria

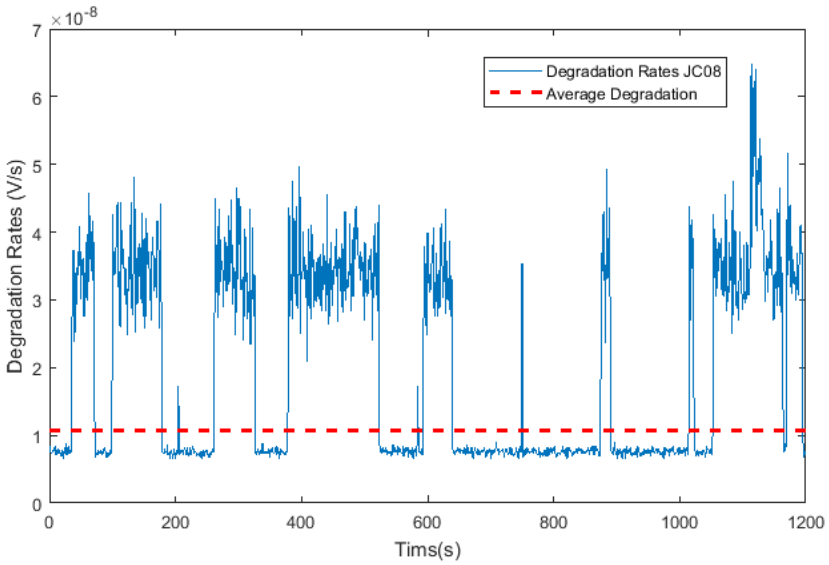

Figure 4.9 – Degradation rates of the initial 1800s of the JC08 simulation and selection criteria

The degradation voltage remaining in the developed ATCs were firstly calculated using equation (3.11) in Chapter 3.2.4, and the acceleration factors

of the NEDC-based and JC08-based ATCs were obtained using equation (3.12).

$$DV_{NEDC-Bassed\ ATC} = \int DR_{Selected} = 0.0286\ V \quad (3.11)$$

$$DV_{JC08-Bassed\ ATC} = \int DR_{Selected} = 0.0282\ V \quad (3.11)$$

$$AF_{NEDC-Based} = \frac{DV_{NEDC}}{DV_{NEDC-Based\ ATC}} = \frac{0.05V}{0.0286V} = 1.75 \quad (3.12)$$

$$AF_{JC08-Based} = \frac{DV_{JC08}}{DV_{JC08-Based\ ATC}} = \frac{0.05V}{0.0282V} = 1.77 \quad (3.12)$$

After the time steps were selected, the load information of the selected time steps was used to construct the ATCs by connecting the load output of the selected time steps in series. The NEDC-based and JC08-based ATCs were developed and a comparison between the initial 5000s of each ATC can be seen in Figure 4.10 and Figure 4.11.

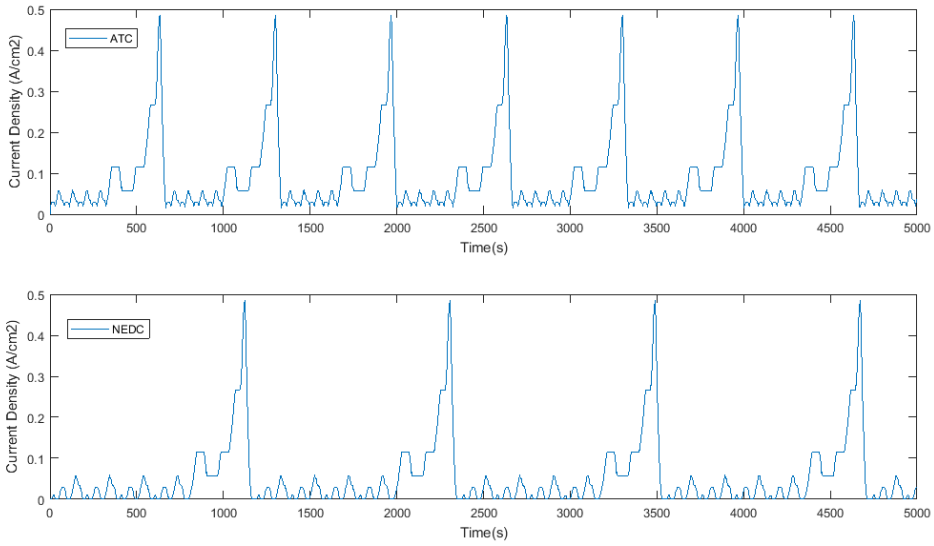

Figure 4.10 – Initial 5000s NEDC-based ATC Compare with NEDC

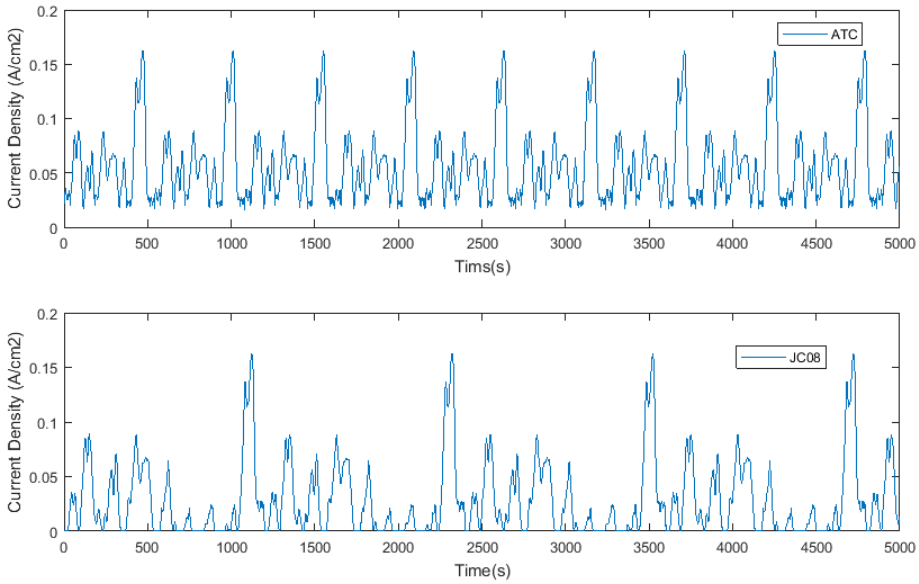

Figure 4.11 – JC08-based ATC Compare with JC08

From Figure 4.10 and Figure 4.11 it can be observed that the NEDC-based ATC reached peak load output 7 times in 5000s, while the original NEDC reached peak load only 4 times. The JC08-based ATC reached peak load output 9 times in the initial 5000s, while the original JC08 reached peak load only 4 times.

The developed NEDC-based ATC and JC08-based ATCs were simulated using the model and degradation voltages of NEDC and JC08 were predicted based on the corresponding simulation results and their acceleration factors. Each ATC simulation was repeated 100 times and the total degradation voltage loss was calculated by averaging the total degradation voltage loss of the 100 simulations. The total degradation voltage loss of NEDC-based ATC and JC08-based ATC were 0.0302V and 0.0896V respectively. By multiplying their corresponding acceleration factors, the total degradation voltage loss of the original NEDC and original JC08 operations were predicted. Error was calculated using equation (3.14).

The results of NEDC and JC08 total degradation voltage loss predictions and error are presented in Table 4-1 and Table 4-2.

Table 4-1 – NEDC Degradation Voltage Prediction

Simulated ATC Degradation Voltage	Acceleration Factor	Predicted NEDC Degradation Voltage	Simulated NEDC Degradation Voltage	Error
0.0302 V	1.75	0.0529 V	0.05 V	5.8%

Table 4-2 – JC08 Degradation Voltage Prediction

Simulated ATC Degradation Voltage	Acceleration Factor	Predicted JC08 Degradation Voltage	Simulated JC08 Degradation Voltage	Error
0.0296 V	1.77	0.0524 V	0.05 V	4.7%

By comparing the accuracy of the predictions made based on the three load cycles it can be observed that the accuracy of using the developed ATC to predict the degradation voltage of the original cycle increased from WLTP to NEDC and further to JC08. It was deduced that the increased accuracy was caused by the difference in cycle dynamics.

To prove the above hypothesis, the transient nature of the WLTP, NEDC and JC08 were further analysed. The harshness of each cycle was evaluated by their average current density output, number of load changes from increasing to decreasing current density (and vies versa), and maximum load change rate. The results are contained in Table 4-3 below.

Table 4-3 – The analysis of the transit nature of WLTP, NEDC, and JC08 cycles

	WLTP	NEDC	JC08	Unit
Average Current Density Output	0.097	0.054	0.0283	(A/cm^2)
Number of load changes from increasing to decreasing current density	60	49	46	—
Number of load changes from decreasing to increasing current density	60	49	46	—
Maximum Load Change Rate	0.021	0.020	0.007	(A/s)

From Table 4-3 it can be concluded that the average current density output, number of load changes, and maximum load change rate showed a decreasing trend from WLTP to NEDC and to JC08. It proved that the accuracy increased with the decreasing transient nature of the targeted real-world operations.

4.3 ATC Evaluation against Different Selection Criteria

4.3.1 Model Assessment

The selection criteria of the strategy are defined by the user and can be changed to meet users' demand. Different selection criteria produce different accelerated test cycles with different duration and acceleration factors. To analyse the effects of selection criteria on the accuracy of predicting degradation voltage loss, various selection criteria were applied for time steps selection. As demonstrated previously, by selecting a time steps with higher than average degradation rates, approximately 40% of the total time steps of the original operations are selected, producing an ATC of 493 hours in

duration with an acceleration factor of 1.74. Using the selection criteria of the developed WLTP-based ATC as a benchmark, selecting the top 10%, top 20%, top 30%, and top 50% of all the time steps of the original operations were used as new selection criteria for comparison. Illustrated in Figure 4.12 are the degradation rates of the initial 1800s of the WLTP simulation, together with the selection criteria of the top 10%, 40% (equivalent to the average degradation rates), and 50%. By choosing different selection criteria, different cut-off lines were generated to select qualified time steps for ATC development. The selection criteria of top 20% and 30% were also applied but not included in Figure 4.12 for clarity.

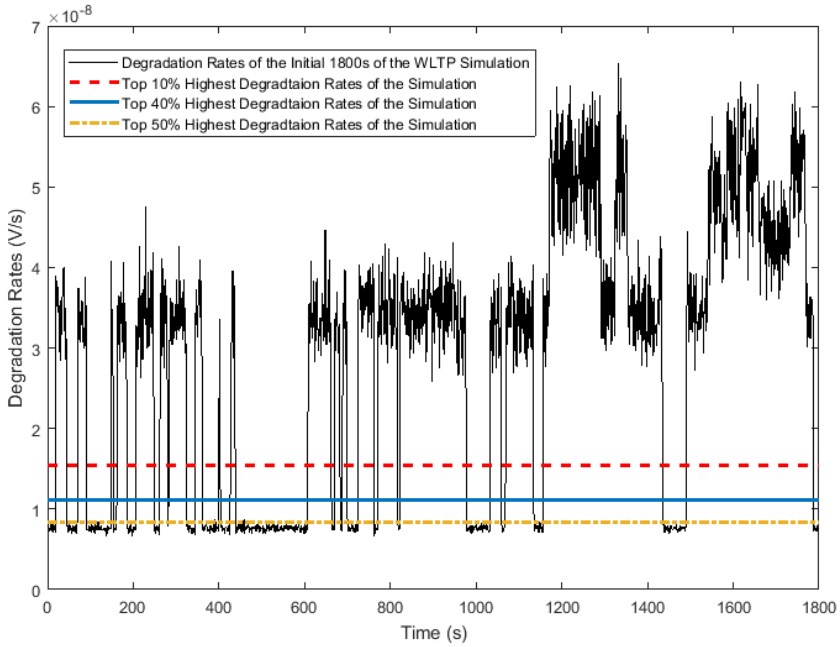

Figure 4.12 - Degradation rates of the initial 1800s of the WLTP simulation and different selection criteria

After the qualified time steps were selected, the ATCs were constructed by connecting the load information of the selected time steps in series. Degradation voltage loss remaining in each ATC was calculated using equation (3.11). The acceleration factor of each ATC was calculated using equation (3.12). Table 4-4 below contains the selection criteria, the durations and the acceleration factors of the developed ATCs. WLTP-based ATCs were named from ATCW1 to ATCW5 as presented in Table 4-4.

Table 4-4 – WLTP based acceleration test cycles with various acceleration factors

	ATCW 1	ATCW 2	ATCW 3	ATCW 4	ATCW 5	Original WLTP	Unit
Selection Criteria	Higher than Average DR (Top 40% Highest DR)	Top 10% Highest DR	Top 20% Highest DR	Top 30% Highest DR	Top 50% Highest DR	100% of the DR	
AF	1.74	5.22	3.07	2.20	1.52	1	
Duration	493	124	247	371	618	1236	Hours

The developed ATCs were simulated using the PEMFC degradation model and simulations were repeated 100 times for each ATC. The total degradation voltage loss caused by each ATC was the averaged value among the 100 simulations. Predictions of the total degradation voltage loss of the original WLTP operation were made by multiplying the degradation voltage loss of each ATC by its corresponding acceleration factor, and errors were calculated using equation (3.12). Table 4-5 below contained the simulated degradation voltage loss of each developed ATC, its corresponding acceleration factor, its prediction of the original WLTP operation, and the calculated error.

Table 4-5 – WLTP based accelerated test cycles predictions and error

	ATCW1	ATCW2	ATCW3	ATCW4	ATCW5	Original WLTP	Unit
AF	1.74	5.22	3.07	2.20	1.52	1	
Simulated ATCWs degradation Voltage Loss	0.0311	0.0118	0.0188	0.0267	0.0347	0.0501	V
Predicted WLTP Degradation Voltage	0.0541	0.0616	0.0577	0.0558	0.0527	0.0501	V
Error	8.2	23.2	15.4	11.6	5.3	0.2	%

From Table 4-4 and Table 4-5 it can be concluded that the duration and the acceleration factor of the ATCs changed with the variation of the selection criteria. The smaller the acceleration factor, the less the original cycle was condensed, the longer the duration of the ATC, and the more accurate the degradation voltage prediction made. When the acceleration factor equalled 1, the original load cycle was not accelerated at all and the error of simulating the original WLTP was negligible.

Similar comparisons were done for NEDC-based and JC08-based ATCs development, and the results were shown in Table 4-6 and Table 4-7. ATCs based on the NEDC simulation and JC08 simulations were named from ATCN1 to ATCN5, and ATCJ1 to ATCJ5, respectively.

Table 4-6 –NEDC based acceleration test cycles with various acceleration factors

	ATCN1	ATCN2	ATCN3	ATCN4	ATCN5	Original NEDC	Unit
Selection Criteria	Higher than Average DR (Top 40% Highest DR)	Top 10% Highest DR	Top 20% Highest DR	Top 30% Highest DR	Top 50% Highest DR	100% of the DR	
AF	1.75	5.54	3.15	2.22	1.53	1	
Duration	504	127	254	381	798	1270	Hours

Table 4-7 – JC08 based acceleration test cycles with various acceleration factors

	ATCJ1	ATCJ2	ATCJ3	ATCJ4	ATCJ5	Original JC08	Unit
Selection Criteria	Higher than Average DR (Top 40% Highest DR)	Top 10% Highest DR	Top 20% Highest DR	Top 30% Highest DR	Top 50% Highest DR	100% of the DR	
AF	1.77	5.89	3.24	2.26	1.54	1	
Duration	511	129	259	388	647	1293	Hours

The NEDC-based and JC08-based ATCs were simulated using the PEMFC degradation model to obtain the total degradation voltage of each ATC. Prediction of the total degradation voltage loss of the original NEDC and JC08 operations were made by multiplying the degradation voltage of an ATC by its acceleration factor. The predicted total degradation voltage loss of the NEDC and JC08 operation were presented in Table 4-8 and Table 4-9, respectively.

Table 4-8 –NEDC based accelerated test cycles predictions and error

	ATCN1	ATCN2	ATCN3	ATCN4	ATCN5	Original NEDC	Unit
AF	1.75	5.54	3.15	2.22	1.53	1	
Simulated ATCNs degradation Voltage Loss	0.0302	0.011	0.018	0.0246	0.0127	0.05	V
Predicted WLTP Degradation Voltage	0.0529	0.0609	0.0568	0.0546	0.0520	0.05	V
Error	5.8	21.7	13.6	9.2	4.1	0	%

Table 4-9 – JC08 based accelerated test cycles predictions and error

	ATCJ1	ATCJ2	ATCJ3	ATCJ4	ATCJ5	Original JC08	Unit
AF	1.77	5.89	3.24	2.26	1.54	1	
Simulated ATCJs degradation Voltage Loss	0.0297	0.0101	0.0174	0.024	0.0337	0.05	
Predicted WLTP Degradation Voltage	0.0526	0.0597	0.0563	0.0543	0.0519	0.05	V
Error	5.1	19.3	12.6	8.6	3.7	0	%

The errors of the three operations are shown in Figure 4.13 below. By comparing the three error curves it can be proved that the error of the three operations followed the same trends, and the error increased with the increasing acceleration factor and increased level of condensation of the original operations. It demonstrated that the accelerated test cycle development strategy was able to condense real-world PEMFC operations into accelerated test cycles with different acceleration factors using verifying

selection criteria to accurately predict the degradation voltage loss of the original operations.

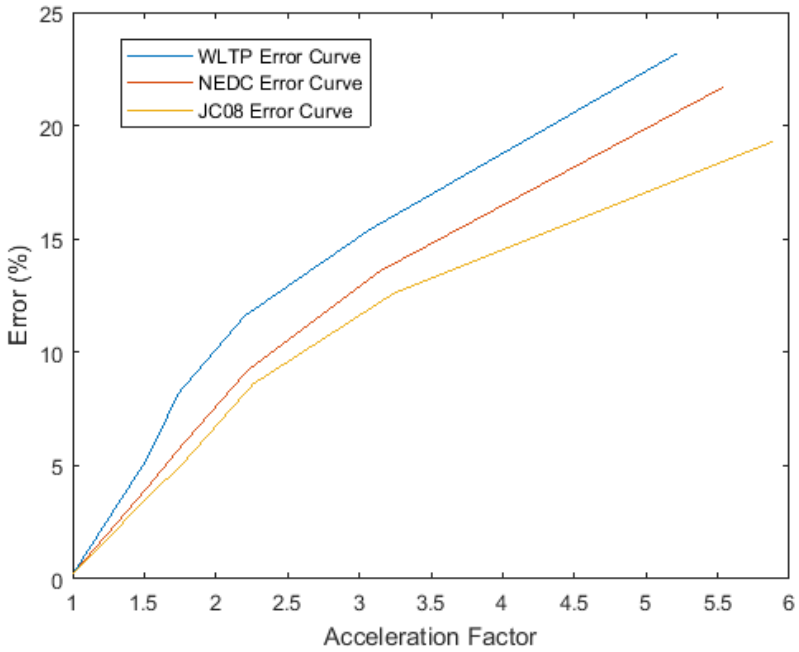

Figure 4.13 – Error curves of WLTP, NEDC, and JC08 predictions

4.3.2 Experimental Validation

The relationship between selection criteria and the error were validated through experiments. Based on the model simulation results of 400 WLTP operation, the 400-WLTP-based ATCs were developed using different selection criteria, which were the average rate (calculated as equivalent to top 14%), top 10%, 30%, top 40%, and 50% highest, respectively. Durations and acceleration factors of the 400-WLTP-based ATCs were presented in Table 4-10.

Table 4-10 – 400 WLTP cycles based ATCs with various acceleration factors

	ATC1	ATC2	ATC3	ATC4	ATC5	Original JC08	Unit
Selection Criteria	Higher than Average DR (Top 14% Highest DR)	Top 10% Highest DR	Top 30% Highest DR	Top 40% Highest DR	Top 50% Highest DR	100% of the DR	
AF	2.33	2.89	1.79	1.60	1.45	1	
Duration	27	20	60	80	100	200	hours

Each ATC listed in Table 4-10 was tested three times, and the degradation voltage loss of the three testes were averaged out and regarded as the degradation voltage loss caused by the corresponding ATC. Table 4-11 contains the experimental results of the ATCs and the predictions of degradation voltage of the 400-WLTP operation. The predictions were compared to the tested 400-WLTP operation degradation voltage to calculate error.

Table 4-11 – 400 WLTP cycles based ATCs experimental results and predictions with error

	ATC1	ATC2	ATC3	ATC4	ATC5	Original WLTP	Unit
Experimental Tested ATCs Degradation Voltage	0.0053	0.0046	0.0066	0.0079	0.0082	0.0106	V
AF	2.33	2.89	1.79	1.60	1.45	1	
Predicted 400 WLTP Degradation Voltage	0.0126	0.0133	0.0122	0.0121	0.0119	0.0106	V
Error	18.86	25.47	15.09	14.15	12.26	—	%

The tested degradation voltage loss of the 400-WLTP-based ATCs were successfully obtained and used to predict the degradation voltage loss of the

400-WLTP operations. A plot of the error against the acceleration factors of the ATCs was produced and presented in Figure 4.14.

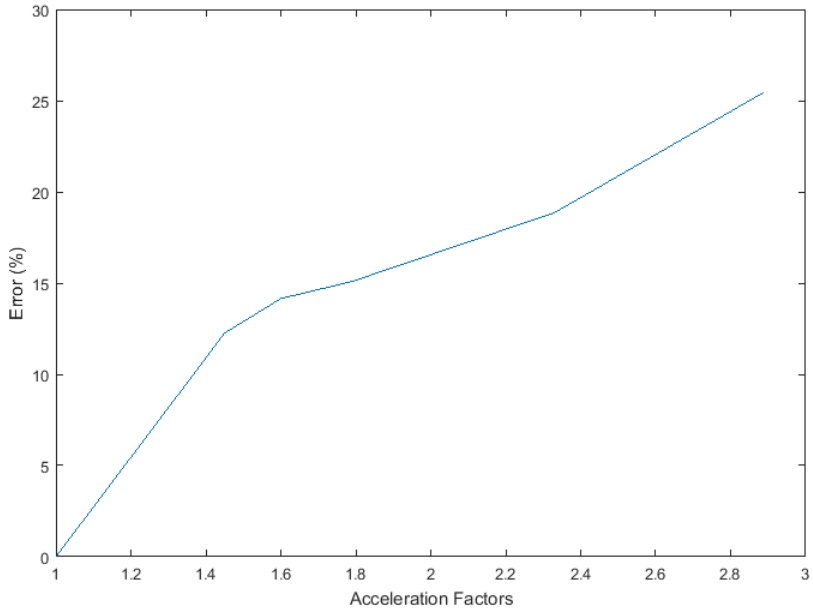

Figure 4.14 – Errors variations against acceleration factors

From Figure 4.14 it can be observed that with the increasing acceleration factors, the accuracy of the degradation voltage loss prediction decreased with the increasing error. The trend of the error obtained from the experimental results of using 400-WLTP-based ATCs to predict the degradation voltage loss of the 400-WLTP operation showed a strong correlation with that produced from model assessment of using WLTP-based ATCs to predict degradation voltage loss of the simulated WLTP operation.

The increase in error is because the ATCs were developed based on model calculation of the degradation contribution of the time steps, and the degradation rates used in the model were average value representing the severity of degradation during a long-term operation. The more degradation voltage remaining in the ATC, the longer the testing time, the closer the actual degradation rates to those used in the model and the smaller the error.

4.4 ATC Evaluation against Different Models

To evaluate the effects of the accuracy of the degradation model used to the ATC development strategy, two different models introduced in Chapter 2.4 were used to simulate WLTP PEMFC operations. The original PEMFC

degradation model was referred as Model 1, and the modified model was referred as Model 2.

4.4.1 Models Comparison

Simulations of 1 WLTP cycle were run using the two models for comparison and the degradation voltage loss calculated by Model 1 and Model 2 were presented in Figure 4.15 and Figure 4.16.

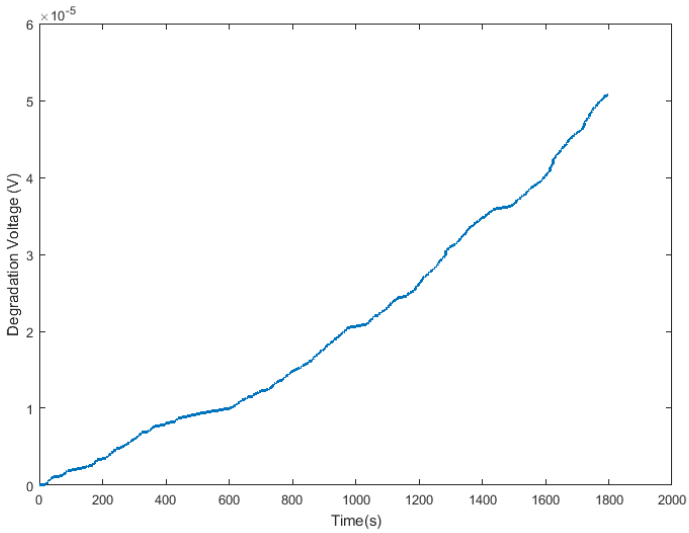

Figure 4.15 – Model 1 calculation of degradation voltage loss of one WLTP cycle

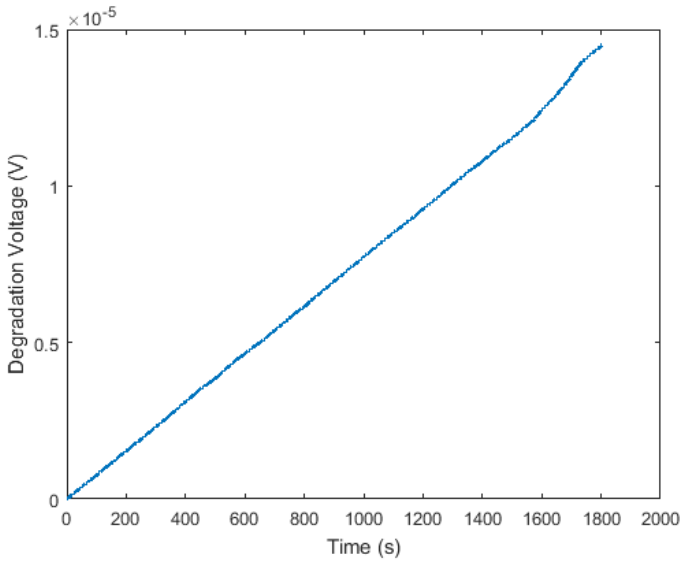

Figure 4.16 – Model 2 calculation of degradation voltage loss of one WLTP cycle

Degradation rates during the 1800s were also obtained by differentiating the degradation voltage loss and the results were presented in Figure 4.17 and Figure 4.18.

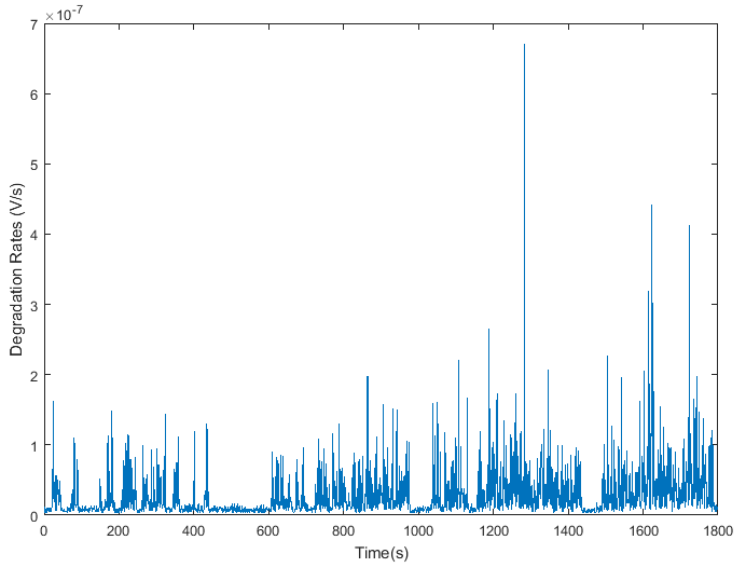

Figure 4.17 – Degradation rates of the initial 1800s of the WLTP Model 1 simulation

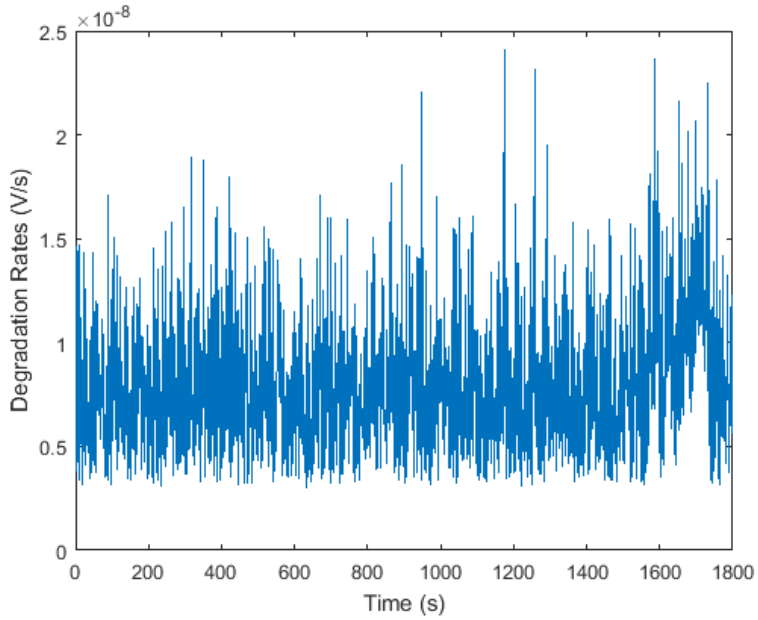

Figure 4.18 – Degradation rates of the initial 1800s of the WLTP Model 2 simulation

By comparing the degradation voltage loss and degradation rates of 1 WLTP cycle simulated using the two different models it can be observed that the

degradation voltage loss simulated by Model 1 was over 3 times higher than that simulated by Model 2. The average degradation rates calculated from Model 2 simulation was 7.79 x 10^{-9} V/s, much lower than that calculated from Model 1 simulation, 1.12 x 10^{-8} V/s.

Simulations of long-term PEMFC calculations were also carried out using the two models. WLTP load profiles were simulated using the two models until the cumulative degradation voltage loss reached 0.05V. The degradation voltage accumulation and the degradation rates simulated using Model 1 are presented in Figure 3.5 and Figure 3.7, and those simulated using Model 2 are presented in Figure 4.19 and Figure 4.20. The cumulative degradation voltage in Figure 4.19 appears to be linear is because the time range is wide, and if the figure is zoomed in, it can be observed that the voltage accumulation rates varied with time.

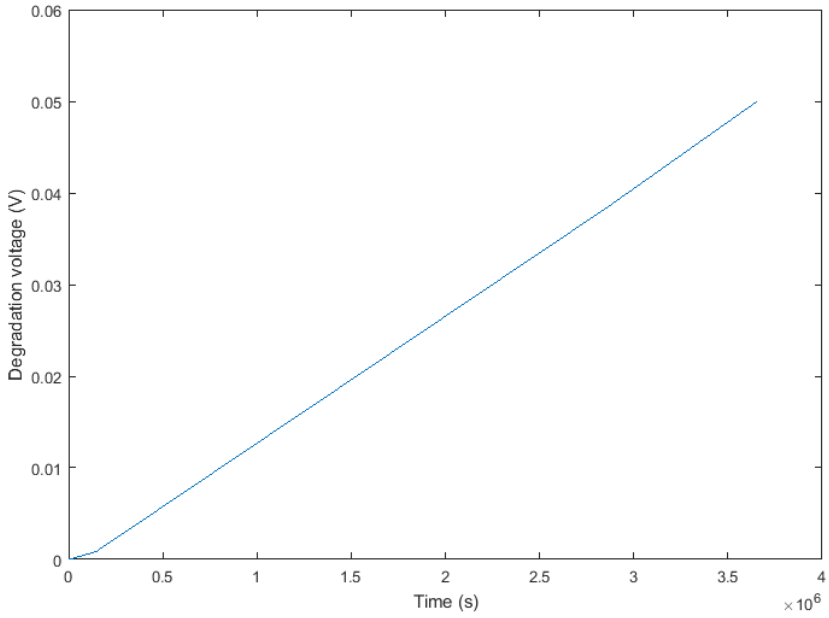

Figure 4.19 – Model 2 simulated cumulative WLTP degradation voltage

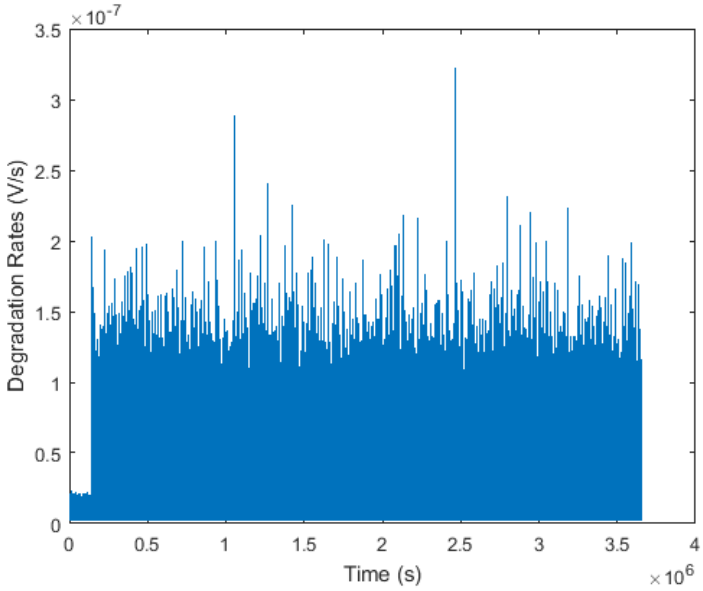

Figure 4.20 – Degradation rates of the Model 2 WLTP operation simulation

The simulation completed 1068 hours of WLTP operations before the total degradation voltage loss reached 0.05V, over 150 hours earlier than that simulated using Model 1.

4.4.2 Results Analyses

PEMFC WLTP operations were simulated using both Model 1 and Model 2 until the cumulative degradation voltage loss reached 0.05V, and WLTP-based ATCs were developed using Model 1 and Model 2. Simulations using each model were repeated 100 times and average cumulative degradation voltage loss and degradation rates of each time step were obtained. Model 1 predicted a lifetime of 1236 hours and Model 2 predicted a lifetime of 1068 hours for WLTP operations. The accuracy of the two models was validated through experiments in Chapter 3.3.3 and the results proved that the accuracy of utilising Model 1 to predict long-term PEMFC operations was higher than that of using Model 2.

After degradation rate of each time step was estimated, ATCs were developed according to different selection criteria. The selection criteria used to develop ATCs were the highest 10%, 20%, 30%, 40% and 50% degradation rates. The Model1-based ATCs were developed in Chapter 4.3.1 and presented in Table 4-4. The Model2-based ATCs were developed in this section and presented in Table 4-12 below. The developed Model2-based ATCs were named ATCM1 to ATCM5 with increasing acceleration factors. With the increasing degradation information remained in the developed ATCs, the acceleration

factors of the ATCs developed from Model 2 were 1.75, 1.85, 2.97, 3.83 and 6.89, respectively.

Table 4-12 – WLTP based acceleration test cycles with various acceleration factors developed using Model 2

	ATCM1	ATCM2	ATCM3	ATCM4	ATCM5	Original WLTP	Unit
Selection Criteria	Higher than Average (Top 40% Highest)	Top 10% Highest	Top 20% Highest	Top 30% Highest	Top 50% Highest	100%	
AF	1.85	6.89	3.83	2.97	1.75	1	
Duration	427	107	213	321	355	1068	Hours

By comparing ATCs developed from Model 1 and Model 2 it can be found that the ATCs developed using the same selection criteria from the two models were different. This is because the two models predict different degradation effects for a same time step which may result in different time steps being selected to construct the ATCs. In this research, Model 1 was used as a simulation tool to represent real-world experiments and evaluate the error because it was evaluated as the more accurate model of the two in validation section.

The developed ATCs were input to Model 1 to calculate their corresponding degradation voltage loss and predictions of the total degradation voltage loss. The original WLTP operations were made by multiplying the calculated degradation voltage loss of the ATCs by their corresponding acceleration factors, and results were presented in Table 4-13.

Table 4-13–Model2-Based ATCs Predictions and Error

	ATCM1	ATCM2	ATCM3	ATCM4	ATCM5	Unit
Model1 Simulated WLTP Degradation Voltage loss	0.05	0.05	0.05	0.05	0.05	V
Predicted Degradation Voltage Using Model2-Based ATCs	0.0567	0.0654	0.063	0.0594	0.0547	V
Error of Model2-Based ATCs	13.4%	30.8%	26%	18.8%	9.4%	

The error of using the two models to develop ATCs and predict the degradation voltage loss of the original cycles were compared and plotted against acceleration factors of the ATCs and was presented in Figure 4.21.

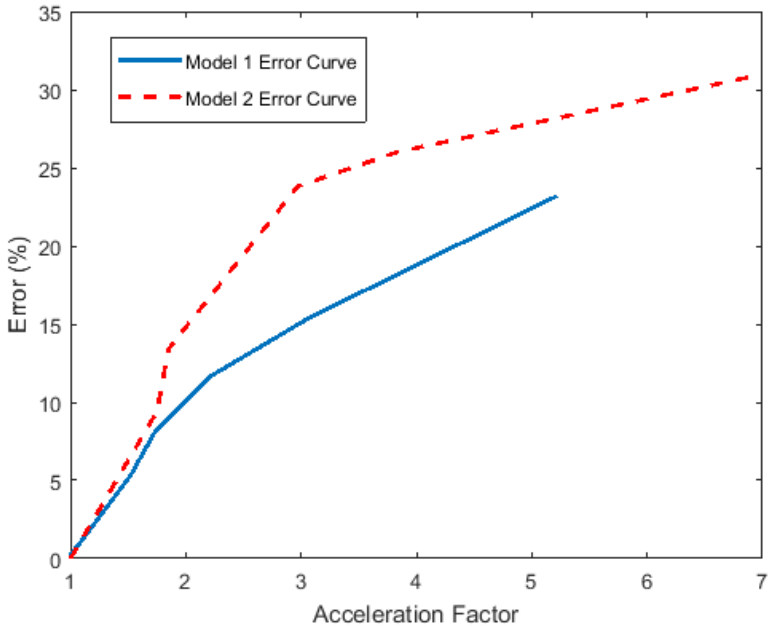

Figure 4.21 – Comparison of the errors of the prediction made based on Model 1 and Model 2

From Figure 4.21 it can be concluded that the degradation voltage predictions made based on the ATCs development from Model 2, which was believed to be less accurate than Model 1, were less accurate compared with those made based on Model 1. However, the variation trend between error and degradation voltage remaining in the ATCs was the same between the two models. the smaller the acceleration factor, the more degradation voltage remained in the ATCs, and therefore, the bigger the error.

The acceleration factors are the ratio of the degradation voltage loss of the original cycles to that of the condensed ATCs. It is calculated specifically to the number of cycles chosen and varies according to different number of cycles chosen.

Ideally, a continues time function is needed that can describe the relationship between acceleration factor and the duration of the condensed ATC, and to analyse the error variations. However, it is impractical because the ATCs are constructed according to the defined selection criteria, which specify the threshold of the selection of time steps. This produces ATCs with fixed candidate time steps, and therefore, fixed acceleration factor and duration. It is difficult to analyse the error against continues time frames. As a result, the error is analysed against different acceleration factors instead of durations of ATCs, and the effects of time is represented by the acceleration factors because different acceleration factors produces ATCs with various durations. The calculation of the acceleration factors will produce errors as well. This error is not calculated separately, but is included in the overall error of the degradation voltage loss predictions.

Another angle to look at the error is to evaluate the effects of different duration of the original cycles completed because running different length of the original cycles will result in different average degradation voltage, and affect the threshold of the candidate time steps, the acceleration factor and the duration of the condensed ATC, and the error of the prediction made. However, because the failure condition is pre-defined, and the calculation and selection process are based on the average value, the duration of the original cycles will be fixed. Therefore, the effects of different duration of the original cycles are not considered here.

In conclusion, the model-based ATCs development strategy requires a model with reasonable accuracy to predict degradation voltage loss to ensure the accuracy of the developed ATCs and therefore, accurate degradation voltage loss prediction of the targeted real-world operations. The accuracy of the real-world operation degradation voltage prediction increases with the accuracy of the model.

4.5 Conclusions

In this chapter, the accelerated stress test development strategy was analysed in terms of the sensitivity to the targeted real-world applications, the selection criteria applied, and the PEMFC performance and degradation model used. The results proved that the accuracy of using the developed accelerated test cycles to predict the degradation voltage loss of the original operation decreased with the more rapid transit nature of the targeted real-world applications. The error of predicting WLTP, NEDC, and JC08 degradation voltage loss using the corresponding developed ATCs decreased from 18% to 6%, and 5%, respectively. The accuracy also decreased with the decreasing acceleration factor of the test cycle. The error of using the ATCs, the acceleration factor of which were 5.22, 3.07, 2.2, 1.74, and 1.52, to predict the degradation voltage loss of the WLTP cycles were 23%, 15%, 12%, 8%, and 5%, respectively. This has been proved through experiments by testing the ATCs developed based on 400 WLTP cycles. The acceleration factor of the ATCs were 2.89, 2.33, 1.79, 1.6, and 1.45, and the error between the tested 400 WLTP cycles and the predicted were 25%, 19%, 15%, 14%, and 12%. The accuracy also decreased with the decreased accuracy of the model. The error of using the ATCs developed using Model 2 were 31%, 26%, 19%, 13%, and 9%. Compared with the error of Model 1 it was concluded that for the same acceleration factor, the error of the prediction made using Model 2 developed ATCs were higher than those made using Model 1 developed ATCs. To improve the accuracy of this strategy, an accurate PEMFC performance and degradation model is required, with appropriately selected acceleration factor.

Chapter 5

5 Applying Developed Strategy to Real Driving Emissions

5.1 Introduction and Background Study of RDE

According to research [149], vehicle emissions measured in real-world driving conditions are always higher than those measured in a laboratory. This is not only due to real-world driving results in higher speed and acceleration, but also the engine and after-treatment system is calibrated in laboratory conditions rather than real driving conditions [150]. NEDC has been used in Europe for vehicle emissions measurement and calibration in laboratory conditions since 1970, and it has been criticised for being a poor representative of real-world driving conditions due to its narrow range of acceleration-velocity conditions [151]. As a result, WLTP cycle was developed based on over 700,000 km of real-world driving data from 5 regions located in Asia, Europe and the US [152]. Although the WLTP was believed to be a better representation of real-driving conditions compared to NEDC, it still fails to capture some key factors such as traffic, driving behaviour, and route severities, which all result in higher emissions [153]. To minimise the difference between emissions obtained from laboratory tests and real-world driving, Real Driving Emission tests were introduced from September 2017 as a complement of the WLTP cycle [154] [155]. The Real Drive Emission drive cycles are recorded from driving a test vehicle following a test route. The acceleration-velocity conditions together with other real-world driving factors such as traffic, driving behaviours etc. are well captured. Emissions were measured onboard by portable emissions measurement system, and currently the RDE NOx emission limit is defined in a not-to-exceed form, and the limit is calculated by multiplying the Euro 6 limit by a conformity factor.

Although RDE tests were designed to minimise on-road emissions, especially NOx emissions from diesel-powered vehicles, the testing strategy has different potentials for PEMFC-powered vehicles. When comparing fuel cells with internal combustion engines, durability of fuel cells has much in common with emissions of IC engines. As stated in Chapter 1, the durability of a fuel cell will also be significantly affected by its operating conditions, and it is reasonable to assume that durability measured in laboratory condition

will be different from that obtained in real-world operating conditions because of different driving factors such as acceleration-velocity distribution. Therefore, it is reasonable to assume that the concept of RDE tests can be applied to PEMFC-powered vehicles and should be considered as an important factor in production and quality control.

In this chapter, three Real Drive Emission drive cycles obtained from literatures were used to prove that the developed accelerated test cycle development strategy can be applied not only in laboratory conditions, but also in real-world driving scenario to predict the degradation voltage in a condensed time frame.

5.2 Methodology of Applying ATC Development Strategy to RDE

Applying the developed accelerated test cycle strategy to RDE involves 4 steps: 1. Converting RDE drive cycles into fuel cell load cycles. 2. RDE fuel cell load cycles simulations and degradation voltage calculation. 3. ATC development based on degradation rates of each time step calculated from the model calculated degradation voltage. 4. RDE fuel cell load cycle degradation voltage prediction. Each step is introduced in detail in this chapter.

5.2.1 RDE Cycles Conversion

In this study, in order to prove the applicability of this strategy to real-world driving scenario, three RDE drive cycles were obtained from literatures and presented in Figure 5.1 to Figure 5.3. They are named RDE drive cycle 1 [156], RDE drive cycle 2 [157], and RDE drive cycle 3 [158].

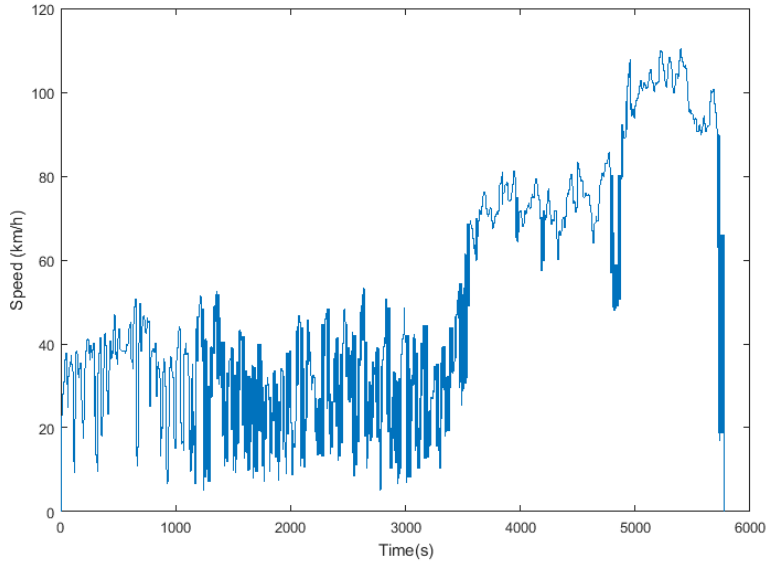

Figure 5.1 – RDE drive cycle 1

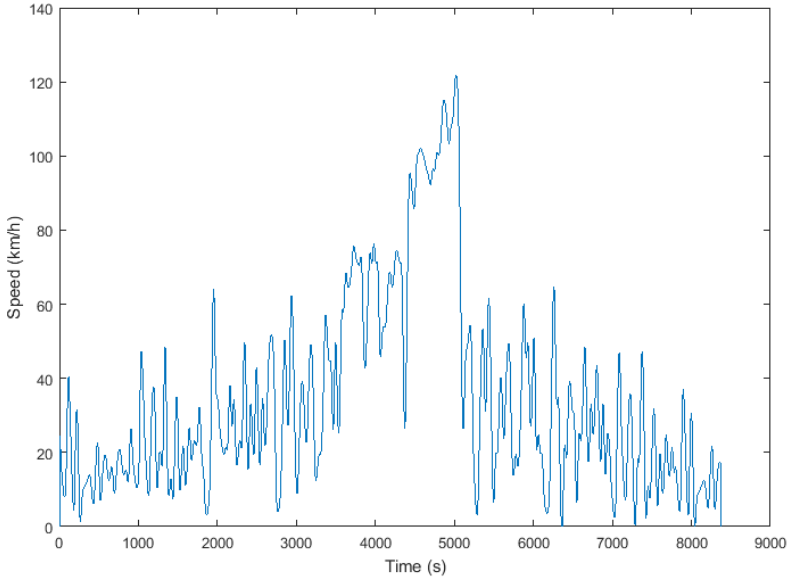

Figure 5.2 – RDE drive cycle 2

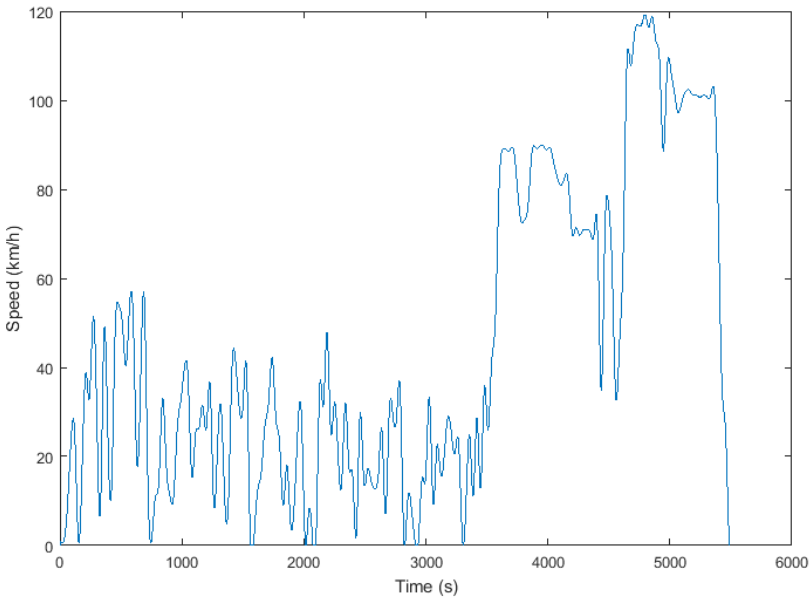

Figure 5.3 – RDE drive cycle 3

To convert vehicle drive cycle into fuel cell load cycle, as introduced in Chapter 3.2.1, the power demand of the RDE drive cycles were firstly calculated and a normalised PEMFC polarisation curve and power curve were used to match the power demand of the data points in the drive cycles with PEMFC power output. By doing this, the required load and voltage output of a PEMFC can be determined and the RDE drive cycles converted into RDE tests fuel cell load profiles. The converted RDE fuel cell load profiles are shown in Figure 5.4 to Figure 5.6, and the cycles were named as RDE PEMFC load cycle 1, RDE PEMFC load cycle 2, and RDE PEMFC load cycle 3 accordingly.

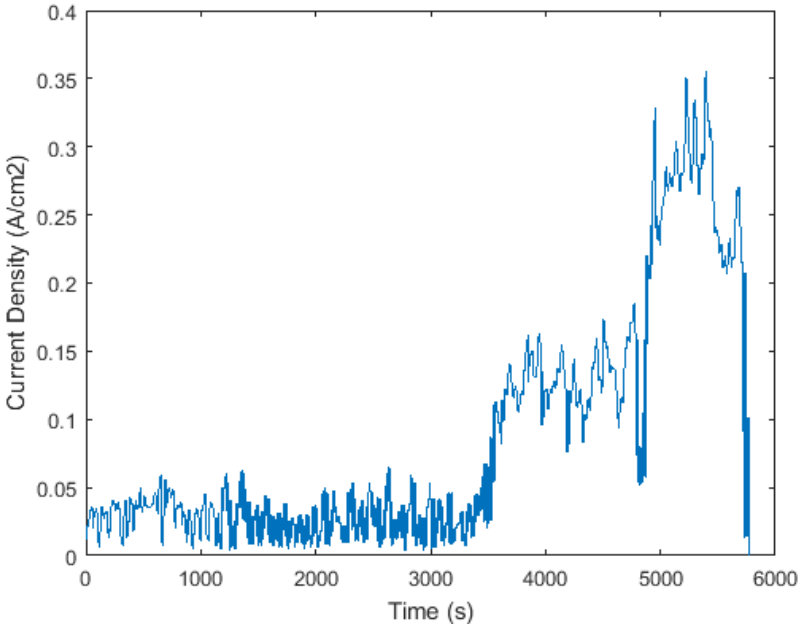

Figure 5.4 – RDE PEMFC load cycle 1

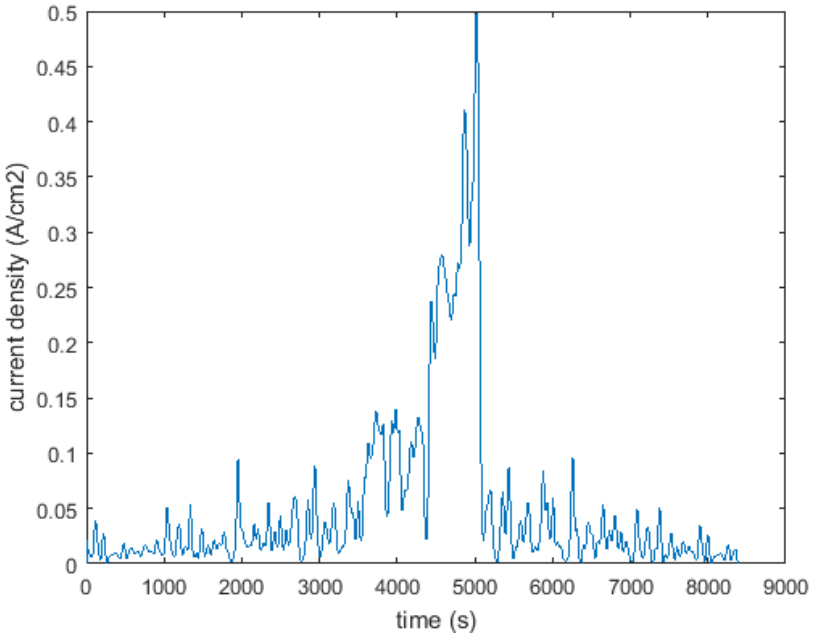

Figure 5.5 – RDE PEMFC load cycle 2

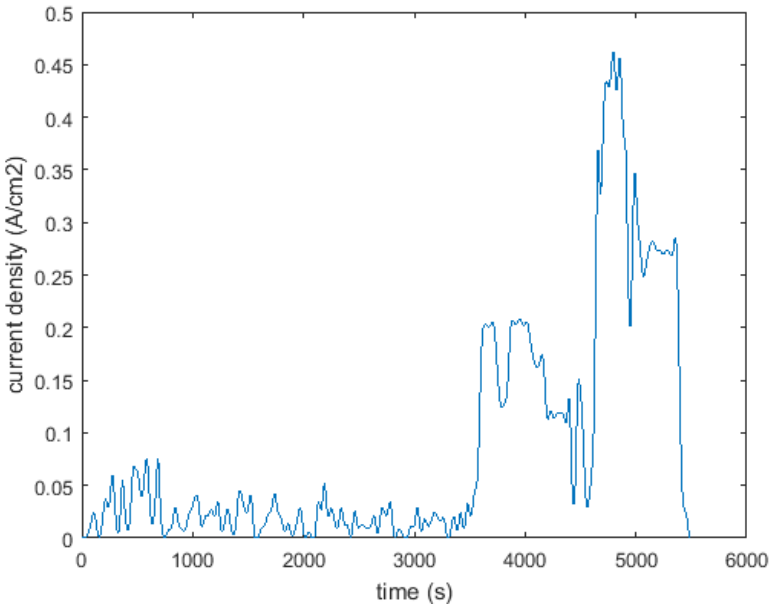

Figure 5.6 – RDE PEMFC load cycle 3

The average current density output, the number of load increase and decrease operations, and the maximum load change rate of the three RDE cycles were presented in Table 5-1 to compare the transit nature. By comparing the transit nature of the RDE load profiles with that of the WLTP, NEDC and JC08 load profiles, the most significant difference between real-world driving and laboratory duty cycles was that real-world driving was more dynamic and had higher frequency and sharper speed changes. The average current density output was also higher than that of the laboratory-based cycles. Similar to the effects on vehicle emissions, this would result in a considerable increase in degradation phenomenon in PEMFCs.

Table 5-1 – The analysis of the transit nature of the RDE PEMFC load cycle 1 to 3

	RDE 1	RDE 2	RDE 3	Unit
Average Current Density Output	0.086	0.051	0.081	(A/cm^2)
Number of Load Increase	106	75	61	—
Number of Load Decrease	106	75	61	—
Maximum Load Change Rate	0.115	0.081	0.011	(A/s)

5.2.2 RDE Cycles Degradation Voltage Model Calculation

After converting the RDE tests drive cycles into fuel cell load profiles, the three load profiles were input into the Petri Nets model to calculate the degradation voltage caused by the profiles.

Because the RDE load profiles are shorter but more dynamic, it can be expected that the degradation caused by extreme voltage or load output and sharp load change will domain the degradation phenomenon.

To calculate the degradation voltage caused by the RDE fuel cell load profiles, simulations were run 100 times for each profile to ensure the accuracy of the calculated degradation voltage. The degradation voltage of each time step calculated from each simulation were averaged out and regarded as the actual degradation voltage of the time step. Figure 5.7 presented the averaged degradation voltage loss of one RDE load profile 1.

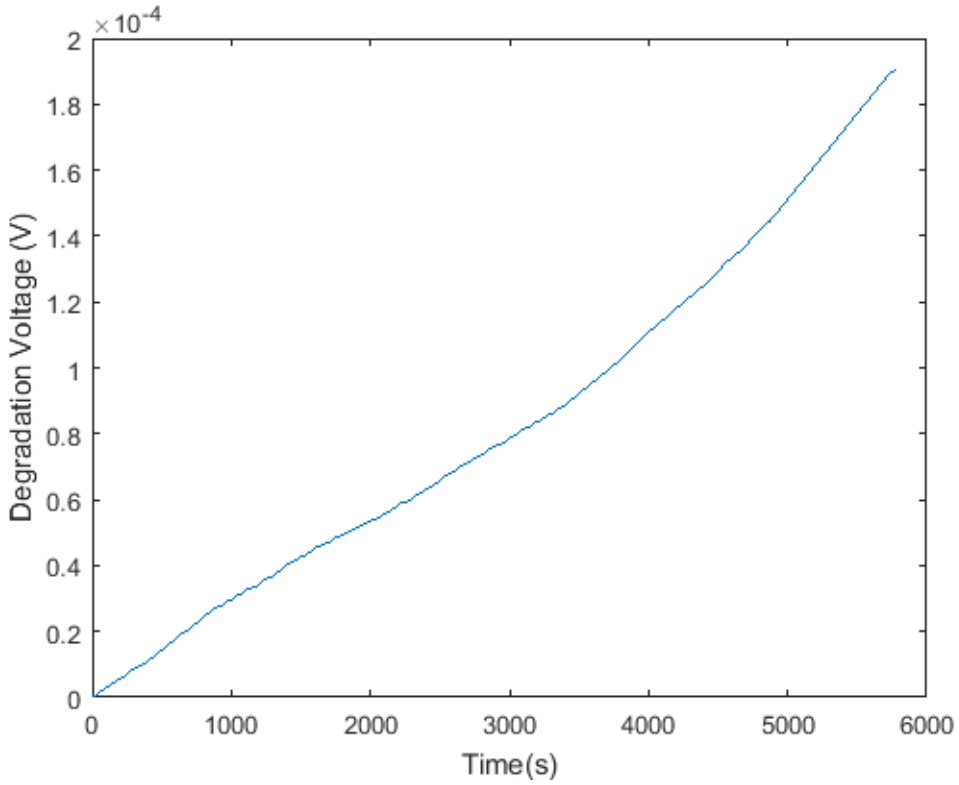

Figure 5.7 – Cumulative degradation voltage loss of RDE load cycle 1

The overall degradation voltage loss of RDE load cycle 1 was 1.91 x 10^{-4} V, with an average degradation rate of 3.33 x 10^{-8} V/s. The comparison between RDE and WLTP, NEDC and JC08 with equivalent operation time were represented in Table 5-2 below.

Table 5-2 Degradation comparison between RDE, WLTP, NEDC, and JC08

	RDE Load Cycle 1	3 Cycles of WLTP	5 Cycles of NEDC	5 Cycles of JC08	Unit
Duration	5777	5400	5915	6000	s
Degradation Voltage	1.91 x 10^{-4}	1.53 x 10^{-4}	1.46 x 10^{-4}	1.38 x 10^{-4}	V
Average Degradation Rate	3.33 x 10^{-8}	2.83 x 10^{-8}	2.47 x 10^{-8}	2.3 x 10^{-8}	V/s

The results proved that the RDE load profile did cause higher and faster degradation voltage loss compared with laboratory drive cycles, such as WLTP, NEDC, and JC08. Degradation rate of each time step of RDE load

cycle 1 was calculated by differentiating the degradation voltage, and the degradation rates were presented in Figure 5.8.

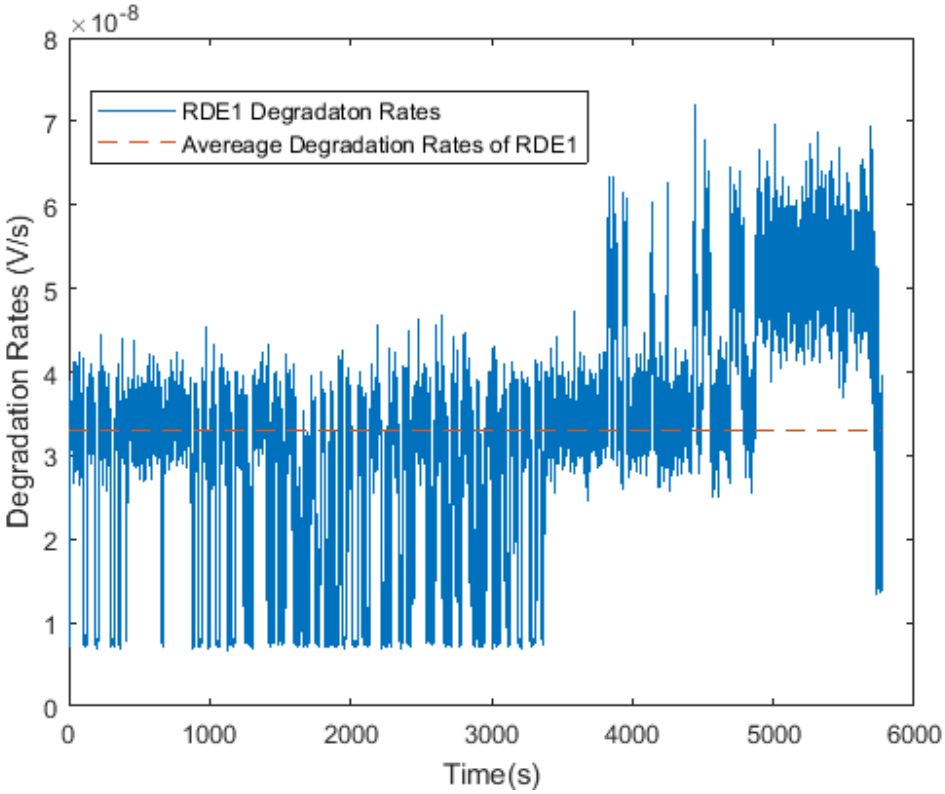

Figure 5.8 – Degradation rates of RDE load cycle 1 simulation

RDE load cycle 2 and 3 were also simulated 100 times to calculate average degradation voltage and degradation rate of each time step. The results were shown in Figure 5.9 to Figure 5.12. The degradation voltage losses of RDE load cycle 2 and 3 were 1.89 x 10^{-4} V and 1.59 x 10^{-4} V, and the overall degradation rates were 2.26 x 10^{-8} V/S and 2.90 x 10^{-8} V/S, respectively. The degradation rates of RDE load cycle 2 and 3 were lower than that of RDE load cycle 1, which was 3.33 x 10^{-8} V/s, but the overall degradation rates of RDE load cycle 1 and 3 were higher than WLTP, NEDC, and JC08. The overall degradation rate of RDE load cycle 2 was also higher than that of the JC08 cycle.

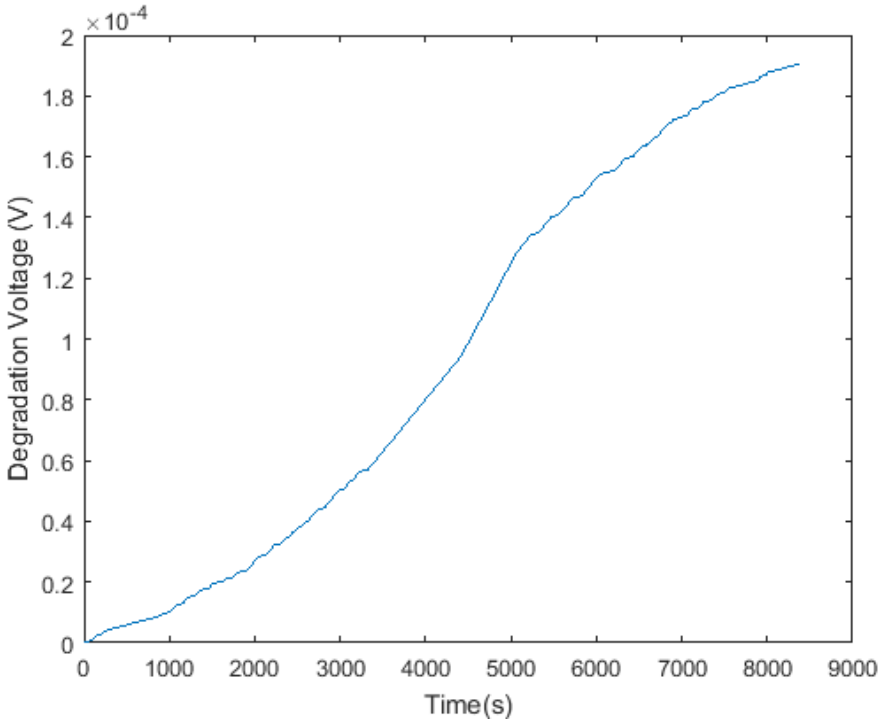

Figure 5.9 – Cumulative degradation voltage loss of RDE load cycle 2

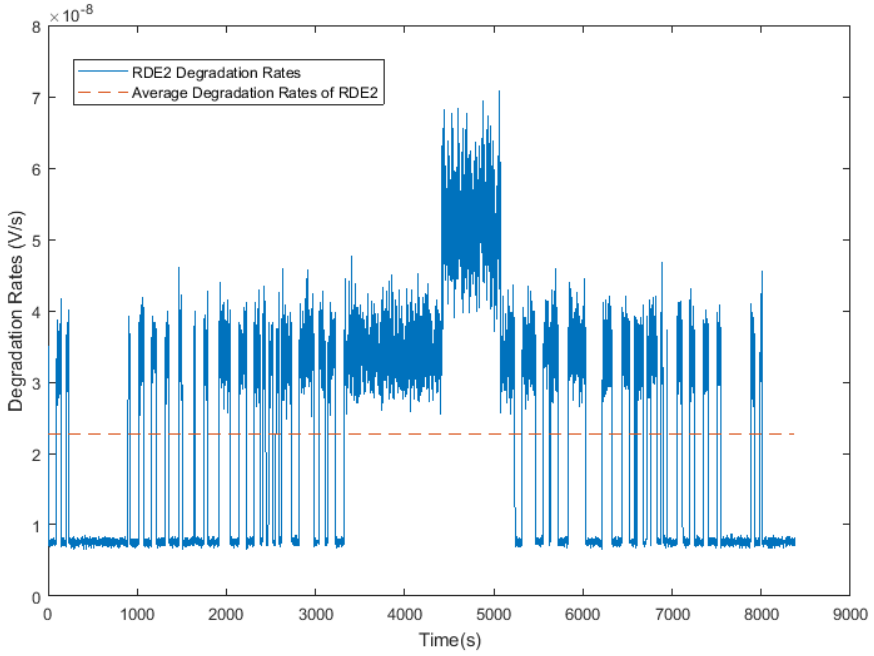

Figure 5.10 – Degradation rates of RDE load cycle 2 simulation

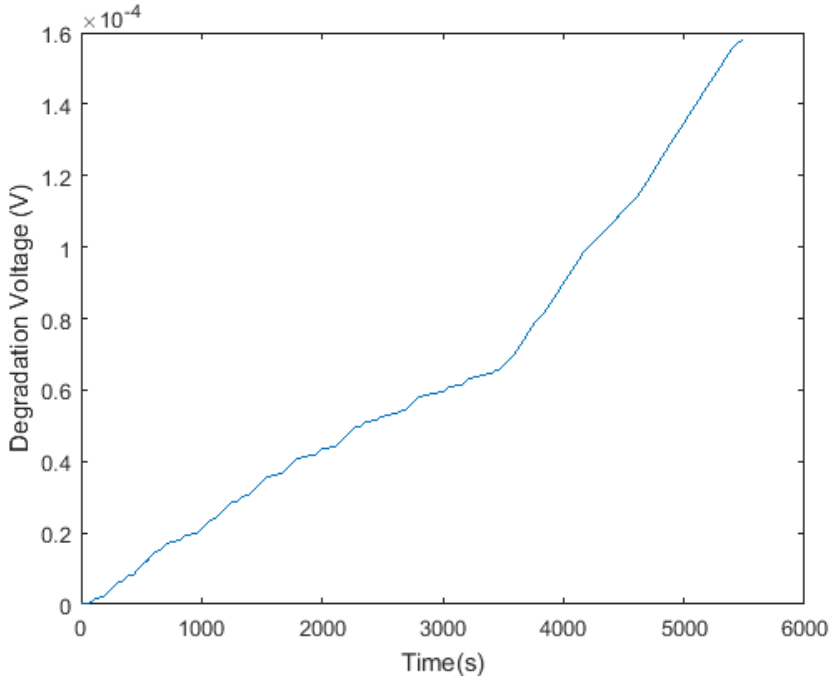

Figure 5.11 – Cumulative degradation voltage loss of RDE load cycle 3

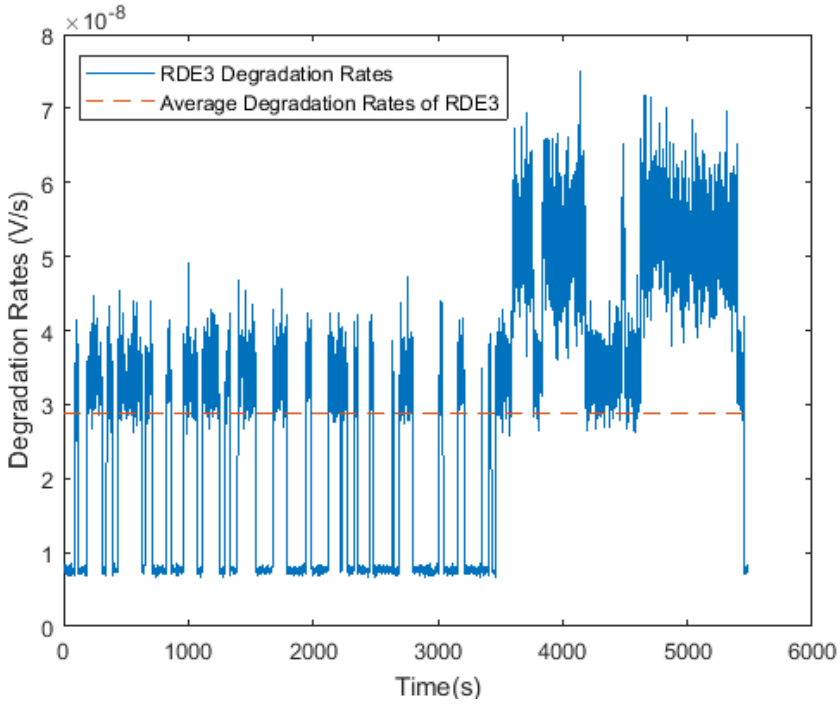

Figure 5.12 – Degradation rates of RDE load cycle 3 simulation

5.2.3 RDE-Based ATC Development

According to the calculated degradation voltage loss and degradation rates of RDE load cycle 1 to 3, the RDE-based ATCs were developed to condense the time period of the load cycles while the degradation voltage of the load cycles can still be predicted.

The red dashed line in Figure 5.8 represented the average degradation rates throughout the simulation of RDE1 load cycles. The selection criteria adopted here involved selecting the time steps for which the degradation rates were higher than the average degradation rate. According to the chosen selection criteria, all the time steps with degradation rates above this line were selected to construct the ATC. The ATC was developed by connecting the selected time steps in series and was named RDE load cycle 1 based ATC1 (RDE1-ATC1). Another RDE1 based ATC was also developed to make comparison, and the selection criteria of which was selecting the time steps with the highest 30% degradation rates, named RDE1-ATC2. The two ATCs were presented in Figure 5.13 and Figure 5.14 and compared with the original RDE1 load cycle. By comparing RDE1-ATC1, RDE1-ATC2, and RDE1 load cycle it can be observed that by selecting the time steps with degradation rates higher than average, the duration of the RDE load cycle was condensed by 45%, from 5777s to 3209s. By selecting the top 30% highest degradation rates, the duration was further condensed to 1734s.

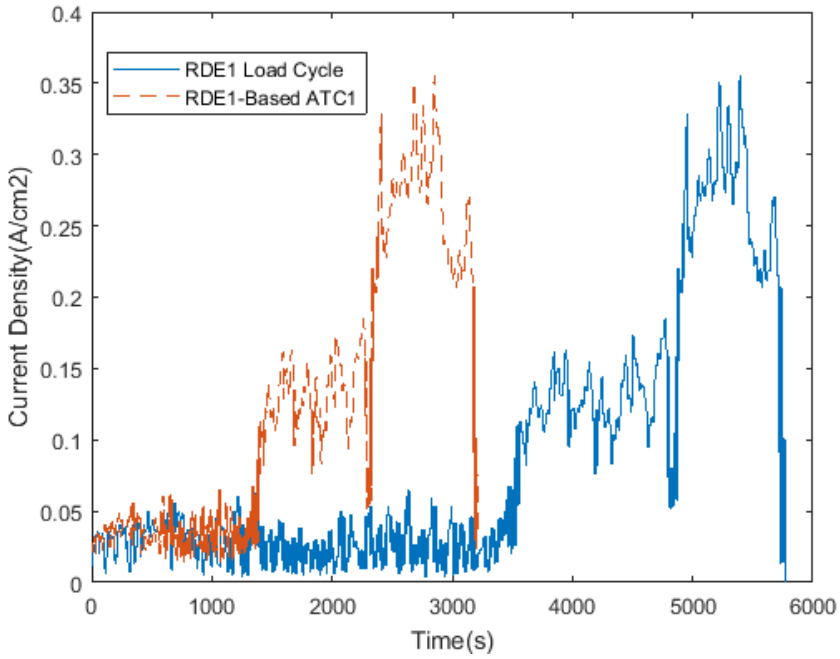

Figure 5.13 – RDE load cycle 1 based accelerated test cycle 1 and comparison

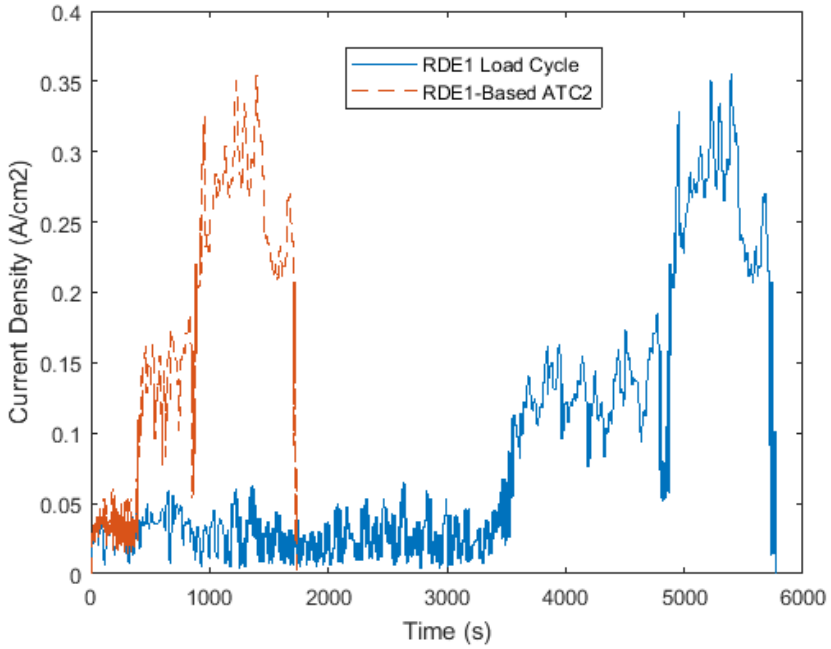

Figure 5.14 – RDE load cycle 1 based accelerated test cycle 2 and comparison

ATCs were also developed based on RDE load cycle 2 and 3 using the two different selection criteria and compared to their corresponding original RDE load profiles. As presented in Figure 5.15, RDE2-ATC1 was developed by selecting the time steps for which the degradation rates were higher than the average value, and the duration was reduced by 48.5%, from 8380s to 4317s. RD2-ATC2 was developed by selecting the time steps with top 30% highest degradation rates, and the duration was condensed from 8380s to 2514s, as presented in Figure 5.16.

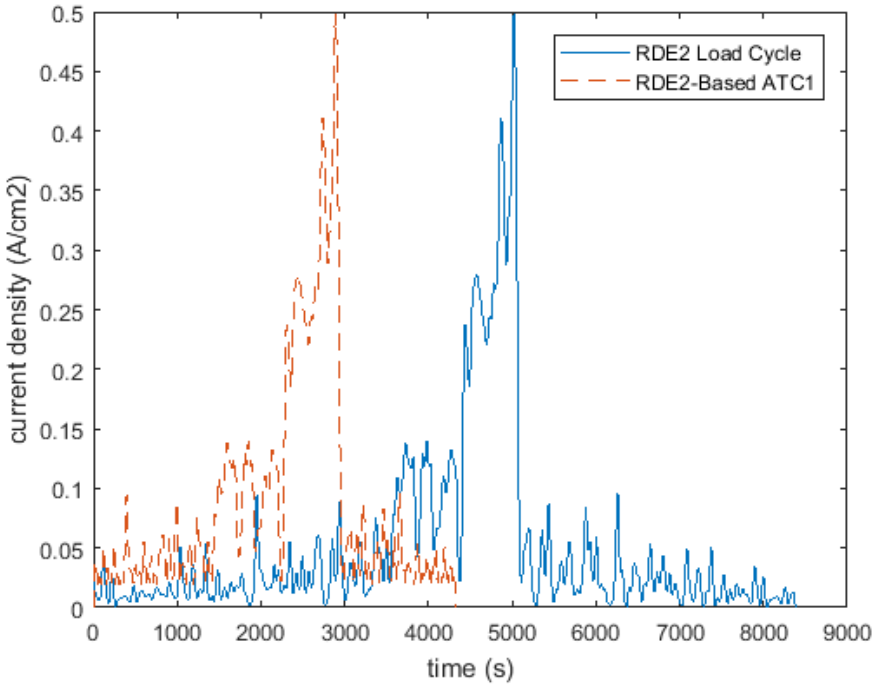

Figure 5.15 – RDE load cycle 2 based accelerated test cycle 1 and comparison

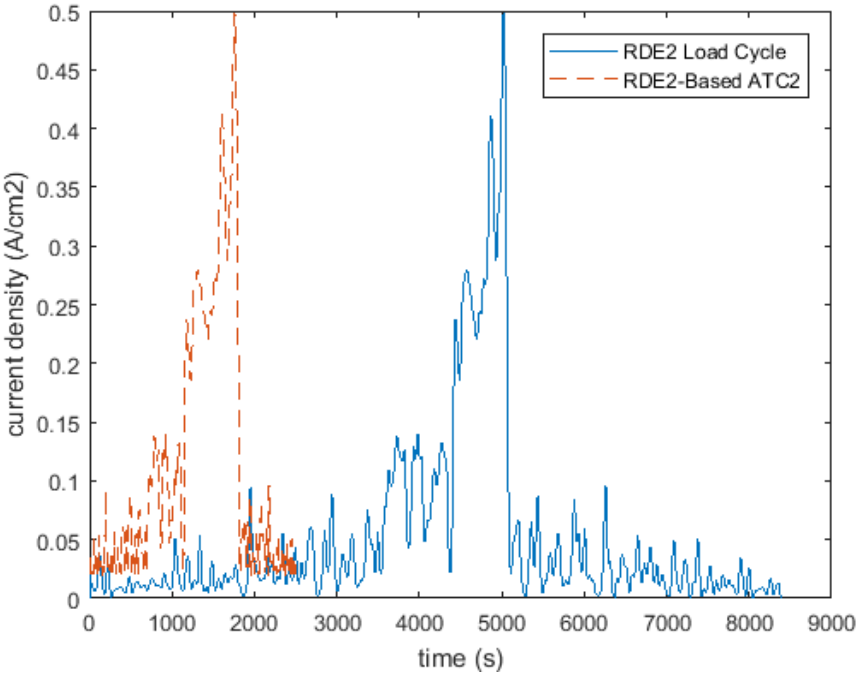

Figure 5.16 – RDE load cycle 2 based accelerated test cycle 1 and comparison

Figure 5.17 and Figure 5.18 compare RDE3-ATC1 and RDE3-ATC2 with RDE3 load cycle. By selecting the time steps with higher than average degradation rates, RDE3 load cycle was condensed by 39.8%, from 5488s to 3361s. By selecting the top 30% highest degradation rates the duration was further condensed to 1648s.

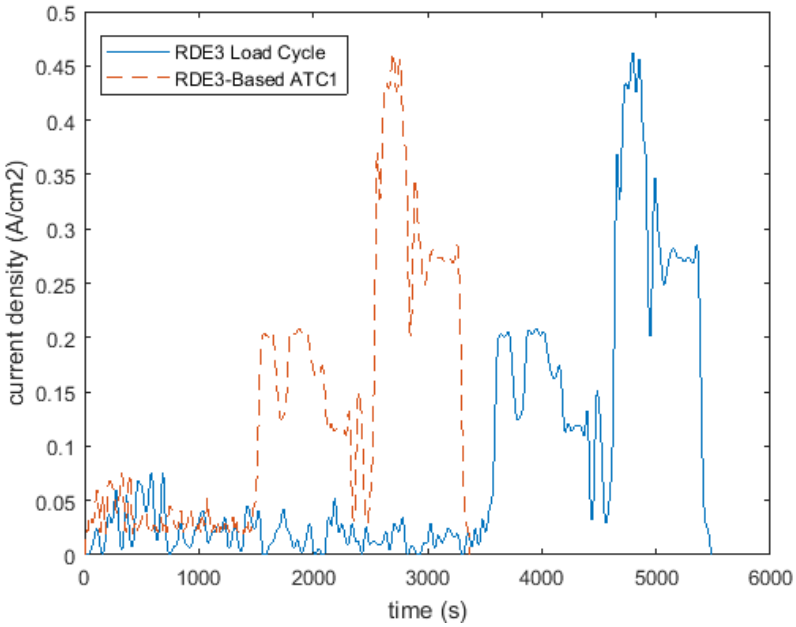

Figure 5.17 – RDE load cycle 3 based accelerated test cycle 1 and comparison

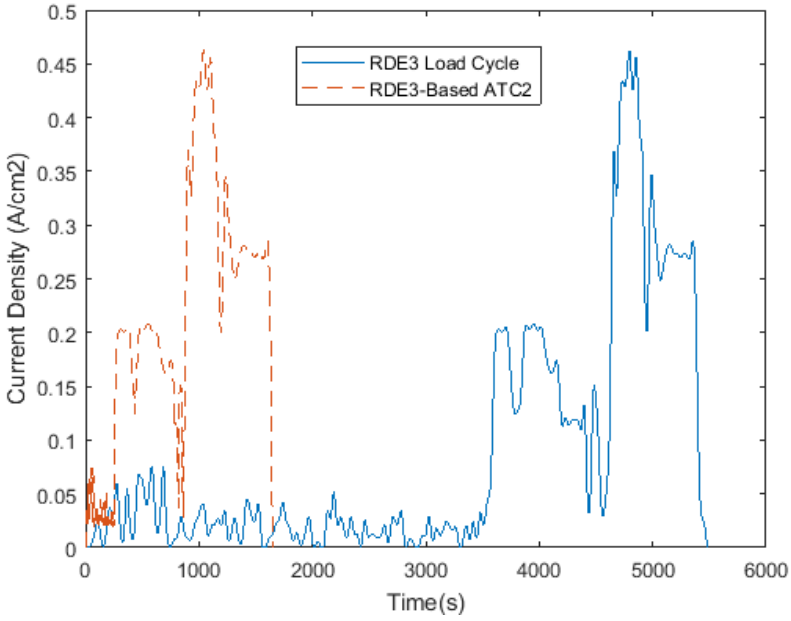

Figure 5.18 – RDE load cycle 3 based accelerated test cycle 2 and comparison

5.2.4 Degradation Voltage Prediction and Error Analysis

As introduced in Chapter 3.2.5, the degradation voltage of the original RDE load cycles can be predicted from the developed ATCs. Firstly, the acceleration factor (AF) of each ATC was calculated using equation (3.11) and equation (3.12). The degradation voltages remaining in the ATCs were calculated by integrating the selected degradation rates. The degradation voltage of the original RDE load cycles were obtained from the previous average value of the 100 simulations. By dividing the degradation voltage of the original RDEs by the corresponding degradation voltages remaining in the ATCs, the AF of each ATC was calculated, representing the ratio between the degradation voltage of the original RDE load cycles and that of the ATC. Table 5-3 contained the selection criteria, the acceleration factors, and the remained duration of the test cycles.

Table 5-3 – RDE based acceleration test cycles with various acceleration factors

	RDE1-ATC1	RDE1-ATC2	RDE2-ATC1	RDE2-ATC2	RDE3-ATC1	RDE3-ATC2	Unit
Selection Criteria	Higher than Average	Top 30% Highest	Higher than Average	Top 30% Highest	Higher than Average	Top 30% Highest	
AF	1.215	2.321	1.186	1.84	1.14	1.94	
Duration	54	29	72	42	56	28	Minutes

To predict the degradation voltage of the RDE load cycles using the developed ATCs, the ATCs were utilised as inputs to the model and simulations were run 100 times for each ATC. The degradation voltage of the 100 simulations were averaged out and regarded as the degradation voltage of the ATC. According to equation (3.13), the degradation voltage of the RDE load cycles can be predicted by multiplying the simulated degradation voltage of the ATCs by their corresponding AF. Errors were calculated as described in equation (3.14). The degradation voltage of the simulated ATCs, the AF, the predicted and simulated degradation voltage of the RDE load cycles, and the error of each prediction are presented in Table 5-4.

Table 5-4 – RDE based accelerated test cycles predictions and error

	RDE1-ATC1	RDE1-ATC2	RDE2-ATC1	RDE2-ATC2	RDE3-ATC1	RDE3-ATC2	Unit
AF	1.215	2.321	1.186	1.84	1.18	1.94	
Simulated ATC Degradation Voltage	1.57×10^{-4}	1.04×10^{-4}	1.78×10^{-4}	1.22×10^{-4}	1.59×10^{-4}	9.95×10^{-5}	V
Predicted RDE Degradation Voltage	2.22×10^{-4}	2.41×10^{-4}	2.11×10^{-4}	2.24×10^{-4}	1.81×10^{-4}	1.93×10^{-4}	V
Simulated RDE Degradation Voltage	1.91×10^{-4}	1.91×10^{-4}	1.89×10^{-4}	1.89×10^{-4}	1.59×10^{-4}	1.59×10^{-4}	V
Error	16.1	26.2	11.6	18.5	11.9	21.3	%

The errors in Table 5-4 were plotted in Figure 5.19 and it can be concluded that the errors showed the same trend as that in Chapter 4.3. For the same RDE load cycle, the error increased with the increasing AF, which means that the further the cycle was condensed, the larger the AF and the less degradation information remained in the ATC. This resulted in a developed ATC and AF with lower accuracy.

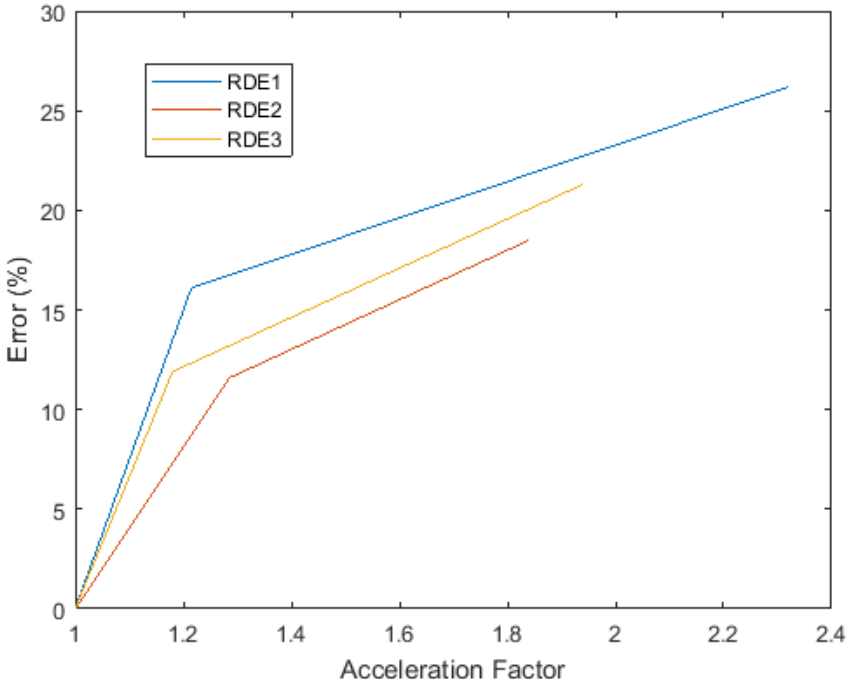

Figure 5.19 – Error curves of RDE load cycles degradation voltage predictions

If the acceleration factors of the developed test cycles were the same, the error of using the test cycle to predict the degradation voltage loss of the original cycles showed a decreasing trend from RDE1 to RDE2 and to RDE3. As presented in Table 5-1, the number of load increase and decrease and the maximum load change rate decreased from RDE1 to RDE2 and further to RDE3 load cycle, while the average current density output decreased from RDE1 to RDE2 but increased from RDE 2 to RDE3. The error did not follow the same trend with the transit nature. The possible reason was that the three factors chosen to represent the transit nature of a load cycle varied following different trends from RDE2 to RDE3, and therefore, it is difficult to accurately compare the transit nature of RDE2 and RDE3. However, by comparing RDE1 with RDE2 and RDE3 respectively, the error decreased with the less rapid transit nature of the RDE cycles.

5.3 Conclusions

To conclude this chapter, the developed ATC development strategy was applied to RDE drive cycles to predict the degradation voltage loss. The aim is to prove that the strategy can not only be applied to long-term laboratory operations to reduce durability testing time, but also can be used to predict the degradation voltage loss of dynamic real-world applications. Each of the three chosen RDE testing drive cycles were condensed into two ATCs with

different AFs, and predictions of the degradation voltage loss of the RDE testing drive cycles were made using the ATCs. By using the ATCs, the degradation voltage of all the three RDE testing drive cycles were predicted successfully and compared with simulated results. The error of using RDE1-based ATCs, the acceleration factor of which were 2.32 and 1.22, were 26% and 16%. The error of using RDE2-based ATCs, the acceleration factor of which were 1.84 and 1.192, were 19% and 12%. The error of using RDE3-based ATCs, the acceleration factor of which were 1.94 and 1.18, were 22% and 12%. The error proved that the developed ATC development strategy can predict the degradation voltage of the RDE testing drive cycles with a reasonable error. This error increased with increasing AF and increasing transient nature of the RDE testing drive cycles.

Chapter 6

6 Combining Accelerated Stress Test with ATC Development Strategy

6.1 Introduction

As introduced in Chapter 1.4, at present, one of the most widely used durability test strategies employed by researcher is accelerated stress tests, which involves increasing stress level to facilitate the degradation and failure of a product to obtain durability in limited testing time. Stress level can be increased by increasing usage rate, reducing off time, and increasing operating parameters, such as speed, temperature, voltage, etc. [159]. According to different designed service of the product, stress loading under accelerated conditions can be applied in various ways, such as constant-stress, step-stress, progressive-stress, cyclic-stress, random-stress, or a combination of those loading [126].

According to the nature of a product, two types of accelerated stress tests, which are accelerated life tests (ALT) and accelerated degradation tests (ADT), have been employed by researchers and engineers. In an ALT, a product will be operated at accelerated conditions until physical failure occurs, while the ADT is more suitable for highly reliable products, because for those products no physical failure will occur, and only limited amount of degradation will be observed even after accelerated stress tests. The physical failure in an ALT is called hard or catastrophic failure, and the failure in an ADT is called soft failure [160]. Because this research is targeted on the durability of long-term PEMFCs operations rather than the reliability, more attention has been paid to ADT because the failure was defined as when the cell performance decreased by 5%, rather than hard failure occurs.

The life data or degradation data obtained from accelerated stress tests will be analysed using statistical models to describe the relationship between stress level and lifetime. Typical accelerated stress tests utilise two statistical models, which are lifetime distribution and life-stress relationship.

6.1.1 A Product's Lifetime Distribution

A lifetime distribution represents the variation in product lifetime of different specimens. Many researchers utilise Weibull distribution to describe the scatter of PEMFC lifetime [99] [100] [101].

Weibull Distribution

The population fraction failing by age t is

$$F(t) = 1 - \exp\left[-\left(\frac{t}{\alpha}\right)^{\beta}\right], t > 0, \tag{6.1}$$

Where α and β are scale parameter and shape parameter, respectively, and both are positive.

The probability density function is

$$f(t) = \left(\frac{\beta}{\alpha^{\beta}}\right) t^{\beta-1} \exp\left[-\left(\frac{t}{\alpha}\right)^{\beta}\right], t > 0, \tag{6.2}$$

representing the probability of product failing at the time t. The point where the probability of failure reaches the maximum does not represent the actual lifetime of a product.

The 100pth percentile is

$$\xi_p = \alpha[-\log(1-p)]^{\frac{1}{\beta}}, \tag{6.3}$$

Where the base of log is e, and the 63.2th percentile of the distribution is the characteristic life of the distribution.

Figure 6.1 presents a typical Weibull probability density function, where $\alpha = 1000$ and $\beta = 4$.

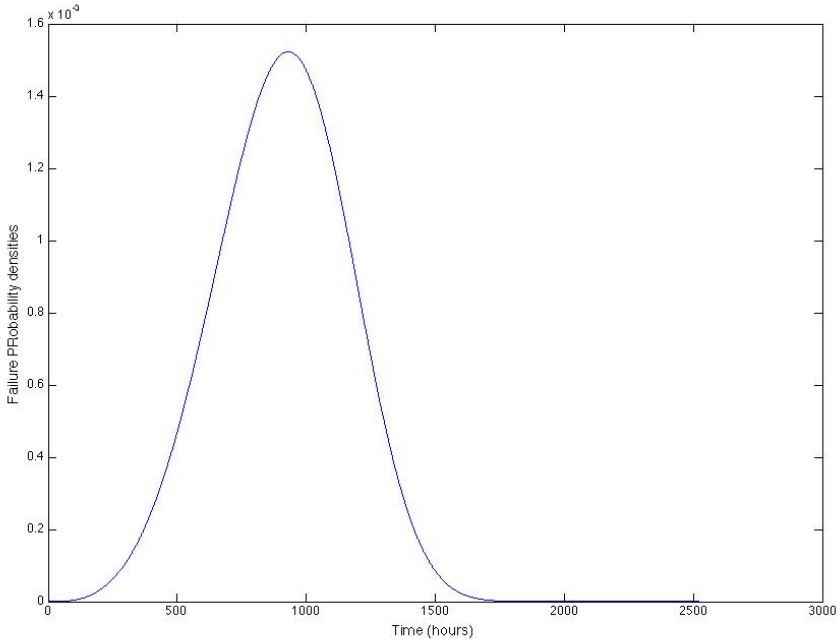

Figure 6.1 – A typical probability density function of a Weibull distribution

6.1.2 Life-Stress Relationship

A life-stress relationship describes the relationship between lifetime of the product and the stress level. After obtaining the lifetime distribution of the product at a stress level, each data point in the distribution can be mapped to its corresponding point at another stress level using life-stress relationship. Figure 6.2 presents an illustration of mapping a life distribution at a stress level to other stress levels using a life-stress relationship.

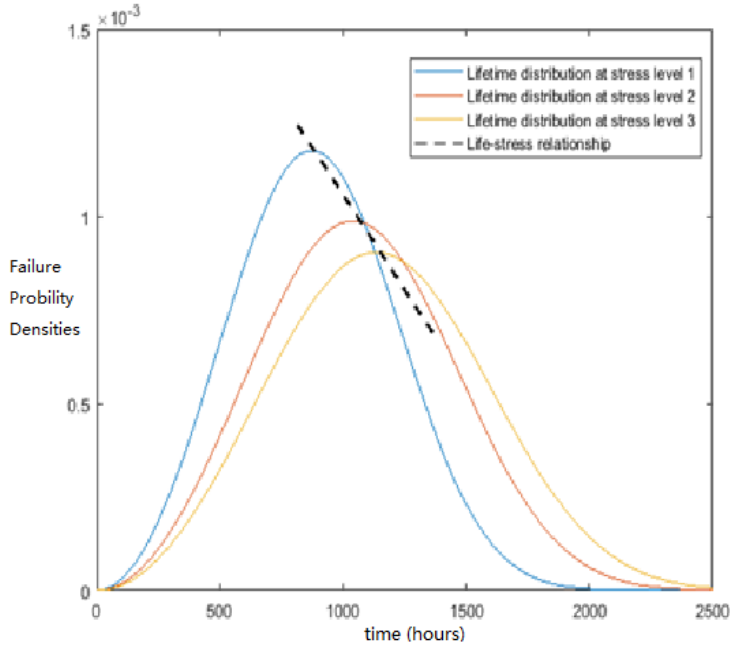

Figure 6.2 – Using life-stress relationship to predict lifetime distribution at different stress levels

The three curves are lifetime distributions at different stress levels, and the dashed line represents the life-stress relationship. The lifetime distribution at stress level 3 was predicted from that at stress level 1 and 2 using the life-stress relationship. By using the three distributions together with the life-stress relationship, the life distribution at any stress level can be predicted.

Arrhenius relationship

A life-stress relationship can be expressed in various forms. Statistical models were widely used by researchers to describe life-stress relationship and the accuracy has been proved. The most commonly used statistical model relationships are: Arrhenius, inverse power law, Eyring, and multivariable, etc. The Arrhenius relationship is used when the degradation is temperature sensitive and the life of a product is a function of temperature [159] [160].

The Arrhenius relationship is shown in equation (6.4), describing the nominal time to failure as a function of temperature.

$$\tau = A \exp\left(\frac{E}{kT}\right) \tag{6.4}$$

Where τ is the time to failure, E is the activation energy of the reaction, usually in electron-volts, k is Boltzmann's constant, 8.6171 x 10^{-5} electron-volts per °C, T is the absolute Kelvin temperature, and A is a constant depends on the product nature and testing method.

The Arrhenius relationship can be linearised by obtaining the (base 10) logarithm of nominal time to failure, as described in equation (6.5).

$$\log(\tau) = \gamma_0 + (\frac{\gamma_1}{T}) \tag{6.5}$$

where

$$\gamma_1 = \log(e)\left(\frac{E}{k}\right) \approx 0.4343\ \frac{E}{k} \tag{6.6}$$

By using equation (7.7), the life τ at temperature T and life τ' at temperature T' can be linked using an Arrhenius acceleration factor F.

$$F = \frac{\tau}{\tau'} = \exp\left[\left(\frac{E}{k}\right)(\frac{1}{T} - \frac{1}{T'})\right] \tag{6.7}$$

The linearised Arrhenius relationship together with the Arrhenius acceleration factor will be utilised in this chapter to describe the relationship between life and different operating temperatures.

6.2 Combination of AST and ATC

To combine the developed ATC development strategy with AST, the operating cell temperature was selected as the stressor of the AST and changed from 60°C to 80°C and 100°C. The petri-nets model is capable of assessing the effects of different operating cell temperatures. Despite the fact that a standard analysis involves both the lifetime distribution of a product and the life-stress relationship, in this work, the analysis is purely based on simulations instead of experiments, in addition, it is the durability instead of the reliability that is the aim, only the life-stress relationship will be used in this chapter.

6.2.1 Predicted WLTP Durability at 60°C from 80°C and 100°C Using Life-Stress Relationship

As discussed in 7.1.2, the product life under different stress level can be described using a life-stress relationship, and for temperature acceleration, the Arrhenius relationship was widely used to model the life-stress relationship.

The simulation of operating a PEMFC under WLTP at 60°C, 80°C and 100°C were run for 100 times at each temperature, and the durability at each temperature was averaged out to be regarded as the durability at the operating temperature. The durability at 60°C, 80°C and 100°C were modelled as 1236 hours, 1066 hours and 1012 hours, respectively. The model is capable of simulating PEMFC operations and calculate degradation voltage loss at different temperatures because temperature is one of the inputs of the degradation mechanisms and the degradation rates varies based on different

operating temperatures. However, the accuracy of simulating the effects of temperature on degradation is expected to be lower compared with experiments undertaken at different temperatures. The difference is not quantified at this stage due to lack of experimental data.

According to Arrhenius Relationship, the lifetimes at different temperatures were expressed as

$$\tau_1 = A \exp\left(\frac{E}{kT_1}\right) \tag{6.8}$$

$$\tau_2 = A \exp\left(\frac{E}{kT_2}\right) \tag{6.9}$$

Where, $\tau_1 = 1236\ hours$, $T_1 = 333.15\ K$, $\tau_2 = 1068\ hours$, and $T_1 = 353.15\ K$.

By solving Equation (6.8) and (6.9), the A and E can be estimated. A=90.66 and E=0.075 eV. Both A and E were estimated from experimental results.

The Arrhenius relationship was linearised as described in Equation (6.5),

$$\log(\tau) = \gamma_0 + \left(\frac{\gamma_1}{T}\right)$$

where

$$\gamma_1 = \log(e)\left(\frac{E}{k}\right) \approx 0.4343\ \frac{E}{k} = 378 \tag{6.10}$$

$$\gamma_0 = \log(\tau) - \left(\frac{\gamma_1}{T}\right) = 5.985 \tag{6.11}$$

Therefore, the linearised Arrhenius relationship was expressed as:

$$\log(\tau) = 5.985 + \left(\frac{378}{T}\right) \tag{6.12}$$

The Arrhenius acceleration factor between 80°C and 60°C was calculated as:

$$F_{(80°C\text{ to }60°C)} = \frac{\tau_{60°C}}{\tau_{80°C}} = \exp\left[\left(\frac{E}{k}\right)\left(\frac{1}{T(60°C)} - \frac{1}{T(80°C)}\right)\right] = 1.19 \tag{6.13}$$

Therefore, the lifetime under WLTP load cycle at 60°C can be predicted from that at 80°C as described below:

$$\tau_{(60°C\text{ from }80°C)} = \tau_{80°C} \times F_{(80°C\text{ to }60°C)} = 1269\ hours \tag{6.14}$$

Similarly, the Arrhenius acceleration factor between 100°C and 60°C was calculated as:

$$F_{(100°C \text{ to } 60°C)} = \frac{\tau_{60°C}}{\tau_{100°C}} = \exp\left[\left(\frac{E}{k}\right)\left(\frac{1}{T(60°C)} - \frac{1}{T(100°C)}\right)\right] = 1.30 \quad (6.15)$$

The lifetime at 100°C was modelled as 1012 hours, and the lifetime under WLTP load cycle at 60°C predicted from that at 100°C was

$$\tau_{(60°C \text{ from } 100°C)} = \tau_{100°C} \times F_{(100°C \text{ to } 60°C)} = 1316\ hours \quad (6.16)$$

The modelled durability of operating a PEMFC under WLTP at 80°C and the predicted distribution at 60°C based on the 80°C distribution was compared with the modelled 60°C durability. The error was calculated as follow:

$$\sigma_{(60°C \text{ from } 80°C)} = \left(1 - \frac{\tau_{60°C}}{\tau_{(60°C \text{ from } 80°C)}}\right) \times 100\% = 2.67\% \quad (6.17)$$

The durability of operating a PEMFC at 100°C was modelled and that of operating it at 60°C was predicted, and the error was calculated as follow:

$$\sigma_{(60°C \text{ from } 100°C)} = \left(1 - \frac{\tau_{60°C}}{\tau_{(60°C \text{ from } 100°C)}}\right) \times 100\% = 6.47\% \quad (6.18)$$

In this section, the durability of operating a PEMFC at 60°C were obtained from model calculation, from prediction based on 80°C and 100°C results, respectively. The feasibility of using the results obtained at higher temperature to predict the durability under a dynamic operation at a lower temperature level has been proved. The error showed an increasing trend with the increasing temperature. The load cycle used in this section remained unchanged, and only temperature was used as an accelerated stressor.

6.2.2 Predicted WLTP Durability at 60°C Using WLTP-Based ATCs at 80°C and 100°C.

In this section, to combine the ATC development strategy with the AST, the developed ATCs will be utilised at higher temperature to predict the durability of the WLTP load cycle at lower temperature level.

The durability of a PEMFC operating at 60°C under the ATCW1 developed in Chapter 3.2.4 was obtained and was compared with that under the WLTP load cycle. As calculated in Chapter 3.2.4, the acceleration factor of ATCW1 was 1.74. The durability of operating a PEMFC at 60°C under ATCW1 was estimated to be 493 hours simulated from the model in Chapter 3.2.4.

By following the steps described in the previous section, the ATCW1 was modelled at 60°C, 80°C, and 100°C, and the lifetime at each temperature was obtained. The simulation at each temperature was also repeated for 100 times and the average durability was utilised as the lifetime at that temperature. The

modelled durability of operating a PEMFC under ATCW1 at 60°C, 80°C, and 100°C was 493 hours, 396 hours, and 359 hours, respectively.

According to Arrhenius Relationship, E and A were calculated based on the temperature and durability of operating ATCW1, and the value of E and A were 0.13(eV) and 5.34, respectively.

The linearised Arrhenius relationship was

$$\log(\tau) = \gamma_0 + (\frac{\gamma_1}{T})$$

where

$$\gamma_1 = \log(e)\left(\frac{E}{k}\right) \approx 0.4343\ \frac{E}{k} = 655 \tag{6.19}$$

$$\gamma_0 = \log(\tau) - \left(\frac{\gamma_1}{T}\right) = 4.234 \tag{6.20}$$

Therefore, the linearised Arrhenius relationship for ATCW1 was:

$$\log(\tau) = 4.234 + (\frac{655}{T}) \tag{6.21}$$

The Arrhenius acceleration factor between operating under ATCW1 at 80°C and 60°C was

$$F_{(ATCW1-80°C\text{ to }60°C)} = \frac{\tau_{60°C}}{\tau_{80°C}} = \exp\left[\left(\frac{E}{k}\right)\left(\frac{1}{T(60°C)} - \frac{1}{T(80°C)}\right)\right] = 1.35 \tag{6.22}$$

Therefore, the lifetime under ATCW1 at 60°C was predicted from that at 80°C as described below:

$$\tau_{(ATCW1-60°C\text{ from }80°C)} = \tau_{80°C} \times F_{(ATCW1-80°C\text{ to }60°C)} = 535\ hours \tag{6.23}$$

Similarly, the Arrhenius acceleration factor between operating under ATCW1 at 100°C and 60°C was

$$F_{(ATCW1-100°C\text{ to }60°C)} = \frac{\tau_{60°C}}{\tau_{100°C}} = \exp\left[\left(\frac{E}{k}\right)\left(\frac{1}{T(60°C)} - \frac{1}{T(100°C)}\right)\right] = 1.57 \tag{7.24}$$

and the lifetime under ATCW1 at 60°C predicted from that at 100°C was

$$\tau_{(ATCW1-60°C\text{ from }100°C)} = \tau_{100°C} \times F_{(ATCW1-100°C\text{ to }60°C)} = 563\ hours \tag{6.25}$$

The calculation of the error of using the modelled ATCW1 operation at 80°C and 100°C to predict the durability of operating ATCW1 at 60°C was presented below.

$$\sigma_{(ATCW1-60°C\text{ from }80°C)} = \left(1 - \frac{\tau_{60°C}}{\tau_{(ATCW1-60°C\text{ from }80°C)}}\right) \times 100\% = 8.52\% \tag{6.26}$$

$$\sigma_{(ATCW1-60°C \text{ from } 100°C)} = \left(1 - \frac{\tau_{60°C}}{\tau_{(ATCW1-60°C \text{ from } 100°C)}}\right) \times 100\% = 14.20\% \quad (6.27)$$

The durability testing duration can be further reduced by combining the AST with the developed ATC strategy. This involves two steps, and the first step is to reduce the experimental testing duration by applying AST to operate the test cell at higher temperature level, as described in the flow chart in Figure 6.3. ATC failure voltage was defined as the degradation voltage remained in the ATC, calculated by integrating the selected degradation rates. Error1 represents the accuracy of representing the degradation level at the EOL at 60°C by that at 80°C.

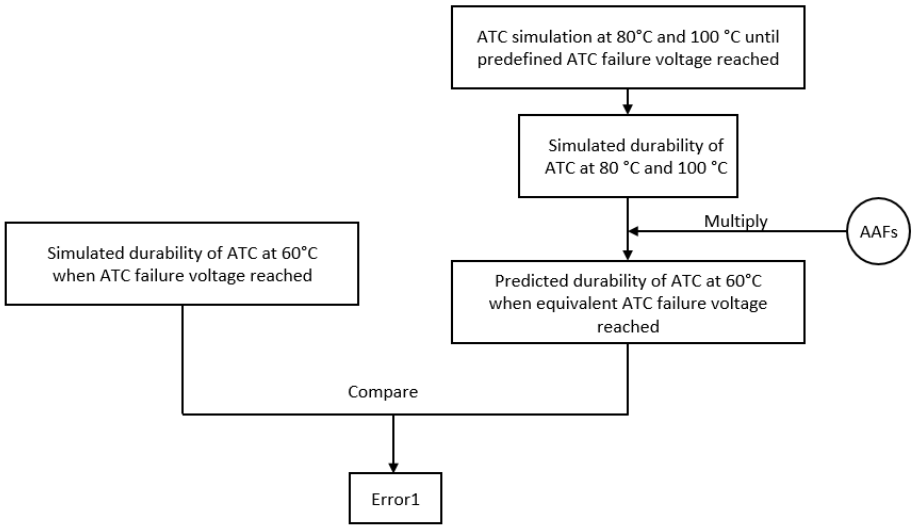

Figure 6.3 – Flow diagram of testing ATCs at accelerated stress level

The second step involves predicting the degradation voltage of the ATC-represented WLTP. As presented in Figure 6.4, error 2 represented the accuracy of using the ATC experimental results to predict the degradation voltage of the equivalent WLTP.

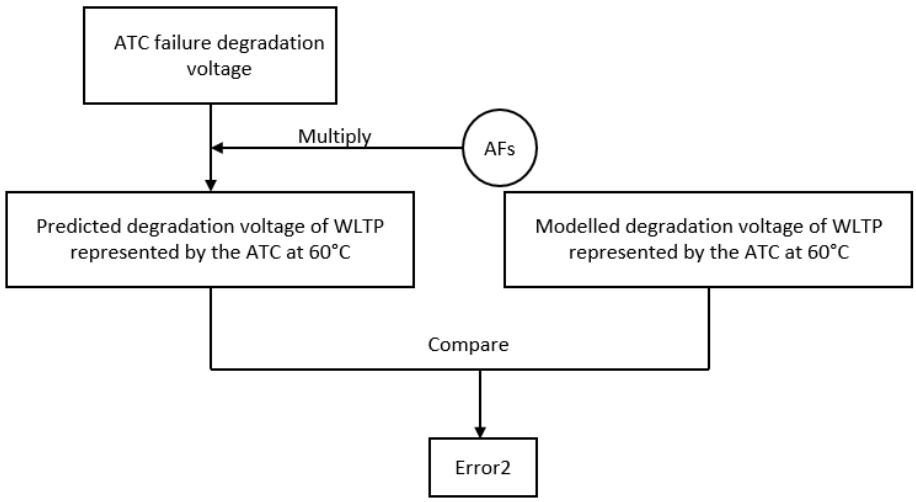

Figure 6.4 – Flow diagram of predicting the degradation voltage loss of WLTP using the acceleration factor of the accelerated test cycle

Therefore, the accuracy of the entire strategy of combining AST with ATC is the product of accuracy of step 1 and the accuracy of step 2. The overall error was calculated as:

$$\partial_{Overall} = [1 - (1 - error\ 1) \times (1 - error2)] \times 100\% \quad (6.28)$$

Error 2 was 8.2%, which represented the error of using ATCW1 to predict the equivalent WLTP degradation voltage and had been calculated in Chapter 3.2.5. Therefore,

$$\partial_{Overall\ ATCW1-60°C\ \text{from}\ 80°C} = [1 - (1 - 8.52\%) \times (1 - 8.2\%)] \times 100\% = 16.02\% \quad (6.29)$$

$$\partial_{Overall\ ATCW1-60°C\ \text{from}\ 100°C} = [1 - (1 - 14.20\%) \times (1 - 8.2\%)] \times 100\% = 21.24\% \quad (6.30)$$

The strategy of combining AST with ATCW1 was also applied to other developed ATCs.

ATCW2 and ATCW3, the acceleration factor of which were 1.52 and 2.20, were firstly simulated at 60°C, 80°C and 100°C and results are presented in Table 6-1. The average simulated durability under ATCW2 and ATCW3 at 60°C were 618 hours and 371 hours, respectively. The average simulated durability under ATCW2 at 80°C and 100°C were 546 hours and 502 hours, and that under ATCW3 at 80°C and 100°C were 316 hours and 285 hours, respectively.

Table 6-1 – ATC simulation results at 60°C, 80°C, and 100°C

Accelerated Test Cycles	Acceleration Factor	Simulated Life at 60°C	Simulated Life at 80°C	Simulated Life at 100°C
ATCW2	1.52	618 hours	546 hours	502 hours
ATCW3	2.20	371 hours	316 hours	285 hours

By using the simulated durability, the linearised Arrhenius relationship for ATCW2 was estimated as:

$$\log(\tau) = 5.2348 + (\frac{397}{T}) \tag{6.31}$$

and that for ATCW3 was estimated as:

$$\log(\tau) = 3.8961 + (\frac{673}{T}) \tag{6.32}$$

The Arrhenius acceleration factor between operating under ATCW2 at 80°C and 60°C was

$$F_{(ATCW2-80°C \text{ to } 60°C)} = \frac{\tau_{ATCW2-60°C}}{\tau_{ATCW2-80°C}} = \exp\left[\left(\frac{E}{k}\right)\left(\frac{1}{T(60°C)} - \frac{1}{T(80°C)}\right)\right] = 1.2 \tag{6.33}$$

Therefore, the lifetime under ATCW2 at 60°C predicted from that at 80°C was as described below:

$$\tau_{(ATCW2-60°C \text{ from } 80°C)} = \tau_{ATCW2-80°C} \times F_{(ATCW2-80°C \text{ to } 60°C)} = 655\ hours \tag{6.34}$$

Similarly, the Arrhenius acceleration factor between operating under ATCW2 at 100°C and 60°C was

$$F_{(ATCW2-100°C \text{ to } 60°C)} = \frac{\tau_{ATCW2-60°C}}{\tau_{ATCW2-100°C}} = \exp\left[\left(\frac{E}{k}\right)\left(\frac{1}{T(60°C)} - \frac{1}{T(100°C)}\right)\right] = 1.32 \tag{6.35}$$

and the lifetime under ATCW2 at 60°C predicted from that at 100°C was

$$\tau_{(ATCW2-60°C \text{ from } 100°C)} = \tau_{ATCW2-100°C} \times F_{(ATCW2-100°C \text{ to } 60°C)} = 662\ hours \tag{6.36}$$

The calculation of the error of using the modelled ATCW2 operation at 80°C and 100°C to predict the durability of operating ATCW2 at 60°C was presented below.

$$\sigma_{(ATCW2-60°C \text{ from } 80°C)} = \left(1 - \frac{\tau_{ATCW2-60°C}}{\tau_{(ATCW2-60°C \text{ from } 80°C)}}\right) \times 100\% = 5.99\% \quad (6.37)$$

$$\sigma_{(ATCW2-60°C \text{ from } 100°C)} = \left(1 - \frac{\tau_{60°C}}{\tau_{(ATCW2-60°C \text{ from } 100°C)}}\right) \times 100\% = 7.12\% \quad (6.38)$$

The same calculation and predictions were made for ATCW3.

The Arrhenius acceleration factor between operating under ATCW3 at 80°C and 60°C was

$$F_{(ATCW3-80°C \text{ to } 60°C)} = \frac{\tau_{ATCW3-60°C}}{\tau_{ATCW3-80°C}} = \exp\left[\left(\frac{E}{k}\right)\left(\frac{1}{T(60°C)} - \frac{1}{T(80°C)}\right)\right] = 1.36 \quad (6.39)$$

Therefore, the lifetime under ATCW3 at 60°C predicted from that at 80°C was as described below:

$$\tau_{(ATCW3-60°C \text{ from } 80°C)} = \tau_{ATCW3-80°C} \times F_{(ATCW3-80°C \text{ to } 60°C)} = 430\ hours \quad (6.40)$$

The Arrhenius acceleration factor between operating under ATCW3 at 100°C and 60°C was

$$F_{(ATCW3-100°C \text{ to } 60°C)} = \frac{\tau_{ATCW3-60°C}}{\tau_{ATCW3-100°C}} = \exp\left[\left(\frac{E}{k}\right)\left(\frac{1}{T(60°C)} - \frac{1}{T(100°C)}\right)\right] = 1.59 \quad (6.41)$$

and the lifetime under ATCW3 at 60°C predicted from that at 100°C was

$$\tau_{(ATCW3-60°C \text{ from } 100°C)} = \tau_{ATCW3-100°C} \times F_{(ATCW3-100°C \text{ to } 60°C)} = 453 hours \quad (6.42)$$

The calculation of the error of using the modelled ATCW3 operation at 80°C and 100°C to predict the durability of operating ATCW3 at 60°C was presented below.

$$\sigma_{(ATCW3-60°C \text{ from } 80°C)} = \left(1 - \frac{\tau_{ATCW3-60°C}}{\tau_{(ATCW3-60°C \text{ from } 80°C)}}\right) \times 100\% = 15.90\% \quad (6.43)$$

$$\sigma_{(ATCW2-60°C \text{ from } 100°C)} = \left(1 - \frac{\tau_{60°C}}{\tau_{(ATCW2-60°C \text{ from } 100°C)}}\right) \times 100\% = 22.10\% \quad (6.44)$$

The error of using ATCW2 and ATCW3 to predict the degradation voltage of their equivalent WLTP cycles were 5.3% and 11.6%. Therefore, the overall error of testing ATCW2 and ATCW3 at 80°C and 100°C to predict the degradation voltage loss of their corresponding WLTP cycles at 60°C were calculated as follow:

$$\partial_{Overall\ ATCW2-60°C \text{ from } 80°C} = [1 - (1 - 5.99\%) \times (1 - 5.3\%)] \times 100\% = 10.97\% \quad (6.45)$$

$$\partial_{Overall\ ATCW2-60°C \text{ from } 100°C} = [1 - (1 - 7.12\%) \times (1 - 5.3\%)] \times 100\% = 12.04\% \quad (6.46)$$

$$\partial_{Overall\ ATCW3-60°C \text{ from } 80°C} = [1 - (1 - 15.9\%) \times (1 - 11.6\%)] \times 100\% = 25.66\% \quad (6.47)$$

$$\partial_{Overall\ ATCW3-60°C \text{ from } 100°C} = [1 - (1 - 22.10\%) \times (1 - 11.6\%)] \times 100\% = 31.14\% \quad (6.48)$$

A 3D plot was presented in Figure 6.5 to illustrate how the overall error changes with temperature and acceleration factor of the ATCs. At the same temperature level, the higher the acceleration factor, the larger the error, and by using the same ATC, the acceleration factor remained unchanged, the higher the operating temperature, the larger the error.

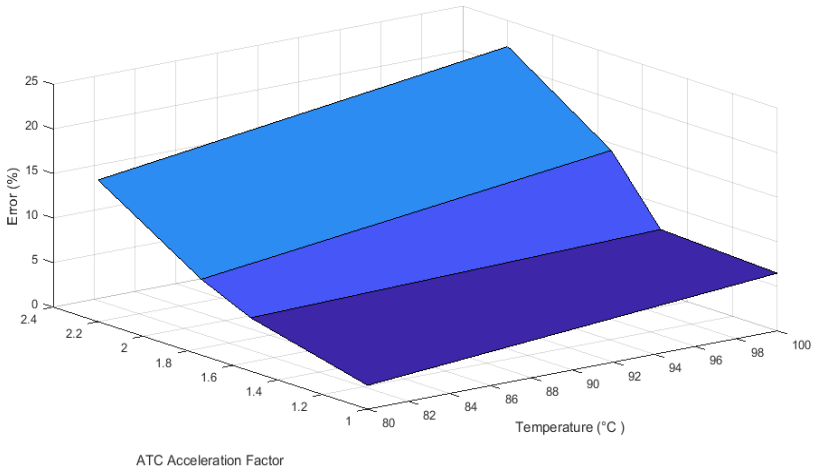

Figure 6.5 – Relationship between acceleration factor, temperature, and error

From the surface it can be concluded that the overall error of using the developed ATC operated at higher temperatures to predict the durability of the original WLTP cycles at normal usage temperature increased with increasing operating temperature and increasing ATC acceleration factors. In other words, with the increasing stress level (temperature) of the AST, and

with the increasingly condensed ATC, the prediction would be expected to be more inaccurate.

The right top point of the surface represents using ATCW3, the acceleration factor of which was 2.2, operating at 100°C to predict the durability of the equivalent WLTP cycle represented by ATCW3 operated at 60°C. The testing time to access durability was reduced by almost 77%, from 1236 hours to 285 hours, with an overall error of 31.14%.

6.3 Conclusion

In this chapter, the accelerated test cycle development strategy was combined with accelerated stress tests to seek the possibility of further reducing durability testing time. The developed WLTP-based accelerated test cycles were simulated at 80°C and 100°C until the calculated degradation voltage loss of the test cycles were reached, and the lifetime under each test cycle was obtained. The lifetime of each test cycle at 60°C was predicted using Arrhenius relationship. The accuracy of the above prediction was the difference between the predicted and the simulated lifetime at 60°C. The error of predicting WLTP degradation at 60°C from WLTP degradation at 80°C and 100°C were 3% and 6%. The error of predicting WLTP degradation at 60°C from ATC degradation at 80°C and 100°C were 9% and 14%. By multiplying the calculated degradation voltages loss of the test cycles by their corresponding acceleration factor, the degradation voltage loss under WLTP operation at 60°C can be predicted. The overall accuracy of this strategy is the product of the accuracy of the accelerated stress tests and that of using the test cycles to predict the degradation under WLTP operations. The overall error of testing ATCW1 at 80°C and 100°C to predict the degradation voltage loss of the WLTP at 60°C were 16% and 21% respectively. The overall error of testing ATCs of different acceleration factors at 80°C and 100°C to predict the degradation voltage loss of the WLTP at 60°C were 11% and 12% for ATCW2, and 26% and 31% for ATCW3, respectively.

Different from a standard accelerated stress test, which predicts the durability of an operation at design temperature by testing the operation at higher temperature level, this strategy firstly operates a condensed test cycle at higher temperature levels to reduce testing time of the test cycles. By multiplying the corresponding acceleration factor of the test cycle, the degradation voltage loss of the original operation can be predicted. Two acceleration factors were generated based on two factors, which are temperature and degradation voltage difference between the original operation and the test cycles, and therefore, the durability tests are accelerated twice.

Chapter 7

7 Conclusions and Future Work

7.1 Major Contributions

This work has contributed to the field of PEMFC durability measurement in the following aspects:

- A novel strategy that can condense prolonged dynamic real-world operations into accelerated test cycles with corresponding acceleration factors has been developed based on laboratory vehicle drive cycles. This fills the gap of using a condensed but intense cycle to represent a prolonged real-world application to measure the durability of PEMFCs.
- The feasibility of applying this strategy to real driving scenarios has been proven by developing RDE cycle-based accelerated test cycles. Degradation voltage losses of RDE cycles were successfully predicted.
- A two-dimension strategy was developed by combining accelerated stress tests with the accelerated test cycle development strategy, to further reduce durability testing time. This enables FC developers to conduct a test using a real life cycle based ATC at high temperature to predict life in the real life cycle at the intended temperature in a much reduced time.

7.2 Conclusions

The aim of this work is to develop a fast PEMFC durability test strategy that can condense dynamic real-world PEMFC applications into accelerated test cycles to reduce time and budget consumption of PEMFC durability tests. The aim has been achieved by accomplishing the following objectives.

- An understanding the operating principles and degradation mechanisms of PEM fuel cells was gained through a survey of literature.
- Advantages and limitations of the existing PEMFC durability test methods were identified from literature.
- Based on the literature review, a PEMFC performance and degradation model was found. This model is capable of calculating the second-by-second degradation voltage caused by a dynamic

PEMFC operation. The model was modified and adapted in this work to evaluate the degradation effects of each time step during an input load cycle.

- An accelerated test cycle was developed based on PEMFC WLTP operation. The degradation voltage loss of the 1236 hour WLTP operation was successfully predicted using the 493 hour test cycle and its acceleration factor. The durability testing time of the WLTP operation was reduced by over 60%, while the accuracy calculated from simulations was 92%.
- A test rig was built from the ground up and the accelerated test cycle development strategy was validated through experiments based on operation over 400 WLTP cycles. The 200-hour operation was condensed into 27 hours of tests and the predicted degradation voltage showed a strong agreement with that obtained from experiments, with an error of 16%.
- The sensitivity of the accelerated test cycle development strategy was analysed in terms of: the targeted real-world applications, the selection criteria applied, and the PEMFC performance and degradation model used to prove the universality of the strategy. Results showed that the accelerated test cycle development strategy can be applied to different real-world operations, and the accuracy decreased with: the more rapid transit nature of the targeted operations, the increasing acceleration factor of the test cycle, and the decreasing accuracy of the model used.
- The strategy was developed and validated using laboratory vehicle drive cycles and was applied to real driving emission tests cycles to prove it could be used in a real-world scenario. Accelerated test cycles were successfully produced based on three RDE cycles, and the degradation voltage loss of the three RDE cycles were all successfully predicted.
- The developed strategy was combined with accelerated stress tests to further reduce testing time. The WLTP-based accelerated test cycles were simulated at higher temperature levels until the calculated degradation voltage of the test cycles were reached, and lifetime at designed stress was mapped following the Arrhenius relationship. The degradation voltage loss of the WLTP operation was predicted by multiplying the degradation voltage loss of the test cycle by the acceleration factor. Accuracy of this combined strategy was the product of the accuracy of predicting the lifetime of the test cycle at designed temperature and that of predicting the degradation voltage loss of the WLTP operation using the test cycle. The testing time of 1236 hours WLTP operation was further reduced to 396 hours by

testing the developed 493 hours accelerated test cycle at 80°C and to 359 hours by testing it at 100°C.

7.3 Future Work

This work presents a novel strategy to condense a prolonged PEMFC operation, to reduce durability testing time. The degradation voltage loss of the original cycle has been successfully predicted using the developed accelerated test cycles. However, there still exists the possibility for improvement and expansion in the following aspects:

- The accuracy of the developed strategy has been validated, and the test cycles together with the acceleration factors were proven to be representative of the original operation in terms of overall degradation. However, the effects of condensing a prolonged operation into short test cycles on each individual degradation mechanism needs to be investigated further, and it would contribute to a better understanding of the relationship between load output and degradation phenomena.
- It has been proven that the accuracy of the model can affect the accuracy of the prediction. Although the Petri Nets model utilised in this work is reasonably accurate, it is possible to improve the accuracy of the model further.
- This ATC development strategy was focussed on developing accelerated test cycles for dynamic real-world operations. a method for reducing durability testing time of steady state PEMFC operations is still required.
- The ATC development strategy was integrated with accelerated stress tests to develop a two-dimension strategy. In this work, temperature was selected as the accelerated stressor to perform accelerated stress tests, and it is possible to add in other factors such as relative humidity and pressure to further condense the durability testing time. As discussed above, the effects of changing those factors on individual degradation mechanisms would be valuable to further understand degradation phenomena, and contribute to PEMFC modelling area in the future.
- The strategy was developed based on the output of an individual cell of a stack. Further work could expand the cell-level durability assessment into stack and system level degradation prediction by using a stack or system model combined with degradation model of each system component.
- It would be helpful to further understand the degradation phenomenon if the difference in degradation rates of different locations in stacks can be investigated.

- It would be valuable to demonstrate how valid this strategy is though big experiments data.

References

[1] DECC, “2011 UK GREENHOUSE GAS EMISSIONS, PROVISIONAL FIGURES,” 2012. [Online]. Available: https://assets.publishing.service.gov.uk/government/uploads/system/uploads/attachment_data/file/790626/2018-provisional-emissions-statistics-report.pdf. [Accessed: 09-May-2019].

[2] IEA, “Global Energy & CO2 Statuts Report,” 2018.

[3] G. J. Offer, D. Howey, M. Contestabile, R. Clague, and N. P. Brandon, “Comparative analysis of battery electric, hydrogen fuel cell and hybrid vehicles in a future sustainable road transport system,” *Energy Policy*, vol. 38, no. 1, pp. 24–29, Jan. 2010.

[4] HyWays, “The European Hydrogen Energy Roadmap,” Integrated Project co-funded by the EC under the 6th Framework Programme (Contract no.: SES6 502596), 2008.

[5] R. P. O’Hayre, S.-W. Cha, C. W. G., and P. F. B., “Fuel Cell Fundamentals, 2nd Ed.,” *John Wiley Sons*, 2009.

[6] J. Larminie and A. Dicks, “*Fuel Cell Systems Explained*”, vol. 93. 2001.

[7] S. Aso, M. Kizaki, and Y. Nonobe, “Development of fuel cell hybrid vehicles in TOYOTA,” in *Fourth Power Conversion Conference-NAGOYA, PCC-NAGOYA 2007 - Conference Proceedings*, 2007, vol. 16, no. 2, pp. 1606–1611.

[8] W. Sung, Y.-I. Song, K.-H. Yu, and T.-W. Lim, “Recent Advances in the Development of Hyundai · Kia’s Fuel Cell Electric Vehicles,” *SAE International Journal of Engines*, vol. 3. SAE International, pp. 768–772, 2010.

[9] Y. Sando, “Research and Development of Fuel Cell Vehicles at Honda,” in *ECS Transactions*, 2009, vol. 25, no. 1, pp. 211–224.

[10] M. P. Rodgers, L. J. Bonville, H. R. Kunz, D. K. Slattery, and J. M. Fenton, “Fuel Cell Perfluorinated Sulfonic Acid Membrane Degradation Correlating Accelerated Stress Testing and Lifetime,” *Chem. Rev.*, vol. 112, no. 11, pp. 6075–6103, Nov. 2012.

[11] R. Borup *et al.*, “Scientific aspects of polymer electrolyte fuel cell durability and degradation,” *Chemical Reviews*, vol. 107, no. 10. American Chemical Society, pp. 3904–3951, 2007.

[12] F. Barbir, *Pem Fuel Cells: Theory and Practice (2nd Edition)*. Academic Press, 2012.

[13] C.-Y. Wang, “Fundamental Models for Fuel Cell Engineering,” *Chem. Rev.*, vol. 104, no. 10, pp. 4727–4766, Oct. 2004.

[14] F. A. De Bruijn, V. A. T. Dam, and G. J. M. Janssen, “Review: Durability and degradation issues of PEM fuel cell components,” *Fuel Cells*, vol. 8, no. 1, pp. 3–22, Feb. 2008.

[15] S. P. Jiang, F. Wang, S. Peikang, M. Pan, and H. Tang, “A degradation study of Nafion proton exchange membrane of PEM fuel cells,” *Journal of Power Sources*, vol. 170, no. 1. pp. 85–92, 2007.

[16] Z. Luo, D. Li, H. Tang, M. Pan, and R. Ruan, “Degradation behavior of membrane-electrode-assembly materials in 10-cell PEMFC stack,” *Int. J. Hydrogen Energy*, vol. 31, no. 13, pp. 1831–1837, Oct. 2006.

[17] D. Moore *et al.*, “A polymer electrolyte fuel cell life test: 3 years of continuous operation,” *J. Power Sources*, vol. 158, no. 1, pp. 446–454, 2005.

[18] W. Chen *et al.*, “Test on the degradation of direct methanol fuel cell,” *Electrochim. Acta*, vol. 51, no. 12, pp. 2391–2399, 2006.

[19] A. Collier, H. Wang, X. Zi Yuan, J. Zhang, and D. P. Wilkinson, "Degradation of polymer electrolyte membranes," *Int. J. Hydrogen Energy*, vol. 31, no. 13, pp. 1838–1854, Oct. 2006.

[20] The US DOE Hydrogen and fuel cell plan, Washington, DC, 2010.

[21] W. Liu, K. Ruth, and G. Rusch, "Membrane Durability in PEM Fuel Cells," *J. New Mater. Electrochem. Syst.*, vol. 4, no. 4, pp. 227–232, 2001.

[22] S. Kundu, L. C. Simon, M. Fowler, and S. Grot, "Mechanical properties of Nafion^{TM} electrolyte membranes under hydrated conditions," *Polymer (Guildf).*, vol. 46, no. 25, pp. 11707–11715, Nov. 2005.

[23] M. Inaba, T. Kinumoto, M. Kiriake, R. Umebayashi, A. Tasaka, and Z. Ogumi, "Gas crossover and membrane degradation in polymer electrolyte fuel cells," *Electrochim. Acta*, vol. 51, no. 26, pp. 5746–5753, 2006.

[24] X. Cheng *et al.*, "Hydrogen crossover in high-temperature PEM fuel cells," *J. Power Sources*, vol. 167, no. 1, pp. 25–31, May 2007.

[25] F. N. Büchi, B. Gupta, O. Haas, and G. G. Scherer, "Study of radiation-grafted FEP-G-polystyrene membranes as polymer electrolytes in fuel cells," *Electrochim. Acta*, vol. 40, no. 3, pp. 345–353, Feb. 1995.

[26] H. Wang, "Behavior of Raipore Radiation-Grafted Polymer Membranes in H_2/O_2 Fuel Cells," *J. Electrochem. Soc.*, vol. 145, no. 3, p. 780, Mar. 2006.

[27] Handbook of fuel cell. Vol 3. Pp. 611.

[28] Handbook of fuel cell. Vol 3. Pp. 647.

[29] J. Healy *et al.*, "Aspects of the chemical degradation of PFSA ionomers used in PEM fuel cells x," *Fuel Cells*, vol. 5, no. 2. pp. 302–308, Apr-2005.

[30] F. D. Coms, "The Chemistry of Fuel Cell Membrane Chemical Degradation," in *ecst.ecsdl.org*, 2008, pp. 235–255.

[31] D. E. Curtin, R. D. Lousenberg, T. J. Henry, P. C. Tangeman, and M. E. Tisack, “Advanced materials for improved PEMFC performance and life,” *J. Power Sources*, vol. 131, no. 1–2, pp. 41–48, May 2004.
[32] M. Aoki, H. Uchida, and M. Watanabe, “Novel evaluation method for degradation rate of polymer electrolytes in fuel cells,” *Electrochem. commun.*, vol. 7, no. 12, pp. 1434–1438, 2005.
[33] V. O. Mittal, H. R. Kunz, and J. M. Fenton, “Effect of Catalyst Properties on Membrane Degradation Rate and the Underlying Degradation Mechanism in PEMFCs,” *J. Electrochem. Soc.*, vol. 153, no. 9, p. A1755, 2006.
[34] F. D. Coms, “The Chemistry of Fuel Cell Membrane Chemical Degradation,” in *ecst.ecsdl.org*, 2008, pp. 235–255.
[35] N. E. Cipollini, “Chemical Aspects of Membrane Degradation,” in *ecst.ecsdl.org*, 2007, pp. 1071–1082.
[36] S. Zhang, X. Z. Yuan, J. N. C. Hin, H. Wang, K. A. Friedrich, and M. Schulze, “A review of platinum-based catalyst layer degradation in proton exchange membrane fuel cells,” *Journal of Power Sources*, vol. 194, no. 2. pp. 588–600, 2009.
[37] R. L. Borup, J. R. Davey, F. H. Garzon, D. L. Wood, and M. A. Inbody, “PEM fuel cell electrocatalyst durability measurements,” *J. Power Sources*, vol. 163, no. 1 SPEC. ISS., pp. 76–81, 2006.
[38] E. Guilminot, A. Corcella, F. Charlot, F. Maillard, and M. Chatenet, “Detection of Pt z^+ Ions and Pt Nanoparticles Inside the Membrane of a Used PEMFC,” *J. Electrochem. Soc.*, vol. 154, no. 1, p. B96, 2006.
[39] K. More, R. Borup, and K. Reeves, “Identifying Contributing Degradation Phenomena in PEM Fuel Cell Membrane Electride Assemblies Via Electron Microscopy,” in *ECS Transactions*, 2006, vol. 3, pp. 717–733.
[40] M. Watanabe, “Activity and Stability of Ordered and Disordered Co-Pt Alloys for Phosphoric Acid Fuel Cells,” *J. Electrochem. Soc.*, vol. 141, no. 10, p. 2659, 2006.
[41] P. J. Ferreira *et al.*, “Instability of Pt/C Electrocatalysts in Proton Exchange Membrane Fuel Cells,” *J. Electrochem. Soc.*, vol. 152, no. 11, p. A2256, 2006.
[42] Y. Zhai, H. Zhang, D. Xing, and Z. G. Shao, “The stability of Pt/C catalyst in H3PO4/PBI PEMFC during high temperature life test,” *J. Power Sources*, vol. 164, no. 1, pp. 126–133, 2007.

[43] M. S. Wilson, “Surface Area Loss of Supported Platinum in Polymer Electrolyte Fuel Cells,” *J. Electrochem. Soc.*, vol. 140, no. 10, p. 2872, 2006.
[44] K. J. J. Mayrhofer *et al.*, “Fuel cell catalyst degradation on the nanoscale,” *Electrochem. commun.*, vol. 10, no. 8, pp. 1144–1147, 2008.
[45] R. M. Darling and J. P. Meyers, “Kinetic Model of Platinum Dissolution in PEMFCs,” *J. Electrochem. Soc.*, vol. 150, no. 11, p. A1523, 2003.
[46] J. Xie, D. L. Wood, K. L. More, P. Atanassov, and R. L. Borup, “Microstructural Changes of Membrane Electrode Assemblies during PEFC Durability Testing at High Humidity Conditions,” *J. Electrochem. Soc.*, vol. 152, no. 5, p. A1011, 2005.
[47] T. Akita *et al.*, “Analytical TEM study of Pt particle deposition in the proton-exchange membrane of a membrane-electrode-assembly,” *J. Power Sources*, vol. 159, no. 1 SPEC. ISS., pp. 461–467, 2006.
[48] J. Zhang, B. A. Litteer, W. Gu, H. Liu, and H. A. Gasteiger, “Effect of Hydrogen and Oxygen Partial Pressure on Pt Precipitation within the Membrane of PEMFCs,” *J. Electrochem. Soc.*, vol. 154, no. 10, p. B1006, 2007.
[49] D. K. Kinoshita, *Carbon: Electrochemical and Physicochemical Properties*. John Wiley Sons,New York, NY, 1988.
[50] J. Willsau and J. Heitbaum, “The influence of platinum activation on the corrosion of carbon in gas diffusion electrodes - a DEMS study.,” *Sect. Title Electrochem. Radiational, Therm. Energy Technol.*, vol. 161, no. 1, pp. 93–101, 1984.
[51] L. M. Roen, C. H. Paik, and T. D. Jarvi, “Electrocatalytic Corrosion of Carbon Support in PEMFC Cathodes,” *Electrochem. Solid-State Lett.*, vol. 7, no. 1, p. A19, Jan. 2003.
[52] M. Aoki, H. Uchida, and M. Watanabe, “Novel evaluation method for degradation rate of polymer electrolytes in fuel cells,” *Electrochem. commun.*, vol. 7, no. 12, pp. 1434–1438, Oct. 2005.
[53] J. Xie, D. L. Wood, D. M. Wayne, T. A. Zawodzinski, P. Atanassov, and R. L. Borup, “Durability of PEFCs at High Humidity Conditions,” *J. Electrochem. Soc.*, vol. 152, no. 1, p. A104, 2005.
[54] F. Y. Zhang, S. G. Advani, A. K. Prasad, M. E. Boggs, S. P. Sullivan, and T. P. Beebe, “Quantitative characterization of catalyst layer degradation in PEM fuel cells by X-ray photoelectron spectroscopy,” *Electrochim. Acta*, vol. 54, no. 16, pp. 4025–4030, 2009.

[55] M. Oszcipok, M. Zedda, D. Riemann, and D. Geckeler, “Low temperature operation and influence parameters on the cold start ability of portable PEMFCs,” *J. Power Sources*, vol. 154, no. 2, pp. 404–411, Mar. 2006.
[56] R. Mohtadi, W. K. Lee, and J. W. Van Zee, “Assessing durability of cathodes exposed to common air impurities,” *J. Power Sources*, vol. 138, no. 1–2, pp. 216–225, 2004.
[57] Y. Si, R. Jiang, J.-C. Lin, H. R. Kunz, and J. M. Fenton, “CO Tolerance of Carbon-Supported Platinum-Ruthenium Catalyst at Elevated Temperature and Atmospheric Pressure in a PEM Fuel Cell,” *J. Electrochem. Soc.*, vol. 151, no. 11, p. A1820, 2004.
[58] Z. Qi, C. He, and A. Kaufman, “Effect of CO in the anode fuel on the performance of PEM fuel cell cathode,” *J. Power Sources*, vol. 111, no. 2, pp. 239–247, 2002.
[59] F. Garzon, F. A. Uribe, T. Rockward, I. G. Urdampilleta, and E. L. Brosha, “The Impact of Hydrogen Fuel Contaminates on Long-Term PMFC Performance,” in *ECS Trans.*, 2006, vol. 3, no. 1, pp. 695–703.
[60] R. Borup, J. Davey, D. Wood, F. Garzon, M. Inbody, D. Guidry. “PEM fuel cell durability, ” DOE Hydrogen Program Review, Report No. FC40. 2005 May.
[61] R. Mukundan *et al.*, “Degradation of Gas Diffusion Layers in PEM Fuel Cells during Drive Cycle Operation,” *ECS Trans.*, vol. 58, no. 1, pp. 919–926, Aug. 2013.
[62] J. Wu *et al.*, “In situ accelerated degradation of gas diffusion layer in proton exchange membrane fuel cell. Part I: Effect of elevated temperature and flow rate,” *J. Power Sources*, vol. 195, no. 7, pp. 1888–1894, Apr. 2010.
[63] R. C. Makkus, A. H. Janssen, F. A. De Bruijn, and R. K. A. Mallant, “Use of stainless steel for cost competitive bipolar plates in the SPFC,” *J. Power Sources*, vol. 86, no. 1, pp. 274–282, Mar. 2000.
[64] A. Pozio, R. F. Silva, M. De Francesco, and L. Giorgi, “Nafion degradation in PEFCs from end plate iron contamination,” *Electrochim. Acta*, vol. 48, no. 11, pp. 1543–1549, May 2003.
[65] H. Wang, and J.A. Turner, “Reviewing metallic PEMFC bipolar plates,” Fuel cells 10.4, pp. 510-519, 2010.
[66] J. Tan, Y. J. Chao, M. Yang, W. K. Lee, and J. W. Van Zee, “Chemical and mechanical stability of a Silicone gasket material exposed to PEM fuel cell environment,” in *International Journal of Hydrogen Energy*, 2011, vol. 36, no. 2, pp. 1846–1852.

[67] G. Li, J. Tan, and J. Gong, “Degradation of the elastomeric gasket material in a simulated and four accelerated proton exchange membrane fuel cell environments,” *J. Power Sources*, vol. 205, pp. 244–251, May 2012.
[68] J. Tan, Y. J. Chao, M. Yang, C. T. Williams, and J. W. Van Zee, “Degradation characteristics of elastomeric gasket materials in a simulated PEM fuel cell environment,” *J. Mater. Eng. Perform.*, vol. 17, no. 6, pp. 785–792, Dec. 2008.
[69] J. Wu, X. Z. Yuan, H. Wang, M. Blanco, J. J. Martin, and J. Zhang, “Diagnostic tools in PEM fuel cell research: Part I Electrochemical techniques,” *International Journal of Hydrogen Energy*, vol. 33, no. 6. Pergamon, pp. 1735–1746, 01-Mar-2008.
[70] A. Parthasarathy, “The Platinum Microelectrode/Nafion Interface: An Electrochemical Impedance Spectroscopic Analysis of Oxygen Reduction Kinetics and Nafion Characteristics,” *J. Electrochem. Soc.*, vol. 139, no. 6, p. 1634, 2006.
[71] O. Antoine, Y. Bultel, and R. Durand, “Oxygen reduction reaction kinetics and mechanism on platinum nanoparticles inside Nafion®,” *J. Electroanal. Chem.*, vol. 499, no. 1, pp. 85–94, Feb. 2001.
[72] M. Eikerling and A. A. Kornyshev, “Electrochemical impedance of the cathode catalyst layer in polymer electrolyte fuel cells,” *J. Electroanal. Chem.*, vol. 475, no. 2, pp. 107–123, Oct. 1999.
[73] M. C. Lefebvre, “Characterization of Ionic Conductivity Profiles within Proton Exchange Membrane Fuel Cell Gas Diffusion Electrodes by Impedance Spectroscopy,” *Electrochem. Solid-State Lett.*, vol. 2, no. 6, p. 259, 2002.
[74] K. R. Cooper, V. Ramani, J. M. Fenton, and H. R. Kunz, “Experimental Methods and Data Analyses for Polymer Electrolyte Fuel Cells,” 2005.
[75] M. Ciureanu and R. Roberge, “Electrochemical impedance study of PEM fuel cells. Experimental diagnostics and modeling of air cathodes,” *J. Phys. Chem. B*, vol. 105, no. 17, pp. 3531–3539, May 2002.
[76] P. Kurzweil and H. J. Fischle, “A new monitoring method for electrochemical aggregates by impedance spectroscopy,” in *Journal of Power Sources*, 2004, vol. 127, no. 1–2, pp. 331–340.
[77] C. A. Schiller, F. Richter, E. Gülzow, and N. Wagner, “Relaxation impedance as a model for the deactivation mechanism of fuel cells due to carbon monoxide poisoning,” *Phys. Chem. Chem. Phys.*, vol. 3, no. 11, pp. 2113–2116, Jan. 2001.

[78] Y. J. Leng, X. Wang, and I. M. Hsing, “Assessment of CO-tolerance for different Pt-alloy anode catalysts in a polymer electrolyte fuel cell using ac impedance spectroscopy,” *J. Electroanal. Chem.*, vol. 528, no. 1–2, pp. 145–152, Jun. 2002.
[79] W. He, G. Lin, and T. Van Nguyen, “Diagnostic Tool to Detect Electrode Flooding in Proton-Exchange Membrane Fuel Cells,” *AIChE J.*, vol. 49, no. 12, pp. 3221–3228, 2003.
[80] M. M. Mench, Q. L. Dong, and C. Y. Wang, “In situ water distribution measurements in a polymer electrolyte fuel cell,” *J. Power Sources*, vol. 124, no. 1, pp. 90–98, Oct. 2003.
[81] S. Cleghorn, J. Kolde, and W. Liu, “Catalyst coated composite membranes,” in *Handbook of Fuel Cells*, vol. 3, Chichester, UK: John Wiley & Sons, Ltd, 2010, pp. 555–556.
[82] K. Borka and P. Ekdunge, “Oxygen and Hydrogen Permeation in Bulk and Recast Films,” *J. Appl. Electrochem.*, vol. 27, no. 2, pp. 117–123, 2013.
[83] D. U. Sauer and H. Wenzl, “Comparison of different approaches for lifetime prediction of electrochemical systems-Using lead-acid batteries as example,” *J. Power Sources*, vol. 176, no. 2, pp. 534–546, Feb. 2008.
[84] M. Marrony, R. Barrera, S. Quenet, S. Ginocchio, L. Montelatici, and A. Aslanides, “Durability study and lifetime prediction of baseline proton exchange membrane fuel cell under severe operating conditions,” *J. Power Sources*, vol. 182, no. 2, pp. 469–475, Aug. 2008.
[85] J. Lankford and S. J. Hudak, “Relevance of the small crack problem to lifetime prediction in gas turbines,” *Int. J. Fatigue*, vol. 9, no. 2, pp. 87–93, 1987.
[86] S. M. Meier, D. M. Nissley, K. D. Sheffler, and T. A. Cruse, “Thermal Barrier Coating Life Prediction Model Development,” in *Volume 5: Manufacturing Materials and Metallurgy; Ceramics; Structures and Dynamics; Controls, Diagnostics and Instrumentation; Education; IGTI Scholar Award; General*, 1991, p. V005T13A003.
[87] M. W. Fowler, R. F. Mann, J. C. Amphlett, B. A. Peppley, and P. R. Roberge, “Incorporation of voltage degradation into a generalised steady state electrochemical model for a PEM fuel cell,” *J. Power Sources*, vol. 106, no. 1–2, pp. 274–283, Apr. 2002.
[88] R. F. Mann, J. C. Amphlett, M. A. I. Hooper, H. M. Jensen, B. A. Peppley, and P. R. Roberge, “Development and application of a

generalized steady-state electrochemical model for a PEM fuel cell," *J. Power Sources*, vol. 86, no. 1, pp. 173–180, Mar. 2000.

[89] D. Liu and S. Case, "Durability study of proton exchange membrane fuel cells under dynamic testing conditions with cyclic current profile," *J. Power Sources*, vol. 162, no. 1, pp. 521–531, Nov. 2006.

[90] W. Bi and T. F. Fuller, "Modeling of PEM fuel cell Pt/C catalyst degradation," *J. Power Sources*, vol. 178, no. 1, pp. 188–196, Mar. 2008.

[91] R. Solasi, Y. Zou, X. Huang, K. Reifsnider, and D. Condit, "On mechanical behavior and in-plane modeling of constrained PEM fuel cell membranes subjected to hydration and temperature cycles," *J. Power Sources*, vol. 167, no. 2, pp. 366–377, May 2007.

[92] A. A. Shah, T. R. Ralph, and F. C. Walsh, "Modeling and Simulation of the Degradation of Perfluorinated Ion-Exchange Membranes in PEM Fuel Cells," *J. Electrochem. Soc.*, vol. 156, no. 4, p. B465, Apr. 2009.

[93] M. Whiteley, A. Fly, J. Leigh, S. Dunnett, and L. Jackson, "Advanced reliability analysis of Polymer Electrolyte Membrane Fuel Cells using Petri-Net analysis and fuel cell modelling techniques," in *International Journal of Hydrogen Energy*, 2015, vol. 40, no. 35, pp. 11550–11558.

[94] A. Fly, "Thermal and water management of evaporatively cooled fuel cell vehicles," Loughborough University, 2015.

[95] S. Zhang *et al.*, "A review of accelerated stress tests of MEA durability in PEM fuel cells," *International Journal of Hydrogen Energy*, vol. 34, no. 1. Pergamon, pp. 388–404, 01-Jan-2009.

[96] N. Ramaswamy, N. Hakim, and S. Mukerjee, "Degradation mechanism study of perfluorinated proton exchange membrane under fuel cell operating conditions," *Electrochim. Acta*, vol. 53, no. 8, pp. 3279–3295, Mar. 2008.

[97] M. Mathias and R. Makharia, "Two fuel cell cars in every garage?," *Electrochem. Soc. Interface*, vol. 14, pp. 24–35, 2005.

[98] D. Liu and S. Case, "Durability study of proton exchange membrane fuel cells under dynamic testing conditions with cyclic current profile," *J. Power Sources*, vol. 162, no. 1, pp. 521–531, Nov. 2006.

[99] E. Macarthur and W. Nelson, "Accelerated Testing: Statistical Models, Test Plans, and Data Analyses.," *Appl. Stat.*, vol. 41, no. 1, p. 224, 2006.

[100] S. J. Bae, S. J. Kim, J. I. Park, J. H. Lee, H. Cho, and J. Y. Park, "Lifetime prediction through accelerated degradation testing of

membrane electrode assemblies in direct methanol fuel cells," *Int. J. Hydrogen Energy*, vol. 35, no. 17, pp. 9166–9176, Sep. 2010.
[101] S. J. Bae *et al.*, "Lifetime prediction of a polymer electrolyte membrane fuel cell via an accelerated startup-shutdown cycle test," *Int. J. Hydrogen Energy*, vol. 37, no. 12, pp. 9775–9781, Jun. 2012.
[102] B. Li, R. Lin, D. Yang, and J. Ma, "Effect of driving cycle on the performance of PEM fuel cell and microstructure of membrane electrode assembly," *Int. J. Hydrogen Energy*, vol. 35, no. 7, pp. 2814–2819, Apr. 2010.
[103] R. Lin, B. Li, Y. P. Hou, and J. M. Ma, "Investigation of dynamic driving cycle effect on performance degradation and micro-structure change of PEM fuel cell," *Int. J. Hydrogen Energy*, vol. 34, no. 5, pp. 2369–2376, Mar. 2009.
[104] R. Lin, F. Xiong, W. C. Tang, L. Técher, J. M. Zhang, and J. X. Ma, "Investigation of dynamic driving cycle effect on the degradation of proton exchange membrane fuel cell by segmented cell technology," *J. Power Sources*, vol. 260, pp. 150–158, Aug. 2014.
[105] J. Shan, R. Lin, S. Xia, D. Liu, and Q. Zhang, "Local resolved investigation of PEMFC performance degradation mechanism during dynamic driving cycle," *Int. J. Hydrogen Energy*, vol. 41, no. 7, pp. 4239–4250, Feb. 2016.
[106] A. Bose, P. Babburi, R. Kumar, D. Myers, J. Mawdsley, and J. Milhuff, "Performance of individual cells in polymer electrolyte membrane fuel cell stack under-load cycling conditions," *J. Power Sources*, vol. 243, pp. 964–972, Dec. 2013.
[107] P. Pei, Q. Chang, and T. Tang, "A quick evaluating method for automotive fuel cell lifetime," *Int. J. Hydrogen Energy*, vol. 33, no. 14, pp. 3829–3836, Jul. 2008.
[108] B. Lakshmanan, W. Huang, D. Olmeijer, and J. W. Weidner, "Polyetheretherketone Membranes for Elevated Temperature PEMFCs," *Electrochem. Solid-State Lett.*, vol. 6, no. 12, p. A282, Dec. 2003.
[109] V. A. T. Dam and F. A. de Bruijn, "The Stability of PEMFC Electrodes," *J. Electrochem. Soc.*, vol. 154, no. 5, p. B494, May 2007.
[110] Y. Wang, "Analysis of the Key Parameters in the Cold Start of Polymer Electrolyte Fuel Cells," *J. Electrochem. Soc.*, vol. 154, no. 10, p. B1041, Oct. 2007.

[111] H. Xu *et al.*, “Durability of Nafion-Teflon-Phosphotungstic Acid Composite Membranes in PEM Fuel Cells at 100°C and 25%RH,” in *ECS Transactions*, 2006, vol. 3, no. 1, pp. 561–568.
[112] R. C. McDonald, C. K. Mittelsteadt, and E. L. Thompson, “Effects of deep temperature cycling on Nafion® 112 membranes and membrane electrode assemblies,” *Fuel Cells*, vol. 4, no. 3, pp. 208–213, Aug. 2004.
[113] V. A. Sethuraman, J. W. Weidner, A. T. Haug, and L. V. Protsailo, “Durability of Perfluorosulfonic Acid and Hydrocarbon Membranes: Effect of Humidity and Temperature,” *J. Electrochem. Soc.*, vol. 155, no. 2, p. B119, 2008.
[114] T. A. Zawodzinski, “Water Uptake by and Transport Through Nafion® 117 Membranes,” *J. Electrochem. Soc.*, vol. 140, no. 4, p. 1041, 2006.
[115] J. Yu, T. Matsuura, Y. Yoshikawa, M. N. Islam, and M. Hori, “In Situ Analysis of Performance Degradation of a PEMFC under Nonsaturated Humidification,” *Electrochem. Solid-State Lett.*, vol. 8, no. 3, p. A156, 2005.
[116] U. Beuscher, S. J. C. Cleghorn, and W. B. Johnson, “Challenges for PEM fuel cell membranes,” *Int. J. Energy Res.*, vol. 29, no. 12, pp. 1103–1112, Oct. 2005.
[117] P. Gode, G. Lindbergh, and G. Sundholm, “In-situ measurements of gas permeability in fuel cell membranes using a cylindrical microelectrode,” *J. Electroanal. Chem.*, vol. 518, no. 2, pp. 115–122, 2002.
[118] K. Broka, “Oxygen and hydrogen permeation properties and water uptake of Nafion® 117 membrane and recast film for PEM fuel cell,” *J. Appl. Electrochem.*, vol. 27, pp. 117–123, 1997.
[119] M. Aoki, H. Uchida, and M. Watanabe, “Decomposition mechanism of perfluorosulfonic acid electrolyte in polymer electrolyte fuel cells,” *Electrochem. commun.*, vol. 8, no. 9, pp. 1509–1513, 2006.
[120] H. Xu, R. Kunz, and J. M. Fenton, “Investigation of Platinum Oxidation in PEM Fuel Cells at Various Relative Humidities,” *Electrochem. Solid-State Lett.*, vol. 10, no. 1, p. B1, 2006.
[121] Shanna D. Knights, Kevin M. Colbow, Jean St-Pierre, and David P. Wilkinson, “Aging mechanisms and lifetime of PEFC and DMFC,” *J. Power Sources*, vol. 127, no. 1–2, pp. 127–134, 2004.
[122] J. Yu, T. Matsuura, Y. Yoshikawa, M. Nazrul Islam, and M. Hori, “Lifetime behavior of a PEM fuel cell with low humidification of feed stream,” *Phys. Chem. Chem. Phys.*, pp. 363–368, 2005.

[123] H. Xu, R. Boroup, E. Brosha, F. Gazon, and B. S. Pivovar, “Effect of Relative Humidity on Membrane Degradation Rate and Mechanism in PEM Fuel Cells,” in *ecst.ecsdl.org*, 2007, pp. 51–62.

[124] A. Kusoglu, A. M. Karlsson, M. H. Santare, S. Cleghorn, and W. B. Johnson, “Mechanical response of fuel cell membranes subjected to a hygro-thermal cycle,” *J. Power Sources*, vol. 161, no. 2, pp. 987–996, 2006.

[125] K. Yasuda, A. Taniguchi, T. Akita, T. Ioroi, and Z. Siroma, “Platinum dissolution and deposition in the polymer electrolyte membrane of a PEM fuel cell as studied by potential cycling,” *Phys. Chem. Chem. Phys.*, vol. 8, no. 6, pp. 746–752, 2006.

[126] F. Barbir *et al.*, “Comparison between two PEM fuel cell durability tests performed at constant current and under solicitations linked to transport mission profile,” *Int. J. Hydrogen Energy*, vol. 32, no. 17, pp. 4523–4536, 2007.

[127] F. Harel, X. François, D. Candusso, M. C. Péra, D. Hissel, and J. M. Kauffmann, “PEMFC durability test under specific dynamic current solicitation, Linked to a vehicle road cycle,” *Fuel Cells*, vol. 7, no. 2, pp. 142–152, Apr. 2007.

[128] V. A. T. Dam and F. A. de Bruijn, “The stability of PEMFC electrodes - Platinum dissolution vs potential and temperature investigated by quartz crystal microbalance,” *J. Electrochem. Soc.*, vol. 154, no. 5, pp. B494–B499, 2007.

[129] W. Bi, G. E. Gray, and T. F. Fuller, “PEM Fuel Cell Pt/C Dissolution and Deposition in Nafion Electrolyte,” *Electrochem. Solid-State Lett.*, vol. 10, no. 5, p. B101, 2007.

[130] P. J. Ferreira *et al.*, “Instability of Pt／C Electrocatalysts in Proton Exchange Membrane Fuel Cells A Mechanistic Investigation,” *J. Electrochem. Soc.*, vol. 152, no. 11, pp. A2256–A2271, 2005.

[131] A. Ohma, S. Suga, S. Yamamoto, and K. Shinohara, “Phenomenon Analysis of PEFC for Automotive Use (1) Membrane Degradation Behavior During OCV Hold Test,” in *ecst.ecsdl.org*, 2006, pp. 519–529.

[132] S. F. Burlatsky, V. Atrazhev, N. Cipollini, D. Condit, and N. Erikhman, “Aspects of PEMFC Degradation,” in *ECS Transactions*, 2006, vol. 1, no. 8, pp. 239–246.

[133] W. Liu and M. Crum, “Effective Testing Matrix for Studying Membrane Durability in PEM Fuel Cells: Part I. Chemical Durability,” in *ECS Transactions*, 2006, vol. 3, no. 1, pp. 531–540.

[134] T. Kinumoto *et al.*, “Durability of perfluorinated ionomer membrane against hydrogen peroxide,” *J. Power Sources*, vol. 158, no. 2 SPEC. ISS., pp. 1222–1228, 2006.
[135] A. Ohma, S. Suga, S. Yamamoto, and K. Shinohara, “Membrane Degradation Behavior during Open-Circuit Voltage Hold Test,” *J. Electrochem. Soc.*, vol. 154, no. 8, p. B757, 2007.
[136] R. Makharia *et al.*, “Durable PEM Fuel Cell Electrode Materials: Requirements and Benchmarking Methodologies,” in *ecst.ecsdl.org*, 2006, pp. 3–18.
[137] T. Fuller and G. Gray, “Carbon Corrosion Induced by Partial Hydrogen Coverage,” in *ecst.ecsdl.org*, 2006, pp. 345–353.
[138] H. Tang, Z. Qi, M. Ramani, and J. F. Elter, “PEM fuel cell cathode carbon corrosion due to the formation of air/fuel boundary at the anode,” *J. Power Sources*, vol. 158, no. 2 SPEC. ISS., pp. 1306–1312, 2006.
[139] C. A. Reiser *et al.*, “A Reverse-Current Decay Mechanism for Fuel Cells,” *Electrochem. Solid-State Lett.*, vol. 8, no. 6, p. A273, 2005.
[140] B. Du, Q. Guo, R. Pollard, D. Rodriguez, C. Smith, and J. Elter, “PEM fuel cells: Status and challenges for commercial stationary power applications,” *JOM*, vol. 58, no. 8. pp. 45–49, 2006.
[141] J. Wu *et al.*, “A review of PEM fuel cell durability: Degradation mechanisms and mitigation strategies,” *Journal of Power Sources*, vol. 184, no. 1. Elsevier, pp. 104–119, 15-Sep-2008.
[142] M. M. Mench, E. C. Kumbur, and T. N. Veziroglu, “*Polymer electrolyte fuel cell degradation,*” Academic Press, 2011.
[143] K. H. Lim, H. S. Oh, S. E. Jang, Y. J. Ko, H. J. Kim, and H. Kim, “Effect of operating conditions on carbon corrosion in polymer electrolyte membrane fuel cells,” *J. Power Sources*, vol. 193, no. 2, pp. 575–579, Sep. 2009.
[144] V. A. T. Dam and F. A. de Bruijn, “The Stability of PEMFC Electrodes,” *J. Electrochem. Soc.*, vol. 154, no. 5, p. B494, May 2007.
[145] W. Bi and T. F. Fuller, “Temperature Effects on PEM Fuel Cells Pt/C Catalyst Degradation,” *J. Electrochem. Soc.*, vol. 155, no. 2, p. B215, 2008.
[146] M. Inaba, T. Kinumoto, M. Kiriake, R. Umebayashi, A. Tasaka, and Z. Ogumi, “Gas crossover and membrane degradation in polymer electrolyte fuel cells,” *Electrochim. Acta*, vol. 51, no. 26, pp. 5746–5753, Aug. 2006.

[147] P. Mock, J. Kühlwein, U. Tietge, V. Franco, A. Bandivadekar, and J. German, “The WLTP: How a new test procedure for cars will affect fuel consumption values in the EU,” *International Council on Clean Transportation*, *9*, pp.35-47, 2014.

[148] A. Marotta, J. Pavlovic, B. Ciuffo, S. Serra, and G. Fontaras, “Gaseous Emissions from Light-Duty Vehicles: Moving from NEDC to the New WLTP Test Procedure,” *Environ. Sci. Technol.*, vol. 49, no. 14, pp. 8315–8322, Jul. 2015.

[149] J. Merkisz, M. Jacyna, A. Merkisz-Guranowska, and J. Pielecha, “The parameters of passenger cars engine in terms of real drive emission test,” Archives of Transport, 32, 2014.

[150] J. Borken-Kleefeld and Y. Chen, “Real-driving emissions from cars and light commercial vehicles - Results from 13 years remote sensing at Zurich/CH.,” *Atmos. Environ.*, vol. 88, pp. 157–164, 2014.

[151] B. Degraeuwe and M. Weiss, “Does the New European Driving Cycle (NEDC) really fail to capture the NO X emissions of diesel cars in Europe?,” *Environ. Pollut.*, vol. 222, pp. 234–241, Mar. 2017.

[152] M. Tutuianu *et al.*, “Development of the World-wide harmonized Light duty Test Cycle (WLTC) and a possible pathway for its introduction in the European legislation,” *Transp. Res. Part D Transp. Environ.*, vol. 40, pp. 61–75, Oct. 2015.

[153] G. Fontaras, V. Franco, P. Dilara, G. Martini, and U. Manfredi, “Development and review of Euro 5 passenger car emission factors based on experimental results over various driving cycles,” *Sci. Total Environ.*, vol. 468–469, pp. 1034–1042, Jan. 2014.

[154] N. Hooftman, M. Messagie, J. Van Mierlo, and T. Coosemans, “A review of the European passenger car regulations – Real driving emissions vs local air quality,” *Renewable and Sustainable Energy Reviews*, vol. 86. pp. 1–21, 2018.

[155] J. M. Luján, V. Bermúdez, V. Dolz, and J. Monsalve-Serrano, “An assessment of the real-world driving gaseous emissions from a Euro 6 light-duty diesel vehicle using a portable emissions measurement system (PEMS),” *Atmos. Environ.*, vol. 174, pp. 112–121, 2018.

[156] T. Donateo and M. Giovinazzi, “Building a cycle for Real Driving Emissions,” in *Energy Procedia*, 2017, vol. 126, pp. 891–898.

[157] T. Lee, J. Park, S. Kwon, J. Lee, and J. Kim, “Variability in operation-based NOx emission factors with different test routes, and its effects on the real-driving emissions of light diesel vehicles,” *Sci. Total Environ.*, vol. 461–462, pp. 377–385, Sep. 2013.

[158] J. M. Luján, V. Bermúdez, V. Dolz, and J. Monsalve-Serrano, “An assessment of the real-world driving gaseous emissions from a Euro 6 light-duty diesel vehicle using a portable emissions measurement system (PEMS),” *Atmos. Environ.*, vol. 174, pp. 112–121, Feb. 2018.
[159] E. Macarthur and W. Nelson, “Accelerated Testing: Statistical Models, Test Plans, and Data Analyses.,” *Appl. Stat.*, vol. 41, no. 1, p. 224, 2006.
[160] E. Kay, N. R. Mann, R. E. Schafer, and N. D. Singpurwalla, “Methods for Statistical Analysis of Reliability and Life Data,” *Oper. Res. Q.*, vol. 27, no. 2, p. 401, 2006.
[161] X. P. Wang, R. Kumar, and D. J. Myers, “Effect of voltage on platinum dissolution relevance to polymer electrolyte fuel cells,” *Electrochem. Solid State Lett.*, vol. 9, no. 5, pp. A225–A227, 2006.
M. Hu and G. Cao, “Research on the long-term stability of a PEMFC stack: Analysis of pinhole evolution,” *Int. J. Hydrogen Energy*, vol. 39, no. 15, pp. 7940–7954, 2014.

Appendix

Membrane Mechanical Degradation

Pinholes

```
function [Pinout,M0_Pinholes]  =
func( M0_Creep,M0_Peroxide,M0_Radical,M0_HighGCO,R_humidity_a,R_humi
dity_c )

R_humidity_tot = (R_humidity_a + R_humidity_c)/2;

Pinout = 0;

D_Pinholes= [-1 0 0 0 0 0 -1 1

             0 -1 0 0 0 0 1 0

             0 0 -1 0 0 0 1 0

             0 0 0 -1 0 0 1 0

             0 0 0 0 -1 0 1 0

             0 0 0 0 0 -1 1 0];

         M0_Pinholes=zeros(8,1);

         M0_Pinholes(1,1)=1;

         TPinholes=zeros(1,6);

if M0_Creep(1,8)+M0_Creep(1,9)+M0_Creep(1,10)~=0;

    M0_Pinholes(2,1) = 1;

end

if M0_Peroxide(1,8)==1;

    M0_Pinholes(3,1) = 1;

end

if M0_Radical(1,5)==1;

    M0_Pinholes(4,1) = 1;

end

if M0_HighGCO(1,4)==1;

    M0_Pinholes(5,1) = 1;

end
```

```
if R_humidity_tot <= 0.2;

    M0_Pinholes(6,1) = 1;

end

if R_humidity_tot > 0.2;

    M0_Pinholes(6,1) = 0;

End

if
M0_Pinholes(2,1)+M0_Pinholes(3,1)+M0_Pinholes(4,1)+M0_Pinholes(5,1)+
M0_Pinholes(6,1)~=0;

   TPinholes(1,1)=1;

   Mn=TPinholes*D_Pinholes+M0_Pinholes'

   M0_Pinholes = Mn';

end

if M0_Pinholes(8,1) == 1;

   Pinout=1;

end

end
```

Flooding

```
function [Floodout, M0_Flood]   = fcn(V_op, R_humidity_a,
R_humidity_c)

R_humidity_tot = (R_humidity_a + R_humidity_c)/2;

Floodout = 0;

ATFlood = [  -1;

            1];

        M0_Flood = zeros(2,1);

        M0_Flood(1,1) = 1;

        TFlood = zeros(1,1);

if M0_Flood(1,1) == 1 && R_humidity_tot >= 1.0;

    TFlood(1,1) = 1;

    Mn = M0_Flood+ATFlood*TFlood;

    M0_Flood = Mn;

end
```

```
if M0_Flood(2,1) == 1;

    Floodout = 1;

end

end
```

Creep

```
function [Creepout, M0_Creep]   = func( t, T_cell, R_humidity_a,
R_humidity_c)

Creepout=0;

D_Creep=[-1 0 0 1 0 0 0 0 0 0

         0 -1 -1 -1 0 -1 0 1 0 0

         0 0 0 -1 0 0 0 0 1 0

         0 -1 0 -1 -1 0 -1 0 0 1];

     M0_Creep=zeros(1,10);

     M0_Creep(1,1)=1;

if T_cell>358.15;

   M0_Creep(1,2)=1;

end

if R_humidity_a < 0.60 && R_humidity_c < 0.60;

    M0_Creep(1,3) = 1;

end

if R_humidity_a > 1.00 && R_humidity_c > 1.00;

    M0_Creep(1,5) = 1;

end

if t<6000;

    M0_Creep(1,6)=1;

end

if t>6000;

    M0_Creep(1,7)=1;

end

if M0_Creep(1,1)==1 && M0_Creep(1,2)==1 && M0_Creep(1,3)==1 &&
M0_Creep(1,6)==1;
```

```
    TCreep=zeros(1,4);

    TCreep(1,1)=1;

    TCreep(1,2)=1;

    TCreep(1,3)=1;

    Mn=TCreep*D_Creep+M0_Creep;

    M0_Creep=Mn;

end

if M0_Creep(1,1)==1 && M0_Creep(1,5)==1 && M0_Creep(1,2)==1 &&
M0_Creep(1,7)==1;

    TCreep=zeros(1,4);

    TCreep(1,1)=1;

    TCreep(1,3)=1;

    TCreep(1,4)=1;

    Mn=TCreep*D_Creep+M0_Creep;

    M0_Creep=Mn;

end

if M0_Creep(1,1)==1;

    TCreep=zeros(1,4);

    TCreep(1,1)=1;

    TCreep(1,3)=1;

    Mn=TCreep*D_Creep+M0_Creep;

    M0_Creep=Mn;

end

if M0_Creep(1,8) == 1;

    Creepout=1;

end

if M0_Creep(1,9) == 1;

    Creepout=1;

end

if M0_Creep(1,10) == 1;

    Creepout=1;
```

```
end
end
```

Swelling

```
function [ Swellingout, M0_Swelling ] = func( M0_Flood )
Swellingout=0;
D_Swelling= [0 -1 1 0
             -1 0 -1 1];
         M0_Swelling = zeros (1,4);
         M0_Swelling(1,1)=1;
         M0_Swelling(1,2)=M0_Flood(2,1);
         TSwelling=zeros(1,2);
if M0_Swelling(1,1)==1 && M0_Swelling(1,2)==1;
    TSwelling(1,1)=1;
    TSwelling(1,2)=1;
    Mn=TSwelling*D_Swelling+M0_Swelling;
    M0_Swelling=Mn;
end
if M0_Swelling(1,4)==1;
    Swellingout=1;
end
end
```

Membrane Chemical Degradation

Gas crossover

```
function [HGCOout,M0_HighGCO,M0_LowGCO]  = func( M0_Pinholes)
HGCOout=0;
D_HighGCO= [-1 1 0 0
             -1 0 -1 1];
M0_HighGCO = zeros(1,4);
M0_HighGCO(1,1) = 1;
THighGCO=zeros(1,2);
```

```
THighGCO(1,1)=1;

M0_HighGCO (1,3)=M0_Pinholes;

if M0_HighGCO (1,3)==1;

    THighGCO(1,2)=1;

    Mn=THighGCO*D_HighGCO+M0_HighGCO;

    M0_HighGCO=Mn;

end

M0_LowGCO=M0_HighGCO(1,2);

if M0_HighGCO(1,4)==1;

    HGCOout=1;

end

end
```

Peroxide Attack

```
function [Perout1, Perout2, Perout3, M0_Peroxide]   = fcn(V_op,
M0_BIP, M0_HighGCO,M0_LowGCO)

Perout1 = 0;

Perout2 = 0;

Perout3 = 0;

D_Peroxide = [ -1 0 0 0 0 0 -1 1

               0 -1 -1 0 0 -1 1 0

               0 0 -1 0 0 -1 1 0

               0 0 -1 -1 0 -1 1 0

               0 0 0 0 -1 -1 1 0];

           TPeroxide=zeros(1,5);

           M0_Peroxide = zeros(1, 8);

           M0_Peroxide(1,1)=1;

           M0_Peroxide(1,2)=1;

           M0_Peroxide(1,3)=M0_LowGCO;

           M0_Peroxide(1,4)=M0_BIP(1,2);

           M0_Peroxide(1,5)=M0_HighGCO;%(1,4);

if V_op<=0.695
```

```
    M0_Peroxide(1,6)=1;

end

if M0_Peroxide(1,1)==1 && M0_Peroxide(1,2)==1 && M0_Peroxide(1,3)==1
&& M0_Peroxide(1,6)==1

    TPeroxide(1,1)=1;

    TPeroxide(1,2)=1;

    TPeroxide(1,3)=1;

    Mn =TPeroxide*D_Peroxide+M0_Peroxide;

    M0_Peroxide = Mn;

    Perout1=1;

end

TPeroxide=zeros(1,5);

M0_Peroxide = zeros(1, 8);

           M0_Peroxide(1,1)=1;

           M0_Peroxide(1,2)=1;

           M0_Peroxide(1,3)=M0_LowGCO;

           M0_Peroxide(1,4)=M0_BIP(1,2);

           M0_Peroxide(1,5)=M0_HighGCO;

if M0_Peroxide(1,1)==1 && M0_Peroxide(1,4)==1 && M0_Peroxide(1,6)==1
&& M0_Peroxide(1,3)==1

    TPeroxide(1,1)=1;

    TPeroxide(1,4)=1;

    Mn =TPeroxide*D_Peroxide+M0_Peroxide;

    M0_Peroxide = Mn;

    Perout2=1;

end

TPeroxide=zeros(1,5);

M0_Peroxide = zeros(1, 8);

           M0_Peroxide(1,1)=1;

           M0_Peroxide(1,2)=1;

           M0_Peroxide(1,3)=M0_LowGCO;
```

```
            M0_Peroxide(1,4)=M0_BIP(1,2);

            M0_Peroxide(1,5)=M0_HighGCO;

if M0_Peroxide(1,5)==1 && M0_Peroxide(1,6)==1

    TPeroxide(1,1)=1;

    TPeroxide(1,5)=1;

     Mn =TPeroxide*D_Peroxide+M0_Peroxide;

    M0_Peroxide = Mn;

    Perout3=1;

end

end
```

Radical Attack

```
function [ Radout, M0_Radical ] = Untitled3( M0_Peroxide, V_op,
M0_BIP )

Radout=0;

D_Radical = [ -1 -1 0 -1 1

               0 -1 -1 -1 1];

           TRadical=zeros(1,2);

           M0_Radical=zeros(1,5);

           M0_Radical(1,1)=1;

           M0_Radical(1,2)=M0_Peroxide(1,8);

           M0_Radical(1,3)=M0_BIP(1,2);

if V_op<=0.695;

    M0_Radical(1,4)=1;

end

if M0_Radical(1,1)==1 && M0_Radical(1,2)==1 && M0_Radical(1,4)==1;

    TRadical(1,1)=1;

    Mn=TRadical*D_Radical+M0_Radical;

    M0_Radical=Mn;

end

if M0_Radical(1,2)==1 && M0_Radical(1,3)==1 && M0_Radical(1,4)==1;

    TRadical(1,2)=1;
```

```
    Mn=TRadical*D_Radical+M0_Radical;
    M0_Radical=Mn;
end
if M0_Radical(1,5)==1;
    Radout=1;
end
end
```

Catalyst Degradation

Carbon Catalyst Degradation

```
function CCout   = func( V_op )
CCout=0;
D_Carbon = [ -1 0 0 -1 -1 1
             0 -1 -1 1 0 0 ];
         M0_Carbon = zeros (1,6);
         M0_Carbon(1,1)=1;
         M0_Carbon(1,2)=1;
         TCarbon = zeros(1,2);
if V_op>=0.55;
    M0_Carbon(1,3)=1;
end
if V_op>=1.1;
    M0_Carbon(1,5)=1;
end
if M0_Carbon(1,1)==1 && M0_Carbon(1,2)==1 && M0_Carbon(1,3)==1 &&
M0_Carbon(1,5)==1;
    TCarbon(1,1)=1;
    TCarbon(1,2)=1;
    Mn=TCarbon*D_Carbon+M0_Carbon;
    M0_Carbon=Mn;
end
```

```
if M0_Carbon(1,6)==1;

    CCout=1;

end

end
```

Immature Pt Agglomeration

```
function [ ImPtAg1, ImPtAg2, ImPtAg3, ImPtAg4] = func( t, V_op,
R_humidity_a, R_humidity_c )

RH_tot = (R_humidity_a + R_humidity_c)/2;

ImPtAg1 = 0;

ImPtAg2 = 0;

ImPtAg3 = 0;

ImPtAg4 = 0;

D_ImPtAg = [ -1 -1 -1 -1 1];

M0_ImPtAg = zeros(1,5);

M0_ImPtAg(1,1)=1;

TImPtAg = zeros(1,1);

if t<144000;

    M0_ImPtAg(1,2)=1;

end

if  V_op >= 0.9;

     M0_ImPtAg(1,4) = 0;

end

if V_op < 0.9;

     M0_ImPtAg(1,4) = 1;

end

if RH_tot >= 0.25;

     M0_ImPtAg(1,3) = 1;

end

if RH_tot < 0.25;

     M0_ImPtAg(1,3) = 0;

end
```

```
if V_op <= 1.0 && V_op > 0.8 && M0_ImPtAg(1,1) == 1 &&
M0_ImPtAg(1,2) == 1 && M0_ImPtAg(1,4) == 1 && M0_ImPtAg(1,3) == 1;

    TImPtAg(1,1) = 1;

    Mn = TImPtAg*D_ImPtAg+M0_ImPtAg;

    M0_ImPtAg = Mn;

   if M0_ImPtAg(1,5) == 1;

        ImPtAg1 = 1;

   end

end

if V_op <= 0.8 && V_op > 0.65 && M0_ImPtAg(1,1) == 1 &&
M0_ImPtAg(1,2) == 1 && M0_ImPtAg(1,4) == 1 && M0_ImPtAg(1,3) == 1;

    TImPtAg(1,1) = 1;

    Mn = TImPtAg*D_ImPtAg+M0_ImPtAg;

    M0_ImPtAg = Mn;

   if M0_ImPtAg(1,5) == 1;

        ImPtAg2 = 1;

    end

end

if V_op <= 0.65 && V_op > 0.41  && M0_ImPtAg(1,1) == 1 &&
M0_ImPtAg(1,2) == 1 && M0_ImPtAg(1,4) == 1 && M0_ImPtAg(1,3) == 1;

    TImPtAg(1,1) = 1;

    Mn = TImPtAg*D_ImPtAg+M0_ImPtAg;

    M0_ImPtAg = Mn;

   if M0_ImPtAg(1,5) == 1;

        ImPtAg3 = 1;

    end

end

if V_op <0.41  && M0_ImPtAg(1,1) == 1 && M0_ImPtAg(1,2) == 1 &&
M0_ImPtAg(1,4) == 1 && M0_ImPtAg(1,3) == 1;

    TImPtAg(1,1) = 1;

    Mn = TImPtAg*D_ImPtAg+M0_ImPtAg;

    M0_ImPtAg = Mn;
```

```
   if M0_ImPtAg(1,5) == 1;
        ImPtAg4 = 1;
    end
end
end
```

Mature Pt Agglomeration

```
function [ MaPtAg1, MaPtAg2, MaPtAg3, MaPtAg4] = func( t, V_op,
R_humidity_a, R_humidity_c )
RH_tot = (R_humidity_a + R_humidity_c)/2;
MaPtAg1 = 0;
MaPtAg2 = 0;
MaPtAg3 = 0;
MaPtAg4 = 0;
D_MaPtAg = [ -1 -1 -1 -1 1];
M0_MaPtAg = zeros(1,5);
M0_MaPtAg(1,1)=1;
TMaPtAg = zeros(1,1);
if t>144000;
    M0_MaPtAg(1,2)=1;
end
if  V_op >= 1;
     M0_MaPtAg(1,4) = 0;
end
if V_op < 1;
     M0_MaPtAg(1,4) = 1;
end
if RH_tot >= 0.25;
     M0_MaPtAg(1,3) = 1;
end
if RH_tot < 0.25;
     M0_MaPtAg(1,3) = 0;
```

```
end

if V_op <= 1.0 && V_op > 0.9 && M0_MaPtAg(1,1) == 1 &&
M0_MaPtAg(1,2) == 1 && M0_MaPtAg(1,4) == 1 && M0_MaPtAg(1,3) == 1;

    TMaPtAg(1,1) = 1;

    Mn = TMaPtAg*D_MaPtAg+M0_MaPtAg;

    M0_MaPtAg = Mn;

   if M0_MaPtAg(1,5) == 1;

        MaPtAg1 = 1;

   end

end

if V_op <= 0.9 && V_op > 0.8 && M0_MaPtAg(1,1) == 1 &&
M0_MaPtAg(1,2) == 1 && M0_MaPtAg(1,4) == 1 && M0_MaPtAg(1,3) == 1;

    TMaPtAg(1,1) = 1;

    Mn = TMaPtAg*D_MaPtAg+M0_MaPtAg;

    M0_MaPtAg = Mn;

   if M0_MaPtAg(1,5) == 1;

        MaPtAg2 = 1;

    end

end

if V_op <= 0.8 && V_op > 0.65  && M0_MaPtAg(1,1) == 1 &&
M0_MaPtAg(1,2) == 1 && M0_MaPtAg(1,4) == 1 && M0_MaPtAg(1,3) == 1;

    TMaPtAg(1,1) = 1;

    Mn = TMaPtAg*D_MaPtAg+M0_MaPtAg;

    M0_MaPtAg = Mn;

   if M0_MaPtAg(1,5) == 1;

        MaPtAg3 = 1;

    end

end

if V_op <0.65  && M0_MaPtAg(1,1) == 1 && M0_MaPtAg(1,2) == 1 &&
M0_MaPtAg(1,4) == 1 && M0_MaPtAg(1,3) == 1;

    TMaPtAg(1,1) = 1;

    Mn = TMaPtAg*D_MaPtAg+M0_MaPtAg;
```

```
    M0_MaPtAg = Mn;
   if M0_MaPtAg(1,5) == 1;
        MaPtAg4 = 1;
    end
end
end
```

BIP Corrosion

```
function [BIPout, M0_BIP]   = fcn(t)
BIPout = 0;
D_BIP = [-1 1];
        M0_BIP = zeros(1,2);
        M0_BIP(1,1) = 1;
if t >= 2880000 && M0_BIP(1,1) == 1;
    TBIP = zeros(1,1);
    TBIP(1,1) = 1;
    Mn = TBIP*D_BIP+M0_BIP;
    M0_BIP = Mn;
end
if M0_BIP(1,2) == 1;
   BIPout = 1;
end
end
```

GDL Degradation

```
function GDLout   = func( M0_Swelling, M0_Flood, M0_Radical)
GDLout=0;
D_GDL= [-1 0 0 0 0 -1 1
        0 -1 0 0 0 1 0
        0 0 -1 0 0 1 0
        0 0 0 -1 0 1 0
        0 0 0 0 -1 1 0 ];
```

```
    M0_GDL=zeros(1,7);

    M0_GDL(1,1)=1;

    M0_GDL(1,2)=M0_Swelling(1,4);

    M0_GDL(1,3)=M0_Flood(2,1);

    M0_GDL(1,4)=M0_Radical(1,5);

if M0_GDL(1,1)==1 &&
M0_GDL(1,2)>0&&M0_GDL(1,3)>0&&M0_GDL(1,4)>0&&M0_GDL(1,5)>0;

    TGDL=zeros(1,5);

    TGDL(1,1)=1;

    Mn=TGDL*D_GDL+M0_GDL;

    M0_GDL=Mn;

end

if M0_GDL(1,7)==1;

    GDLout=1;

end

end
```